Step IV of the Muon Ionization Cooling Experiment (MICE) and the multiple scattering of muons

Timothy Carlisle
Christ Church, Oxford

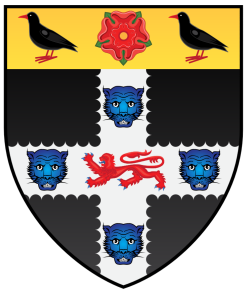

Thesis submitted in fulfilment of the requirements for the degree of Doctor of Philosophy at the University of Oxford

Michaelmas Term, 2013

Acknowledgements

I wish to thank my supervisor, John Cobb, for his hard work, patience and guidance throughout the course of my degree. I am very grateful to Victoria Blackmore for taking the time to read my drafts and for her encouragement. Thanks also to Chris Rogers, and my colleagues Mark Rayner and Chris Tunnell, for their help over the years. Last but not least, I'd like to thank my family and friends for their support.

Contents

List of Figures

List of Tables

Abstract

The Muon Ionization Cooling Experiment (MICE) is the first technical demonstration of muon ionization cooling, using a prototype section of a Neutrino Factory cooling channel. MICE is currently under construction at the Rutherford-Appleton Laboratory in the UK and will make the first cooling measurements in 2015, in Step IV of the experimental programme.

Cooling predictions in Monte Carlo simulations of Step IV were found to disagree with the predictions of the "cooling formula", a widely-used approximation, by up to 30% in liquid hydrogen (LH_2). This disagreement was shown to originate, largely, from the multiple scattering expression used in the cooling formula. It was necessary to go back to the fundamental physics of scattering to derive a more accurate expression that includes scattering from atomic electrons. A modified form of the cooling formula was derived using this expression and gave better agreement with the Monte Carlo in LH_2. Predictions are given for the equilibrium emittance, using the new expression, for seven low Z materials at muon momenta of $140, 200$ and $240\,\mathrm{MeV}/c$.

Theories which predict the distribution of multiple scattering angles are briefly reviewed, focusing on Molière theory and its variants, which are the most widely-used theories. The distributions predicted by these theories are used in most Monte Carlo codes but their implementation is not transparent, especially regarding the treatment of scatters with atomic electrons, which are important in low Z materials. A simple Monte Carlo model to predict multiple scattering distributions was developed that correctly treats scatters off electrons. The model gives very good agreement with measurements by the MuScat Experiment.

Investigations were made into the possibility of measuring multiple scattering in MICE Step IV, both with and without the magnetic field. Preliminary results suggest that measurements are easier with no magnetic field, where tracks are straight. Corrections to account for the resolution of the scintillating-fibre trackers are required in both cases, but these are substantially smaller when straight tracks are used.

Chapter 1

Introduction

Neutrinos are one of the most abundant types of particle in the Universe yet they violate one of the most successful theories in science, the Standard Model, through flavour oscillation. The Neutrino Factory is widely considered the ideal facility with which to study neutrino oscillations but requires very high fluxes of stored muons which must be cooled before acceleration. Ionization cooling is the only technique fast enough, using sequential absorbers and RF cavities, but is untested and involves significant engineering challenges.

The Standard Model (SM) of particle physics describes the Universe as being populated by two types of elementary particle known as fermions (quarks and leptons) and bosons. There are six types (flavours) of quarks in the SM: up, down, strange, charm, bottom and top. The electron (e^-), muon (μ^-) and tau (τ^-) leptons each have a neutrino partner (ν_e, ν_μ, ν_τ) to give a total of six leptons. Bosons act as force-carriers for the weak (via the $W^\pm$ & Z bosons), strong (gluon) and electromagnetic (photon) forces. The existence of the Higgs Boson* has been confirmed by recent results at the Large Hadron Collider (LHC) [1] [2].

Neutrinos provide an exciting glimpse of "new physics" beyond the Standard Model and also offer a unique window into the central engines of stars and galaxies through neutrino telescopes such as IceCube [4]. The Neutrino Factory is an accelerator facility designed to answer the remaining fundamental questions in our understanding of neutrino physics. Its design demands new technology for the production, collimation and transport of intense beams of muons, including the untested technique known as muon ionization cooling.

The Muon Ionization Cooling Experiment (MICE) [5] will be the first demonstration of the technique, and is currently under construction at the Rutherford Appleton Laboratory in Oxfordshire,

*An introduction to the Higgs mechanism is given in [3].

England. It is described in Chapter 2. An overview of the field of Neutrino Physics is now presented, and the concept of muon ionization cooling introduced.

1.1 Neutrino Oscillations

Since its development in the 1970s the Standard Model has been verified by experiment for two decades, successfully predicting the existence of the W and Z bosons, the τ^- lepton and the top quark, identifying their masses with remarkable precision. It was not until the confirmation of neutrino oscillations in 1998 by the Super Kamiokande Experiment [6] that any physics beyond the SM was found.

The Super Kamiokande Experiment detected atmospheric (produced by cosmic rays) and solar neutrinos using an underground tank holding $50,000$ tons of ultra-pure water, surrounded by over $11,000$ photomultiplier tubes (PMTs). Neutrino interactions with the nuclei and electrons in the water produce high energy leptons ($e^{\pm}, \mu^{\pm}$), which in turn emit Cherenkov light that can be detected using PMTs. The timing and charge information recorded by the PMTs is then used indirectly to measure the neutrino's properties. Super Kamiokande measured a zenith angle and energy dependent deficit in the ratio of the muon to electron atmospheric neutrino fluxes, implying that neutrinos change flavour. This process requires neutrinos to have mass, forbidden in the (classic) SM.

In 2001, further evidence for neutrino flavour change was found by the Sudbury Neutrino Observatory (SNO) [7], which was the first experiment able to measure the total neutrino flux ($\phi_{\nu_e} + \phi_{\nu_{\mu,\tau}}$) using a large tank containing $1,000$ tons of heavy water. SNO identified $\nu_e \longrightarrow \nu_{\mu,\tau}$ flavour oscillation, in solar neutrinos. The SNO results solved the long-standing Solar Neutrino Problem, in which the measured solar neutrino flux (ν_e) on Earth (as measured by the Homestake Experiment [8]) was a third of the rate expected from solar models. SNO measured a total flux which was consistent with solar models, which strongly implied a large fraction of the ν_e flux produced in the Sun changes flavour en route to the Earth. The reactor-based KamLAND Experiment [9] confirmed the oscillation hypothesis in 2003, measuring a large deficit in the $\bar{\nu}_e$ flux produced in nuclear fission.

The theoretical framework for neutrino oscillations pre-dated experimental verification by several decades (Ray Davis's Homestake Experiment aside), starting with the work of Pontecorvo in 1957 [10], followed by Maki, Nakagawa and Sakata [11]. The standard theory of neutrino oscillation states that the neutrino flavour eigenstates ν_e, ν_μ, ν_τ propagate through space as coherent superpositions of mass eigenstates, expressed as ν_1, ν_2 and ν_3. The superposition of neutrino mass states is described using the Pontecorvo-Maki-Nakagawa-Sakata (PMNS) mixing matrix:

$$U = \begin{bmatrix} c_{12}c_{13} & s_{12}c_{13} & s_{12}e^{-i\delta} \\ -s_{12}c_{23} - c_{12}s_{23}s_{13}e^{i\delta} & c_{12}c_{23} - s_{12}s_{23}s_{13}e^{i\delta} & s_{23}c_{13} \\ s_{12}c_{23} - c_{12}s_{23}s_{13}e^{i\delta} & -c_{12}c_{23} - s_{12}s_{23}s_{13}e^{i\delta} & s_{23}c_{13} \end{bmatrix} K' \tag{1.1}$$

where $c_{ij} \equiv \cos\theta_{ij}$, $s_{ij} \equiv \sin\theta_{ij}$ and $K' = \text{diag}(e^{i\alpha_1/2}, e^{i\alpha_2/2}, 1)$. It is parametrized in terms of three mixing angles $\theta_{12}, \theta_{23}, \theta_{31}$ and three CP violating phases δ, α_1 and α_2. The Majorana phases, $\alpha_{1,2}$, are only significant if neutrinos are identical to their anti-particle partner ($\nu_e \equiv \bar{\nu}_e$), but this issue does not affect neutrino oscillations. Experiments measure the squared differences of the neutrino masses: $\Delta m^2_{ij} = \Delta m^2_i - \Delta m^2_j$. Apart from the Majorana phases, neutrino flavour mixing is a direct analogue of mixing in the quark sector, as described using the Cabibbo-Kobayashi-Maskawa (CKM) matrix.

Recent results by the Planck Collaboration have largely ruled out the existence of sterile neutrinos [12], thereby supporting the three flavour framework. The two mass differences, Δm^2_{ij}, and mixing angles θ_{12}, θ_{23} have been measured by past experiments and are well constrained, as explained in the comprehensive review of the field by Gonzalez-Garcia and Malton [13]. θ_{13} is known to be large after confirmation by several experiments including Daya Bay [14], RENO [15] and T2K [16]. The most important questions remaining in our understanding of neutrino oscillations are the sign of Δm^2_{13} and the phase δ, for which a new generation of experiments is required [17], such as the Neutrino Factory.

1.2 The Neutrino Factory

The high-energy Neutrino Factory (NF) is widely considered the "ultimate precision" instrument with which to study the neutrino sector and the only facility capable of achieving sensitivity comparable to the quark sector [17]. Figure 1.1 shows the baseline design for the Neutrino Factory as outlined in the International Design Study (IDS-NF) [18]. The facility is designed to generate intense, high-energy neutrino beams for study in large magnetized iron neutrino detectors (MIND). A high power (2–5 MW) proton driver and target generate charged pions, which are captured in a 20 T superconducting solenoidal field. The pions quickly decay ($\tau \sim 26$ ns) into muons, which must then be conditioned in the NF front-end (buncher, phase rotation and cooling) prior to acceleration. A combination of linacs, recirculating linacs (RLAs) and fixed field alternating gradient accelerators (FFAGs) accelerate the muons to energies of order of ≈ 20 GeV for input into the decay rings. The stored muon beams decay by $\mu^+ \longrightarrow e^+ + \nu_e + \bar{\nu_\mu}$ and $\mu^- \longrightarrow e^- + \bar{\nu_e} + \nu_\mu$, to produce intense beams of neutrinos directed towards MIND detectors in which their properties can be observed and studied. The most sensitive method to study CP violation is by measuring the transition probabilities of $\nu_e(\bar{\nu_e}) \longrightarrow \nu_\mu(\bar{\nu_\mu})$, which is known as the "golden" channel. These processes can be measured by detecting muons with the opposite charge to that of the parent beam in the storage rings. Magnetized detectors allow differentiation of the $\mu^\pm$ flux. Observation of $P(\nu_e \longleftrightarrow \nu_\mu) \neq P(\bar{\nu_e} \longleftrightarrow \bar{\nu_\mu})$ would confirm CP violation in the lepton sector.

As the first major muon-beam facility, the NF design contains significant technical challenges, including the operation of a high power target in strong magnetic fields (20 T) and in the front end of the facility (the buncher, phase rotation and cooling stages), as discussed in Feasibility Study II (FS2) and II-b (FS2b) [19, 20]. A key challenge in achieving the $\sim 10^{21}$ muons per year production benchmark lies in maximizing the muon transmission to the decay rings. As tertiary decay products, muons beams are large and divergent, whilst the downstream accelerating structures (linac/RLA/FFAG) have only a limited acceptance[†]. The Neutrino Factory design uses a ≈ 150 m cooling channel to reduce the size and divergence of the beam prior to acceleration, thereby increasing the flux accelerated through to the storage rings. Whilst the NF design is technically very demanding, it greatly compliments designs for the Muon Collider (MC) [21] as they can share

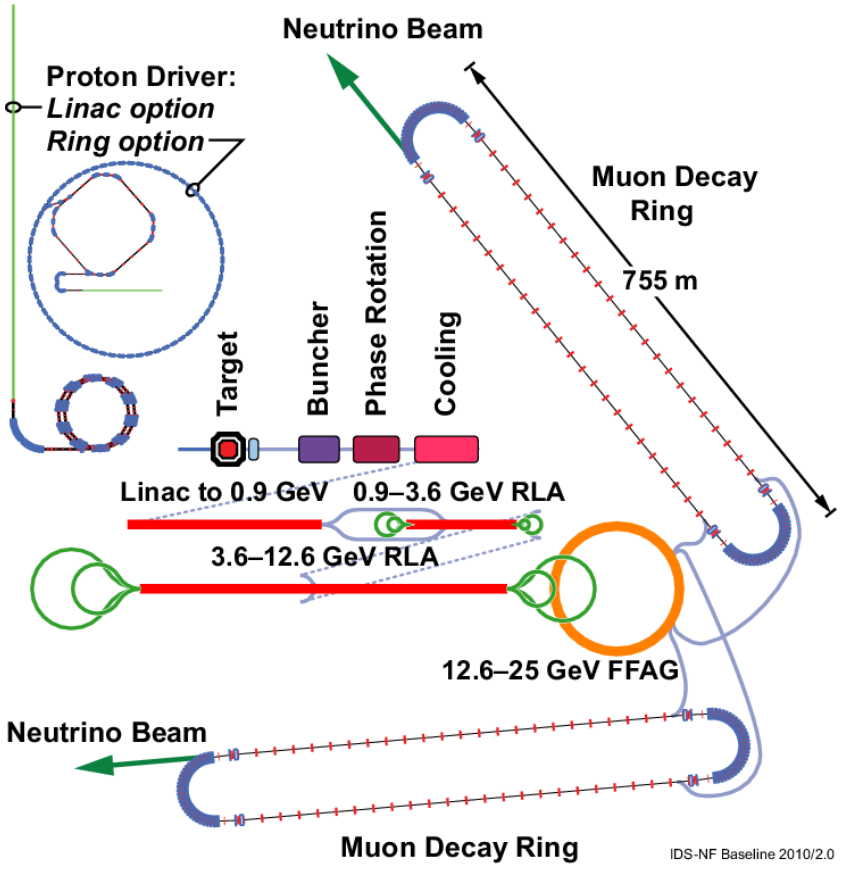

Figure 1.1: Schematic of the Neutrino Factory according to the International Design Study baseline [18].

the same target and front-end. As a result it is likely a NF can be upgraded to a MC at a vastly lower cost than building a new facility from scratch. The MC design poses considerable technical challenges in its own right, however.

The physics case for a Muon Collider depends, largely, on whether the LHC discovers new physics above 1 TeV. If so, there is a definite case for a TeV-scale collider, candidates for which include the Compact Linear Collider (CLIC) [23] and Muon Collider. If not, it is likely that the International Linear Collider (ILC) [24] will be prioritized, which has a centre of mass (CM) energy of 500 GeV but is upgradeable to 1 TeV. As a synchrotron machine, a muon collider will require only a very modest land footprint relative to the ILC and CLIC, which are linear, electron machines. Synchrotron acceleration of electrons above $O(100\,\text{GeV})$ is impractical due to the very high energy losses (synchrotron radiation). Linear acceleration to TeV energies requires very long accelerating

[†] Acceptance describes the largest transmissible beam in a channel or accelerating structure, typically defined transversely, using beam emittance or particle amplitude [22].

Figure 1.2: The technique of ionization cooling whereby a beam of muons is directed through an absorber followed immediately by a radio-frequency (RF) accelerating cavity.

structure ($\sim$ 50 km in CLIC) which are very expensive to build and operate. Muons, by virtue of their larger mass, lose $\sim 10^9$ times less energy to synchrotron radiation then electrons, and are therefore very well suited to TeV, circular acceleration. The Project X high-intensity proton source [25] at Fermilab is anticipated to be a first step towards a muon accelerator facility. Whilst a Muon Collider is potentially less expensive and much smaller than the ILC and CLIC schemes, it demands ionization cooling many orders of magnitude greater (a factor of 10^6 in 6D) than required in a Neutrino Factory.

1.3 Ionization Cooling

Designs for both the Neutrino Factory and Muon Collider require very high fluxes of muons for acceleration to GeV/TeV energies. Beam cooling is essential to maximize the flux of muons through the limited acceptance of accelerating structures. Existing techniques such as stochastic (with protons) and synchrotron (electrons) cooling are too slow for use with muons due to their $\tau \sim 2\,\mu$s lifetime. The only technique fast enough is ionization cooling, which has never been demonstrated experimentally despite being first proposed in 1981 [26]. It involves the systematic reduction in emittance through energy loss in absorbers followed by longitudinal re-acceleration in radio frequency (RF) cavities, as illustrated in Figure 1.2. Energy loss in the material reduces the momenta of the muons thereby compressing (cooling) the phase space of the beam. The lost longitudinal muon momentum is then restored using high gradient RF acceleration. The cooling is counteracted, however, by multiple Coulomb scattering (MCS) in the absorber which inflates the transverse phase space (heating). Cooling is commonly predicted using the cooling formula (Equation 2.9), which

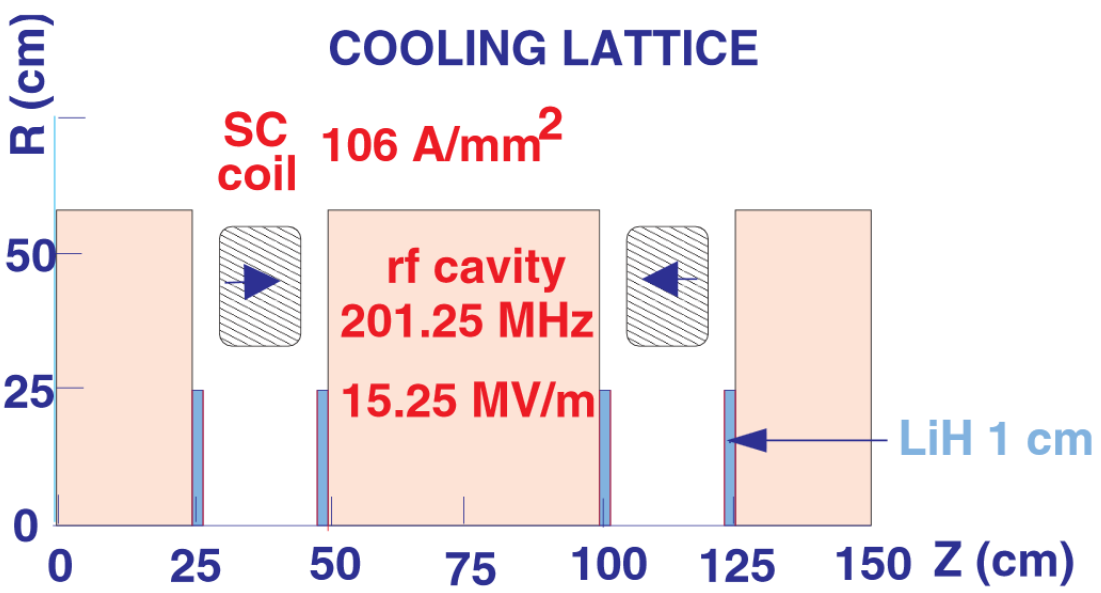

Figure 1.3: Schematic of a single cell in an ionization cooling lattice [20].

uses approximations for energy loss and the rms angle of scattering. A derivation of the cooling formula is presented in Chapter 2.

Whilst the actual physics of ionization cooling are well-understood, muon cooling presents many significant engineering and operational challenges. The FS2 cooling scheme (2001) [19] uses a 100 m cooling channel, which accepts a large transverse emittance beam of $\sim$ 12 mm at input, and cools it to $\approx$ 2 mm using absorbers such as liquid hydrogen (LH_2) or lithium hydride (LiH), increasing the flux into the downstream accelerators by a factor of 1.7. A shorter, 80 m channel, using FFAGs with a larger acceptance, was proposed in FS2b (2006) [20], and matched the performance of the FS2 design. Figure 1.3 shows the baseline design for a single cell of the FS2b cooling channel, which contains two 50 cm long, 201.25 MHz RF cavities. High gradient RF (15.25 MeV/m) is necessary to rapidly replace the energy lost by muons in the absorbers ($dE/dX \sim 30$ MeV/m in LH_2), which is very challenging to achieve. The RF cavities are sealed with 1 cm LiH windows, which also act as the cooling absorbers. An alternating 2.8 T solenoidal field is produced by one solenoid per half cell, located between the cavities, to transport the beam.

A Muon Collider cooling channel will demand cooling many orders of magnitude greater than required by a NF, however, and require phase space reduction in six dimensions. Current 6D cooling schemes [27] involve a helical cooling channel (HCC) which use hydrogen-pressured RF

cavities within a magnetic field with solenoidal, helical dipole and helical quadrupole components. The Muon Ionization Cooling Experiment (MICE) [5] will be the first technical demonstration of ionization cooling, using a single, repeatable, module of a prototype cooling channel for a Neutrino Factory. The MICE cooling lattice is based upon the design given in FS2 [19] but will also run with LiH absorbers, as used in the IDS-NF design [18].

1.4 Focus of this thesis

The first demonstration of muon ionization cooling will be made in Step IV of MICE in 2015, a description of which is given in Chapter 3. This thesis presents a detailed Monte Carlo study of the anticipated performance of Step IV, as a cooling channel and as a platform to measure muon multiple Coulomb scattering (MCS). The cooling estimates, however, were found to disagree with the cooling formula, which is a widely-used approximation to make cooling predictions. This disagreement was as large as 30% in low Z materials, and originates, largely, from the approximations used to treat MCS, as will be shown in Chapter 4. This discrepancy raised important questions as to the actual physics contained within these approximations, and in Monte Carlo scattering models. It was necessary, therefore, to go right back to the fundamental physics of scattering to understand these issues. In Chapter 5 more accurate scattering approximations are developed which improve the agreement between the cooling formula and simulation.

Chapter 6 describes how the distribution of scattering angles can be obtained using a theory of multiple scattering, and discusses experimental measurements. A new Monte Carlo model, based on only simple, fundamental physics is described in Chapter 7 and is shown to give very good agreement with the measurements of the MuScat Experiment [28]. Chapter 8 presents the case for MICE to make its own scattering measurements in Step IV. To begin, some essential beam physics will now be introduced, followed by a description of MICE.

Chapter 2

Muon Ionization Cooling

> Ionization cooling involves the extraction of transverse momenta from a beam of particles via the sequential removal of energy in material, followed by RF cavity acceleration. The Muon Ionization Cooling Experiment (MICE) is a prototype section of a cooling channel for a Neutrino Factory, and will make the first ionization cooling measurements from 2015 onwards.

The development of muon ionization cooling is critical to the design of both the Neutrino Factory and Muon Collider facilities. Ionization cooling involves passing muon beams through absorber materials to reduce their longitudinal and transverse momentum through energy loss. The lost longitudinal momentum is then restored immediately using high gradient RF cavities. Despite the physics of ionization cooling being well understood it has never been demonstrated using muons, and the construction and operation of a cooling channel involves many significant engineering and technical challenges.

The Muon Ionization Cooling Experiment (MICE) is the first demonstration of muon cooling, using a section of a prototype cooling channel based on the Feasibility Study II [19] design. MICE and the technique of ionization cooling are described in this chapter. First of all, it is necessary to introduce some standard beam physics.

2.1 Collective description of a beam of particles

The collective motion of a beam of particles, that is, its transverse distribution in trace space, can be described in its most basic form by the first and second order moments of the distribution function. For a symmetric beam about the design axis the first order moments are zero, whilst the second order moments are the variances of the distribution, given in 2D by the covariance matrix [29]:

$$M = \begin{bmatrix} \sigma_{xx} & \sigma_{xx'} \\ \sigma_{x'x} & \sigma_{x'x'} \end{bmatrix} = \varepsilon \begin{bmatrix} \beta_\perp & -\alpha_\perp \\ -\alpha_\perp & \gamma_\perp \end{bmatrix} \tag{2.1}$$

where (x, x') are the coordinates of the beam in trace space, where x is the horizontal (transverse) position and $x' = p_x/p_z$. $\alpha_\perp$, $\beta_\perp$ and $\gamma_\perp$ are known as the Twiss Parameters. One can visualize the trace space as an rms ellipse, as shown in Figure 2.1, which has a general equation: $\gamma_\perp x^2 + 2\alpha_\perp xx' + \beta_\perp x'^2 = \varepsilon$. The area of the beam in trace space is the known as the (geometric) emittance, ε, where:

$$\det M = \sigma_{xx}\sigma_{x'x'} - \sigma_{xx'}^2 = \varepsilon^2. \tag{2.2}$$

The rms beam size, σ_x, and divergence, $\sigma_{x'}$, are given by:

$$\begin{aligned} \sigma_x &= \sqrt{\beta_\perp \varepsilon} \\ \sigma_{x'} &= \sqrt{\varepsilon/\beta_\perp}\,. \end{aligned} \tag{2.3}$$

Whilst the orientation and eccentricity of the ellipse will change along a beam transport line, for example because of magnetic fields, the area of the ellipse, $\varepsilon\pi$, remains constant under a conservative force. This is known as Liouville's Theorem in which the emittance of a beam is conserved. Ionization cooling violates this theorem, however, through energy loss in material which allows the phase space area, i.e. the emittance, of a beam to be reduced. This has the effect of reducing the size and divergence of a beam for input into accelerating structures such as linacs, which have only a limited acceptance.

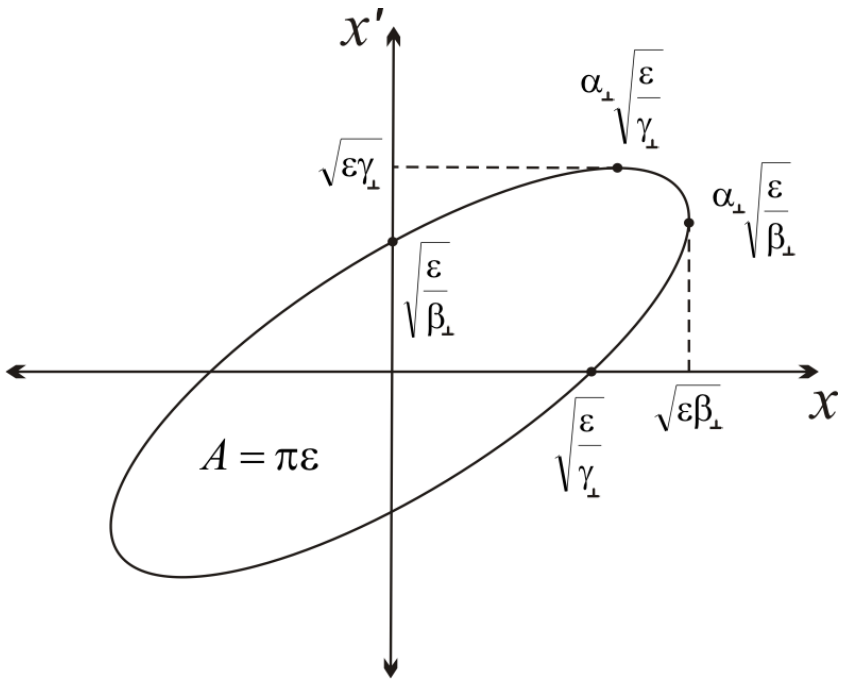

Figure 2.1: Trace space of a beam in the $x - x'$ plane.

Emittance is often expressed as a normalized value, which is constant under acceleration. The normalized transverse (4D) emittance is defined as:

$$\varepsilon_n = \beta\gamma\varepsilon = \frac{p}{m}\varepsilon \tag{2.4}$$

where β is the particle velocity and γ the Lorentz factor [22]. Cooling is described in terms of a reduction in emittance, most commonly in the four transverse, phase space dimensions (x, p_x, y, p_y).

In solenoidal optics the horizontal (x, p_x) and vertical (y, p_y) components are coupled, and the beam covariance matrix (Equation 2.1) can be written in 4D, in phase space, as:

$$M = \begin{bmatrix} \sigma_{xx} & & & \\ \sigma_{xp_x} & \sigma_{p_xp_x} & & \\ \sigma_{xy} & \sigma_{p_xy} & \sigma_{yy} & \\ \sigma_{xp_y} & \sigma_{p_xp_y} & \sigma_{yp_y} & \sigma_{p_yp_y} \end{bmatrix},$$

and can be defined in terms of the Twiss Parameters:

$$M = \begin{bmatrix} \varepsilon_n \beta_\perp mc/p_z & & & \\ -mc\varepsilon_n \alpha_\perp & mcp_z\varepsilon_n\gamma_\perp & & \\ 0 & mc\varepsilon_n(\beta_\perp\kappa - \mathcal{L}) & \varepsilon_n\beta_\perp mc/p_z & \\ -mc\varepsilon_n(\beta_\perp\kappa - \mathcal{L}) & 0 & -mc\varepsilon_n\alpha_\perp & mcp_z\varepsilon_n\gamma_\perp \end{bmatrix}, \tag{2.5}$$

as discussed in Penn and Wurtele's paper [30]. The Twiss parameter $\gamma_\perp \equiv 1/\beta_\perp[1+\alpha_\perp^2+(\beta_\perp\kappa-\mathcal{L})]$, κ is the focusing strength, $\kappa \simeq 0.15B_z/p_z$ m^{-1}, and $\mathcal{L}$ the mean canonical angular momentum.

2.2 The cooling formula

When making cooling predictions it is common to use an approximation known as the "cooling formula" (CF) [31], which is given as Equation 2.9. The formula predicts the fractional change in emittance per unit length of absorber material, for a given beam momentum and magnetic focusing ($\beta_\perp$). This formula will be compared with Monte Carlo predictions in Chapter 3 for Step IV of MICE, which is described later on in this chapter.

As described in Chapter 1, cooling involves two fundamental physics processes: energy loss, which reduces the emittance, and multiple Coulomb scattering (MCS), which inflates it. The effects of both these processes are described in the CF using approximations. The multiple scattering approximation will be discussed in depth in Chapters 5, and alternative expressions developed. It is necessary, therefore, to introduce these approximations by deriving the cooling formula, starting from Equation 2.4:

$$\varepsilon_n = \frac{p}{m}\varepsilon = \frac{p}{m}\sigma_x\sigma_{x'}.$$

The rate of change of (normalized) emittance, for a beam moving through material in the z-direction, is:

$$\frac{d\varepsilon_n}{dz} = \frac{1}{m}\frac{dp}{dz}\sigma_x\sigma_{x'} + \frac{p}{m}\sigma_x\frac{d\sigma_{x'}}{dz}, \tag{2.6}$$

which contains a cooling (energy loss) term and a heating (MCS) term, the 1st and 2nd terms on the right-hand side respectively. The dp/dz term can be expressed in terms of the mean energy loss per unit length, $\langle dE/dX \rangle$, since,

$$E^2 = p^2 + m^2$$
$$dp = \frac{E}{p}dE,$$

which gives:

$$\frac{dp}{dz} = \frac{E}{p}\frac{dE}{dz} = \frac{1}{\beta}\left\langle\frac{dE}{dz}\right\rangle.$$

Substitution back into Equation 2.6 gives,

$$\frac{d\varepsilon_n}{dz} = -\frac{\varepsilon_n}{p\beta}\left\langle\frac{dE}{dz}\right\rangle + \frac{p}{m}\sigma_x\frac{d\sigma_{x'}}{dz},$$

where a minus sign is introduced as $\langle dE/dz \rangle$ is a negative quantity. The final term is redefined using

$$\frac{d\sigma_{x'}^2}{dz} = 2\sigma_{x'}\frac{d\sigma_{x'}}{dz},$$

to give:

$$\frac{d\varepsilon_n}{dz} = -\frac{\varepsilon_n}{p\beta}\left\langle\frac{dE}{dz}\right\rangle + \frac{p}{m}\sigma_x\frac{1}{2\sigma_{x'}}\frac{d\sigma_{x'}^2}{dz}.$$

The definitions for σ_x and $\sigma_{x'}$ in Equation 2.3 are then substituted to give a general formula for cooling:

$$\frac{d\varepsilon_n}{dz} = -\frac{\varepsilon_n}{p\beta}\left\langle\frac{dE}{dz}\right\rangle + \frac{p}{m}\frac{\beta_\perp}{2}\frac{d\sigma_{x'}^2}{dz}. \tag{2.7}$$

The emittance at which the heating and cooling terms are equal, *i.e.* for $d\varepsilon_n/dz = 0$, is defined as the equilibrium emittance:

$$\varepsilon_0 = \frac{p^2\beta\beta_\perp}{2m}\frac{d\sigma_{x'}^2}{dz}\left\langle\frac{dE}{dz}\right\rangle^{-1}. \tag{2.8}$$

Both formulae are usually given in a different form, however, where the heating term is replaced by the following approximation for multiple scattering [31]:

$$\frac{d\langle\theta_0^2\rangle}{dz} = \frac{d\sigma_{x'}^2}{dz} = \left(\frac{13.6\text{ MeV}}{p\beta}\right)^2\frac{1}{X_0}.$$

where $\Delta z/X_0$ is the fraction of a radiation length of the absorber. A similar expression is found in the Particle Data Group (PDG) Review [32], given in Equation 4.2, which has an additional log term. The origins of these MCS approximations are discussed in Chapter 5, and more accurate forms derived.

The general cooling equation can now be rewritten using this expression, along with the relativistic relations $p = \gamma\beta m_\mu c$ and $E = \gamma m_\mu c$ (where $c = 1$), to obtain the standard cooling formula,

$$\frac{d\varepsilon_n}{dz} = \frac{-\varepsilon_n}{\beta^2 E}\left\langle\frac{dE}{dz}\right\rangle + \frac{\beta_\perp(13.6\text{ MeV})^2}{2\beta^3 E m_\mu X_0}. \tag{2.9}$$

The first term represents the cooling due to energy loss and the second the heating due to multiple scattering.

Setting $d\varepsilon_n/dz = 0$ gives the usual expression for equilibrium emittance,

$$\varepsilon_0 = \frac{\beta_\perp (13.6\ \text{MeV})^2}{2\beta m_\mu X_0} \left\langle \frac{dE}{dz} \right\rangle^{-1} . \tag{2.10}$$

The cooling formula, whilst only an approximation, highlights the key elements in designing the most effective ionization cooling channel. A strongly focused beam (small $\beta_\perp$) will have a small size (σ_x) but also a large divergence ($\sigma_{x'}$), so the overall effect of MCS (heating), which increases the divergence of a beam, is reduced. $X_0\langle dE/dz\rangle$ is maximal in low Z materials.

Material	Z	X_0 [g cm^{-2}]	$\langle dE/dz\rangle$ [MeV g^{-1} cm^2]	ρ [g cm^{-3}]	$(X_0 \langle dE/dz\rangle)^2$ (normalized)
Liquid H_2	1	63.04	4.104	0.0708	1.000
Liquid He	2	94.32	1.954	0.125	0.507
LiH		79.62	1.940	0.820	0.356
Li	3	82.78	1.667	0.534	0.284
Be	4	65.19	1.622	1.848	0.167
B	5	52.69	1.651	2.37	0.113
C_2H_4		44.77	2.12	0.94	0.135
C	6	42.70	1.722	2.2	0.081
Al	13	24.01	1.630	2.699	0.023
Ti	22	16.16	1.490	4.54	0.009
Fe	26	13.83	1.463	7.874	0.006
Cu	29	12.86	1.414	8.96	0.005

Table 2.1: Material properties and cooling performance, characterized using the figure of merit $(X_0 \langle dE/dX\rangle)^2$ for muons of kinetic energy 200 MeV ($p = 286.8$ MeV/c).

2.3 Optimal materials for cooling

Cooling channels are required to increase the flux of muons that can be accelerated and then contained in the storage rings of a Neutrino Factory. As shown in Equation 2.9, for cooling to occur the trace space compression due to energy loss must exceed the inflation due to multiple scattering. The cooling formula contains explicit dependencies on the properties of the absorber material (X_0, $\langle dE/dz\rangle$). The greater the energy loss of a beam in an absorber the greater the reduction in phase space. Whilst the rate of energy loss, per g of material, does indeed increase with atomic number Z, so too does the amount of multiple scattering (implicit in X_0) and at a higher rate. This is evident in

Table 2.1 which lists the material properties from $Z = 1$ (LH_2) to 29 (Cu), taken from the PDG Review [32], where X_0 values are calculated using Tsai's expression [33]. The use of radiation length to describe MCS originates from the work of Rossi and Greisen [34] and will be discussed in detail in Chapter 5. The central particle density in a beam is proportional to $\varepsilon_0^{-2} \longrightarrow (X_0 \langle dE/dz \rangle)^2$, and is commonly used as a figure of merit for the cooling performance of a material. Liquid hydrogen is the ideal cooling material, followed by liquid helium.

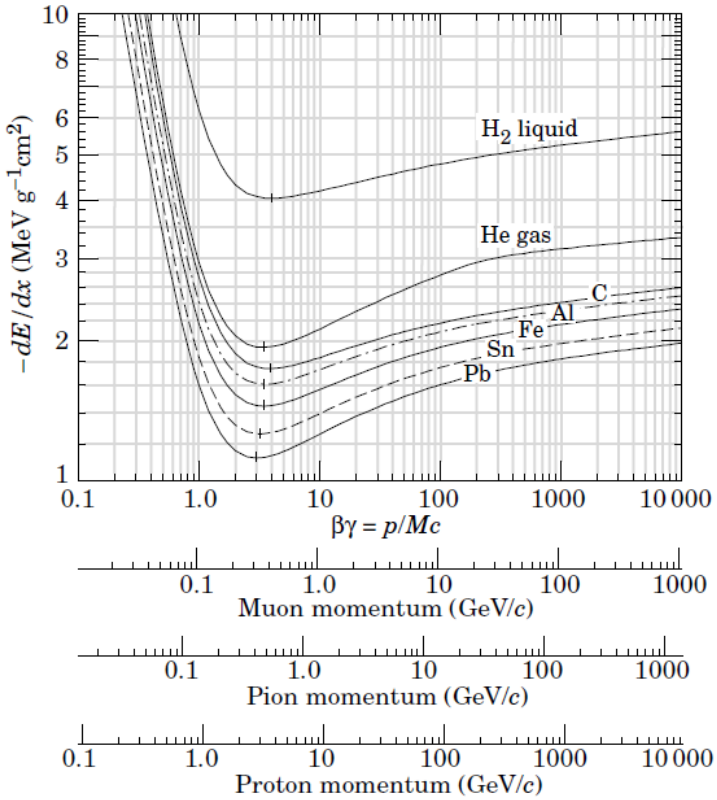

Figure 2.2: Mean energy loss rate in liquid hydrogen, gaseous helium, carbon, aluminium, iron, tin, and lead. Radiative effects, relevant for muons and pions, are not included. These become significant for muons in iron for $\beta\gamma > 1000$, and at lower momenta for muons in higher Z absorbers. Figure and caption reproduced from Figure 30.2 in [32]. Copyright (2012) by The American Physical Society.

The average energy loss of muons and other charged particles through material is calculated using the Bethe* stopping power formula, which is given in Section 30.2.2 of [32] (2012 edition), and is stated to be accurate to around 1% for pions for $40\,\mathrm{MeV}/c < p < 6\,\mathrm{GeV}/c$. Aside from a slight dependence on particle mass, $\langle dE/dz \rangle$ is dependent only on the particle velocity, β. The mean rate of energy loss in different materials, as a function of momentum, is compared in Figure 2.2, for

muons, pions and protons. As the figure shows, $\langle dE/dz \rangle$ scales inversely with momentum, and rapidly so below 100 MeV/c. Muons are unstable particles, however, and decay within a few μs, so cooling must be carried out very quickly to maintain a high muon flux. The slower the muon beam the shorter the distance over which the necessary phase space reduction can be carried out, which places very strong demands on the cooling channel. Consequently, the choice of p is very important to the performance of a Neutrino Factory. Muon cooling channels are designed to cool $\sim 200\,\mathrm{MeV}/c$ ($\beta\gamma \approx 2$) muon beams.

2.4 The Muon Ionization Cooling Experiment

The Muon Ionization Cooling Experiment (MICE) [5, 35], shown in Figure 2.3, is a test of a prototype muon cooling channel. It is an integral part of the worldwide research effort towards a Neutrino Factory, discussed in Chapter 1. MICE is an engineering demonstration to achieve and accurately measure ionization cooling in a single SFOFO ("super focus focus") lattice cell. MICE uses three 35 cm liquid hydrogen (LH_2) absorbers to achieve a 10% reduction in emittance and eight 201 MHz RF cavities to re-accelerate the muon beam. Spectrometer solenoids at each end of the cooling channel contain scintillating-fibre trackers which measure the emittance of the beam at input and output. Currents in the match coils, which are housed inside the spectrometers, can be adjusted to tune the magnetic optics to match the muon beam.

The MICE channel is designed to accept beams of emittance 3–10 mm, $p_z = 140$–$240\,\mathrm{MeV}/c$ and $\sigma_{p_z} \approx 20\,\mathrm{MeV}/c$, as they resemble typical input beams into a Neutrino Factory cooling channel [19], and to operate over a range of $\beta_\perp$.

*The 2012 release of the PDG [32] uses this term, rather than "Bethe-Bloch", in recognition of the fact that Bloch's expression for the mean ionization potential is no longer used, having been replaced by more accurate calculations.

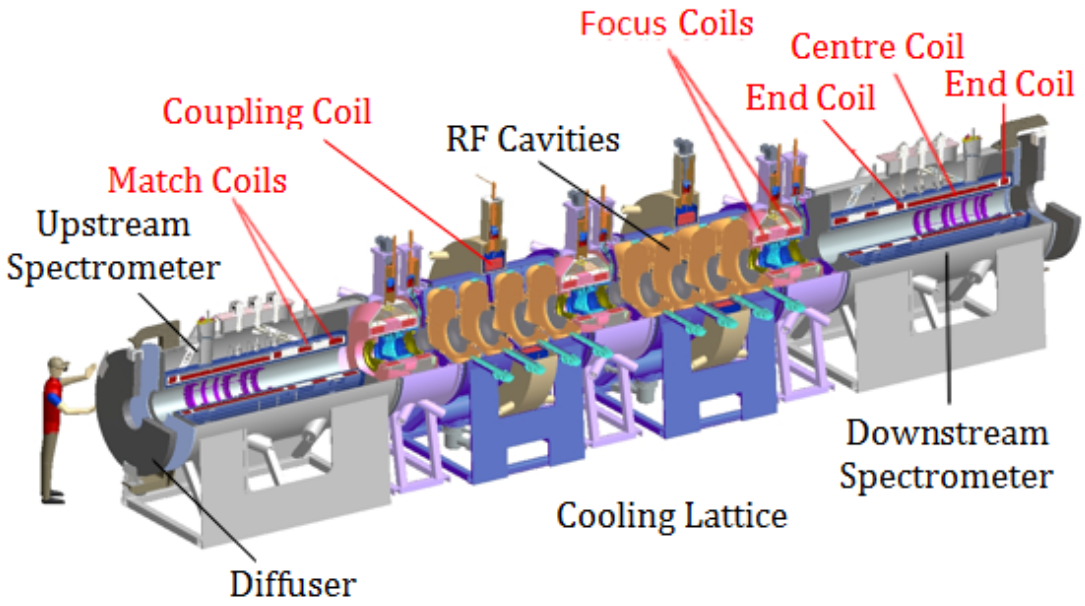

Figure 2.3: The Muon Ionization Cooling Experiment (MICE).

2.4.1 Muon generation and transport

MICE is based at the Rutherford Appleton Laboratory near Oxford, UK, operating parasitically off the ISIS proton synchrotron, as shown in Figure 2.4. A titanium target is dipped into the outer halo of the proton beam, just prior to extraction when the beam energy is 800 MeV. Scattered protons and pions leave the ISIS beam pipe through a thin window into the muon beam line [36], shown in Figure 2.5.

The beam line is designed to capture and transport intense beams of muons into the MICE channel, using a series of quadrupole and solenoid magnets. A quadrupole triplet (Q1-Q2-Q3) transports the beam into a dipole magnet D1, where momentum selection is applied to collect pions with a momentum of 440 MeV/c, excluding neutral particles and protons. The pions are then directed into a 5 T "decay" solenoid where they decay to muons. Further momentum selection is applied by the second dipole magnet D2, followed by two quadrupole triplets (Q4-Q5-Q6 and Q7-Q8-Q9) which transport the beam into MICE where an adjustable tungsten and brass diffuser plate is able to inflate the emittance (through multiple scattering) to up to 10 mm. With the diffuser removed the beam line will deliver a beam of approximately $\varepsilon_x \approx 2$ mm and $\varepsilon_y \approx 3$ mm into the upstream spectrometer solenoid in MICE, as measured in Step I [37], discussed later in this chapter.

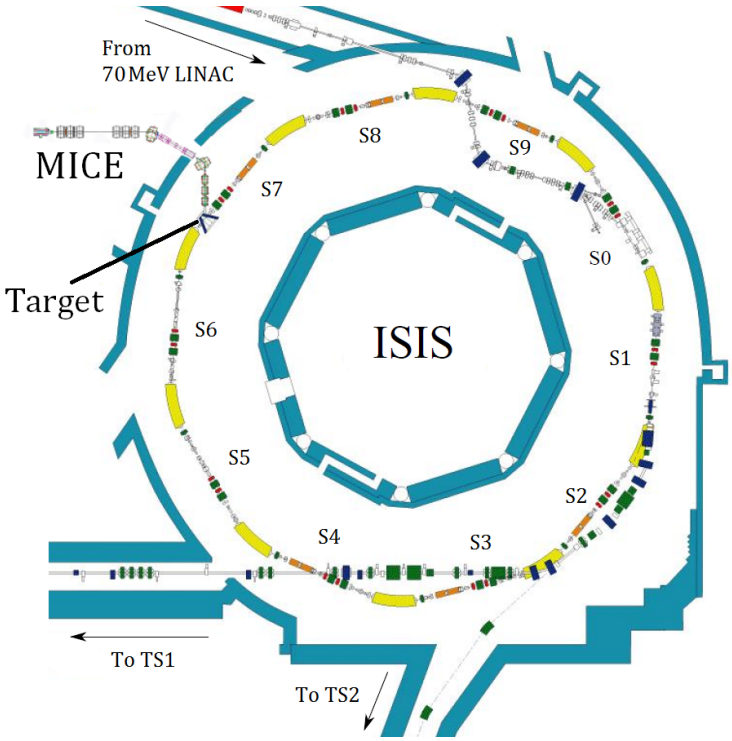

Figure 2.4: A Ti target is dipped into the proton beam at the ISIS synchrotron to produce pions, which are transported into the MICE beam line.

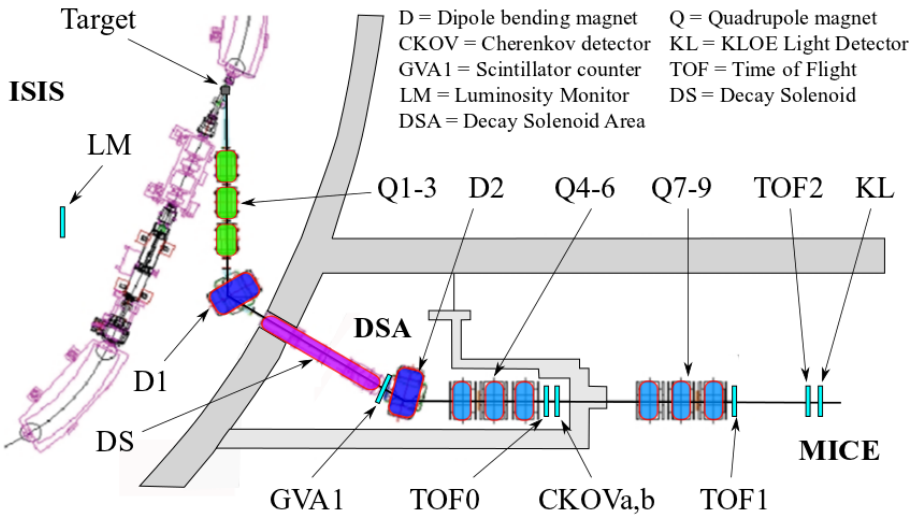

Figure 2.5: The MICE muon beam line transports pions from the target into the decay solenoid, where they decay into muons, through to MICE itself.

2.4.2 Detectors

MICE is designed to measure the 6D coordinates of individual muons before and after the cooling channel. This allows the covariance matrix, which describes the beam, to be measured. The matrix is given in Equation 2.5, from which the emittance and Twiss parameters of the beam are computed. The transverse coordinates of the beam (x, y, p_x, p_y) and p_z are measured inside two trackers, each using five scintillating-fibre planes, positioned within the constant field region in each spectrometer solenoid. The field is generated by a large solenoid magnet and tapered either side by an end coil, as shown in Figures 2.3 and 2.6.

Timing measurements are made by the two time of flight detectors (TOF0, TOF1) placed in the beam line, and a third (TOF2) positioned downstream of the cooling lattice. Each TOF consists of two orthogonally oriented planes of scintillator slabs, read out at each end by photomultiplier tubes. They achieve a timing accuracy of 50 ps [38], permitting a more accurate p_z measurement than can be obtained using the trackers. TOF0, TOF1 and Cherenkov detectors (Ckov) are used for particle identification ahead of the cooling channel, to ensure a muon beam purity of 99.9%. At the downstream end of the cooling channel is a calorimetric system to identify and reject decay electrons, consisting of a pre-shower detector (KL), TOF2 and a electron muon ranger (EMR) [39].

2.4.3 The MICE cooling channel

The complete MICE cooling channel consists of three absorber focus coil (AFC) modules and two sets of normal-conducting RF cavities. It uses a SFOFO design where the magnetic field is flipped at the centre of the absorbers to remove net angular momentum growth. This field configuration is known as “flip mode”. The lattice design is discussed in detail in Section 5.3.2 of Feasibility Study II [19]. 18 superconducting coils produce an axisymmetric field to focus and transport muons through the channel, shown in Figure 2.6. The baseline specification for MICE is to run with a beam of initial $p_z = 200\,\mathrm{MeV}/c$, with a $\beta_\perp = 33\,\mathrm{cm}$ matched into the uniform 4 T field in the spectrometers.

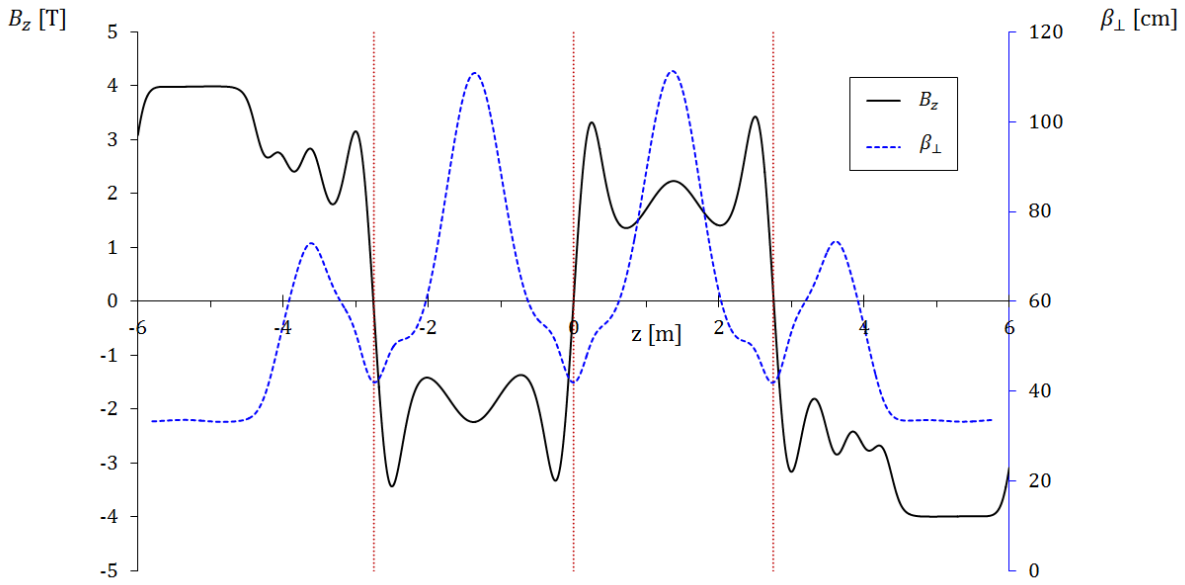

Figure 2.6: The baseline magnetic field (on-axis), $B_z(z)$, and beta function, $\beta_\perp(z)$, in MICE Step VI for $p_z = 200\,\mathrm{MeV}/c$ muons assuming no energy loss or scattering. Vertical lines indicate the position of the centres of each absorber, at which the field is zero and the $\beta_\perp$ is a minimum.

The AFC modules are designed to house the 21 litre LH_2 absorbers, the primary absorber material in MICE. Each absorber is 35 cm in length and 30 cm in diameter, contained with two pairs of 0.18 mm thick aluminium windows, as shown in Figure 2.7. The AFC modules will also be used to house solid absorbers (Al windows are removed), including a 63 mm lithium hydride (LiH) disc. Other materials such as polyethylene are likely to be studied also. Two focus coils surrounding the absorber bring the beam to a tight focus to maximize cooling.

MICE uses 201 MHz RF cavities housed in groups of four in an RFCC module. Large coupling coils around each RFCC module are used to maintain muon transport between the AFC modules. Each RF cavity is 41 cm in length, with 0.16 mm beryllium windows at each end to close the aperture. The MICE RF system is designed to run at gradients of up to 8 MV/m, to re-inject approximately 11 MeV of energy into the beam, roughly the amount of energy lost in an absorber.

Figure 2.8 shows the transverse emittance, ε_n, and longitudinal momentum, p_z, as simulated in Maus/Geant4 in MICE Step VI. A 5.86 mm transverse emittance beam is expected to cool by around 13% down to $\varepsilon_n = 5.08$ mm, and lose approximately $10\,\mathrm{MeV}/c$ in each of the three LH_2 absorbers. RF cavities between the absorbers reinject the lost momentum. Beryllium windows in

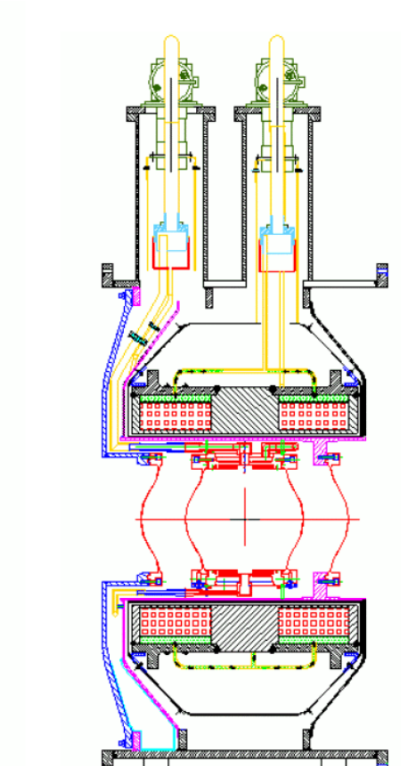

Figure 2.7: Schematic for the absorber focus coil (AFC) module, which contains two sets of aluminium windows to contain a 35 cm width (21 litre) liquid H_2 absorber. The AFC can also house solid absorbers, in which case the windows are removed.

the RFCC modules will generate small amounts of multiple scattering which inflate the emittance slightly, as is shown in the figure.

The MICE cooling channel is being built in stages to reflect the production schedule, as shown in Figure 2.9. Step I was completed in 2010 and involved the commissioning of the muon beam line [36] and the measurement of the beams delivered to MICE [37]. The time of flight counters TOF0 and TOF1 were used to measure the momentum distribution, emittance and dispersion of the beam line, as described in [40]. Step I characterized beams of effective emittance 0.6 – 2.8 mm with central momenta $170 < p_z < 280\,\mathrm{MeV}/c$, and spread, $\sigma_{p_z} \approx 25\,\mathrm{MeV}/c$. The second dipole magnet (D2) introduces dispersion into the beam, which transforms to a dispersion of 90 – 189 mm in x and 0.03 – 0.11 rad at TOF1. Step IV involves a single AFC and will use several absorber materials, including LH_2 and LiH. It is due to begin in 2014 without magnetic fields (using straight muon tracks), followed by full operation (fields switched on) from 2015 to 2016. The complete MICE cooling channel will be operated in Step VI, using three AFCs with RF acceleration, and

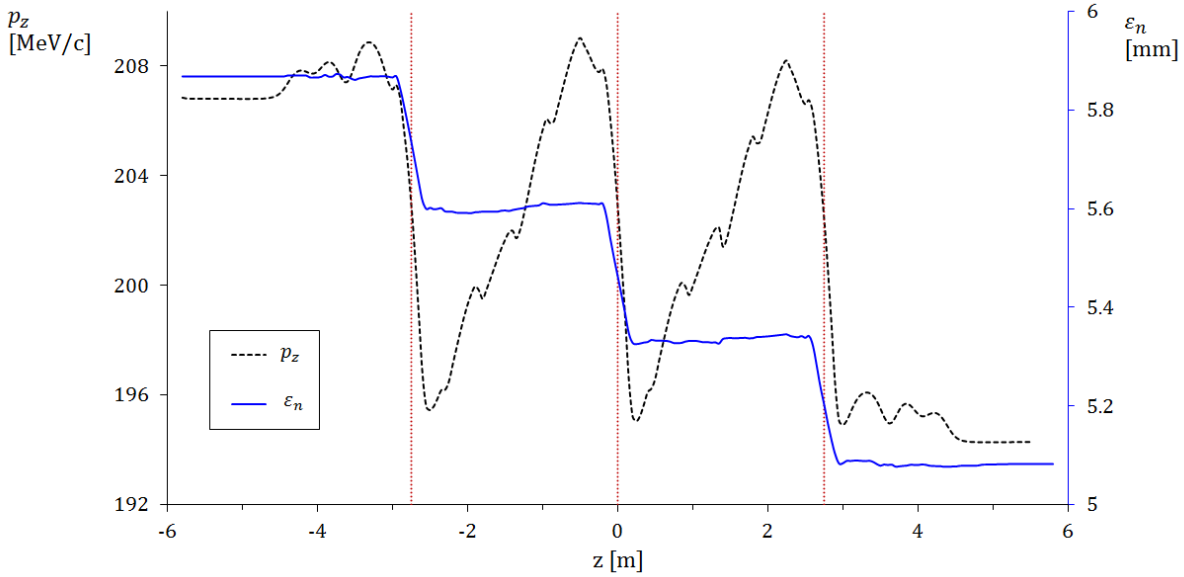

Figure 2.8: Evolution of the longitudinal momentum, p_z, and transverse emittance, ε_n, in Step VI of MICE. Energy loss in each of the three 35 cm LH_2 absorbers, the centres of which are represented by the red vertical lines, reduces the emittance whilst the lost p_z is re-injected using RF cavities placed between the absorbers. The beam scatters and loses a (very) small amount of momentum in the thin Be windows which seal each RF cavity.

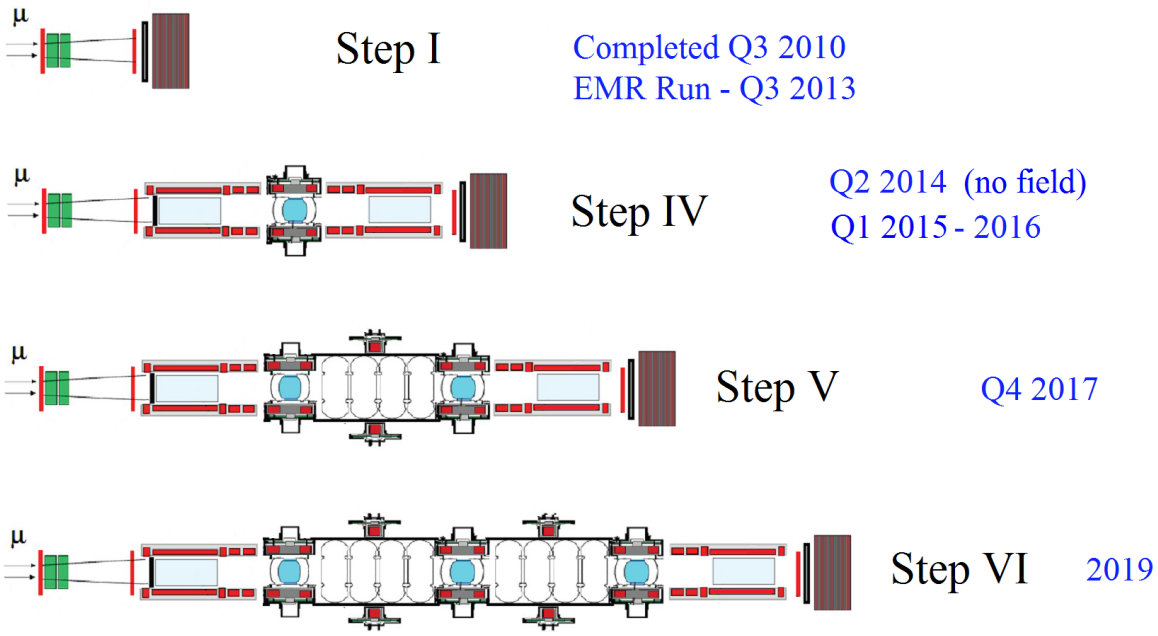

Figure 2.9: The MICE schedule, where Steps II and III were bypassed after changes to the production schedule. The first ionization cooling measurements will be made in Step IV, in both LH_2 and solid absorbers.

is anticipated to begin in Q3 2018. Beams measured in Step I were input into Monte Carlo and simulated through Step VI, and were found to be well-suited to demonstrating cooling as described in [40].

2.5 Summary

The Muon Ionization Cooling Experiment is the first engineering demonstration of a prototype section of an ionization cooling channel. It is being built at the Rutherford Appleton Laboratory in the UK, where it operates parasitically off the ISIS proton synchrotron. The next phase of MICE is Step IV, where the first ionization cooling measurements will be made in 2015. In Chapter 3, the anticipated performance of Step IV is discussed in detail, using the predictions of the cooling formula (Equation 2.9) and Monte Carlo simulation. Predictions are given for total cooling, $\Delta\varepsilon$, and the equilibrium emittance, ε_0, for beams of 140, 200 and 240 MeV/c in seven low Z materials, at $\beta_\perp = 42$ cm. As will be discussed, the predictions of the standard cooling formula disagree significantly with Monte Carlo. The main source of this discrepancy is shown to originate from the approximations used to describe multiple scattering.

Chapter 3

Simulation Studies of MICE Step IV

The performance of MICE Step IV was studied in the Maus Monte Carlo, using the Geant4 physics libraries. Predictions are given for the anticipated cooling and equilibrium emittances in various low Z absorber materials, over a range of muon momenta. Cooling predictions in low Z absorber materials such as liquid H_2 were up to 30% less than estimated using the standard cooling formula, which was unexpected.

The next phase of MICE is Step IV, in which the first ionization cooling measurements will be made in 2015. Step IV will provide the opportunity to characterize the optics of the beam and to understand its behaviour in the focus coils, absorbers and spectrometer solenoids. Cooling will be measured over a range of input emittances, and values for the equilibrium emittance of materials obtained.

This chapter presents the results of Maus Monte Carlo simulation studies of Step IV, giving cooling predictions in seven absorber materials using $p_z = 140, 200$ and $240\,\mathrm{MeV}/c$ muon beams. The equilibrium emittances obtained in Monte Carlo are found to disagree by up to 30% with the standard cooling formula (CF) (Equation 2.9). The chapter begins with a description of Step IV, and of its simulation in Maus.

3.1 Step IV

Step IV of MICE consists of a single absorber contained within an absorber focus coil (AFC) module, with spectrometer solenoids on either side, as illustrated in Figure 3.1. The AFC will house an absorber to demonstrate ionization cooling, which will include a 35 cm LH_2 and a 63 mm LiH absorber. Other materials will be studied also, including polyethylene (C_2H_4). In addition, Step IV will run with a LiH "wedge" absorber [41] as a first test of 6D cooling, which is required for a Muon Collider cooling scheme (as discussed in Chapter 1).

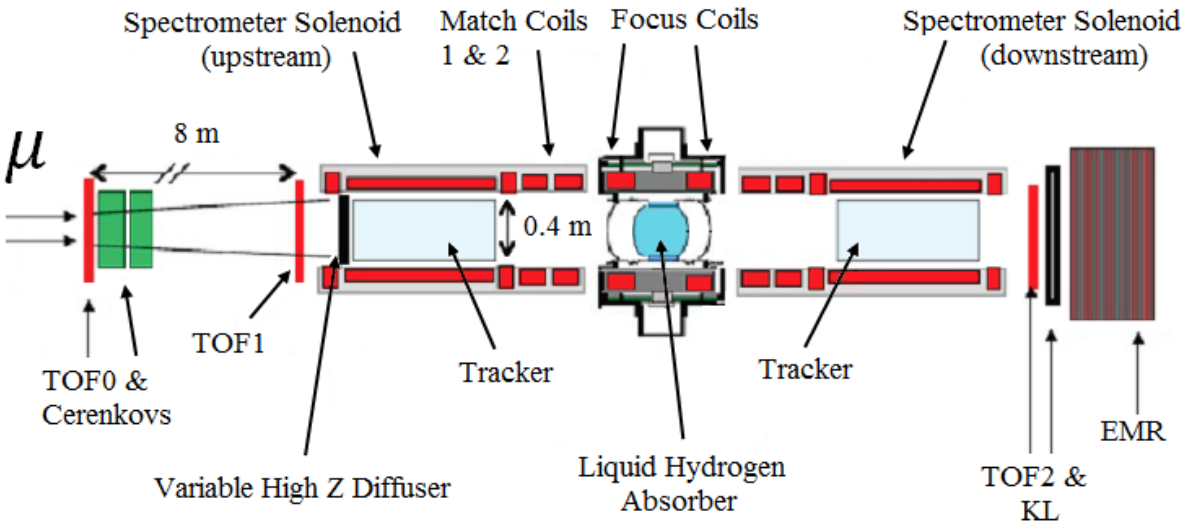

Figure 3.1: Step IV of MICE.

Prior to demonstrating cooling however, the Step IV channel must first be characterized and understood, which is carried out in three stages. The first stage of Step IV is to confirm the alignment of the apparatus using straight-line muon tracks (no magnetic field) through the trackers and downstream PID detectors (TOF2, KL and EMR). The magnetic alignment can then be studied by comparing the transverse momenta of helical tracks (fields switched on) in the two trackers.

When the mechanical and magnetic configuration is well understood the next stage is to then understand how best to match beam into the downstream spectrometer. This will involve fine-tuning the quadrupoles Q4 – Q9 in the beam line (see Figure 2.5) and scanning the available momentum space. Finally, transmission studies will be carried out at different amounts of magnetic focusing.

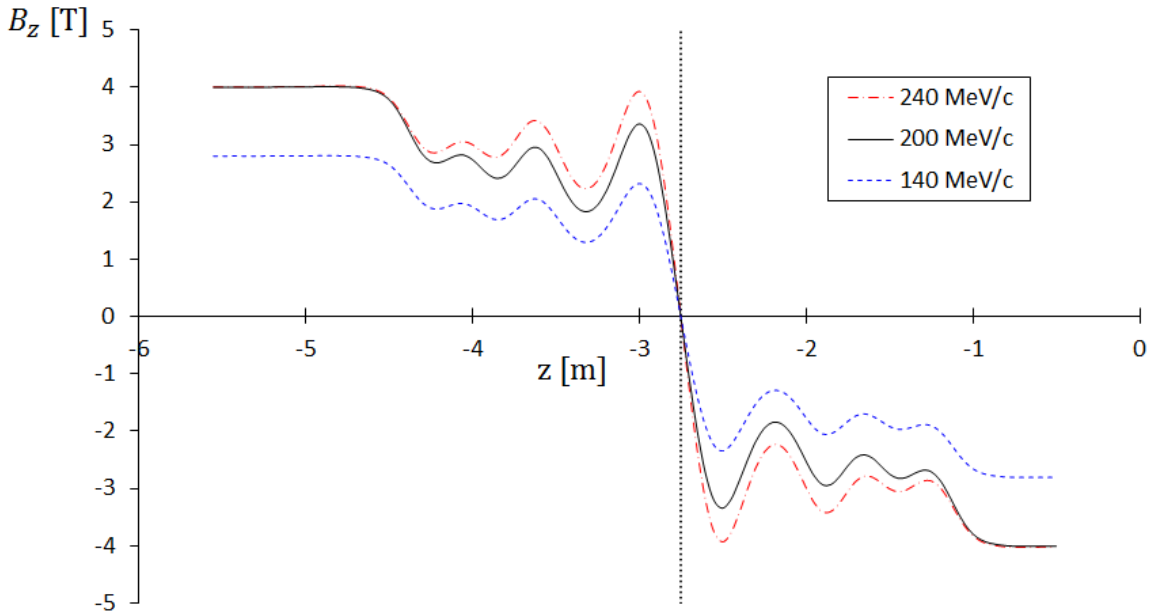

Figure 3.2: Step IV magnetic field (on-axis) in flip mode, for a central $\beta_\perp = 42$ cm.

	z_1 [m]	z_2-z_1 [m]	r_1 [m]	r_2 [m]	J [A/mm^2] 140 MeV/c	200 MeV/c	240 MeV/c
End Coil 1	-6.006	0.111	0.258	0.324	94.63	135.18	135.18
Centre Coil 1	-5.858	1.314	0.258	0.279	106.71	152.44	152.44
End Coil 2	-4.506	0.111	0.258	0.318	89.16	127.37	127.37
Match Coil 2	-4.151	0.200	0.258	0.288	95.99	137.13	150.52
Match Coil 1	-3.712	0.201	0.258	0.303	82.99	118.56	142.48
Focus Coil	-3.06	210	0.263	0.347	79.77	113.95	136.74
Focus Coil	-2.65	210	0.263	0.347	-79.77	-113.95	-136.74
Match Coil 1	-1.99	0.201	0.258	0.303	-82.99	-118.56	-142.48
Match Coil 2	-1.55	0.200	0.258	0.288	-95.99	-137.13	-150.52
End Coil 2	-1.104	0.111	0.258	0.318	-89.16	-127.37	-127.37
Centre Coil	-0.956	1.314	0.258	0.279	-106.71	-152.44	-152.44
End Coil 1	-0.396	0.111	0.258	0.324	-94.63	-135.18	-135.18

Table 3.1: Step IV coil dimensions and currents in flip mode, where z_1 is the upstream edge of the coil, z_2-z_1 the coil length, r_1 and r_2 the inner and outer radii. The current densities, J, are given for the three Step IV operating momenta, for $\beta_\perp = 42$ cm in an empty channel (no absorbers).

Step IV will study cooling in a number of different beams, covering a phase space defined by three parameters, the central longitudinal momentum, p_z, transverse emittance, ε_n, and central beta function, $\beta_\perp$. "Central" refers to the value at the absorber centre. Step IV is anticipated to run at $p_z = 140, 200$ and $240\,\mathrm{MeV}/c$, $\varepsilon_n = 3, 6$ and $10\,\mathrm{mm}$, with central $\beta_\perp$ of $7, 15, 25$ and $42\,\mathrm{cm}$.

The coil dimensions for Step IV are given in Table 3.1, alongside the baseline operating currents for the three central momenta in "flip mode", for $\beta_\perp = 42\,\mathrm{cm}$. Step IV will also run in "solenoid mode" where the field does not change sign at the absorber. The currents for the baseline $200\,\mathrm{MeV}/c$ and $240\,\mathrm{MeV}/c$ case are taken from [42], tuned for an empty lattice without absorber material, giving a 4 T field in the spectrometer solenoids. The $240\,\mathrm{MeV}/c$ currents for the focus and match coils are scaled up from the baseline by 240/200 to account for the higher momentum. At $140\,\mathrm{MeV}/c$, all coil currents are scaled down by $140/200 = 0.7$. Figure 3.2 shows the on-axis magnetic field for Step IV for the three beam momenta at $\beta_\perp = 42\,\mathrm{cm}$.

3.1.1 Simulation in Maus Monte Carlo

The Maus framework (MICE Analysis User Software) [43] allows the performance capabilities of Step IV to be studied prior to data taking, using the Geant4 physics libraries [44] to handle processes such as multiple scattering and energy loss. The BeamMaker application within Maus allows different beam types to be generated for input into the Monte Carlo. Simulations described in this thesis used beams defined by their 4D covariance matrix (Equation 2.5), *i.e.* with a finite emittance, or were straight, on-axis ("pencil") beams defined simply by their initial momentum. Figure 3.3 shows distributions of (x, p_x) at input for a 6 mm emittance beam with initial $p_z = 207\,\mathrm{MeV}/c$. Beams are sampled from multivariate Gaussian distributions and approximately resemble the beams delivered by the MICE muon beam line [37]. A strong step length dependence was discovered in G4MICE, the precursor to Maus, using an older Geant4 version and it is discussed in the following chapter. This instability is not present in Maus using a more recent Geant4 release however. Unless otherwise stated, all simulations were made using Maus/Geant4.9.2.p04.

When simulating Step IV, beams were input into the constant field region of the upstream spectrometer (4 T when running at the baseline $200\,\mathrm{MeV}/c$ currents). The input beams were matched at

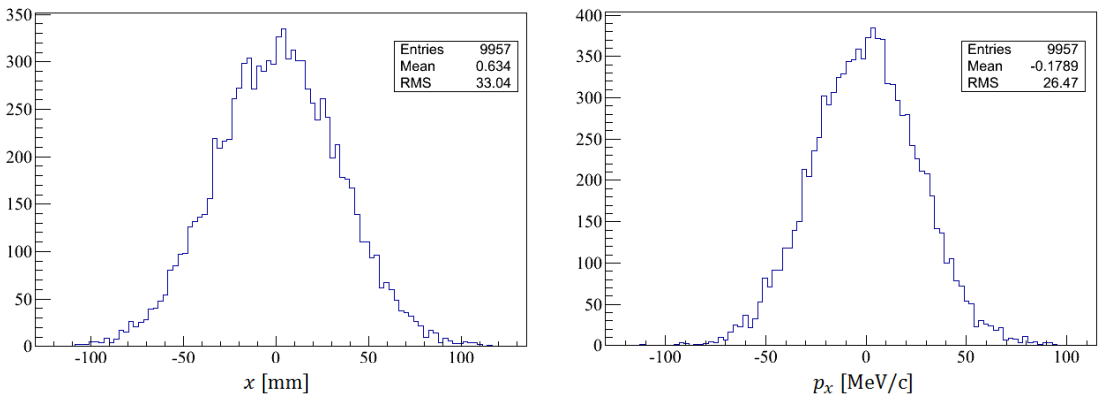

Figure 3.3: Gaussian distributions of x and p_x, as generated in BeamMaker, for $\varepsilon_n = 6$ mm beam in the 4 T solenoidal field. The width of the p_x distribution, σ_{p_x}, is inflated by the mechanical angular momentum required for the muons to orbit in the magnetic field (see Section 2.1 and [30]).

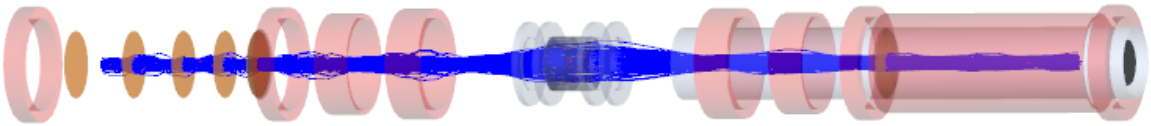

Figure 3.4: Geant4 visualization of a $\varepsilon_n = 6$ mm beam in Step IV.

input to give a fixed $\beta_\perp$ by the matching criterion $\beta_\perp = 1/\kappa$, where $\kappa \simeq (0.15\,\text{GeV}B_z)/p_z\,\text{m}^{-1}$ [30]. For a 207 MeV/c beam in a 4 T field, $\beta_\perp = 34.5$ cm. The evolution of the emittance and Twiss parameters of the beam through the channel are calculated using the standard routines in Maus. Figure 3.4 shows a Geant4 visualization of a 6 mm emittance beam in Step IV. The scintillating-fibre planes of the upstream tracker are shown, along with the coils inside the spectrometer solenoid. The central AFC module houses a 35 cm LH_2 absorber, surrounded by a pair of focus coils. All physical material was removed from simulated geometries, aside from the aluminium safety windows in the AFC and the absorber itself. Magnetic fields were input using a field map, so the effects of muon scraping at large amplitudes by the coil material was not considered.

3.2 Cooling studies

Figure 3.5 shows the evolution of $\beta_\perp$, ε_n and p_z as a function of z for a 35 cm LH_2 absorber in Step IV, as simulated in Maus. At 240 MeV/c beams lose $\approx$ 14 MeV/c in p_z through the absorber, increasing to 19 MeV/c at 140 MeV/c. The emittance clearly drops through the absorber, most significantly at 140 MeV/c with a reduction of 0.5 mm, which is 5% of the input value. The simulated $\beta_\perp$-function departs significantly from the idealized baseline (cf. Figure 2.6) as multiple scattering in the absorber inflates the emittance. A change in emittance produces a corresponding change in $\beta_\perp$, since the rms size of a beam through a thin absorber is constant: $\beta_\perp \varepsilon = \sigma_x$ (Equation 2.3). As a result, $\beta_\perp$ isn't symmetrical about the absorber and the beam is slightly unmatched. When running Step IV however, the coil currents will be fine-tuned to re-match the beam into the channel*.

Figure 3.6 shows the predicted cooling, $\Delta\varepsilon_n$, versus (normalized) input emittance, ε_i, compared with the cooling formula (Equation 2.9) for 35 cm LH_2 and 63 mm LiH absorbers. Simulations used beams of 10,000 muons, with $\sigma_{p_z} = 1$ MeV/c and initial mean $p_z = 207$ MeV/c (corresponding to a "central" momentum of 200 MeV/c). The change in emittance $\Delta\varepsilon_n = \varepsilon_f - \varepsilon_i$, where the normalized input (ε_i) and output (ε_f) emittances of a beam are defined as being the values in the constant field regions of the upstream and downstream spectrometers respectively. A linear fit to the results shows a clear discrepancy with the CF prediction. Error bars for all the cooling plots presented in this chapter are proportional to $1/\sqrt{N_\mu}$ [45], and were approximately 1% of $\Delta\varepsilon_n$. As a result they were ignored.

This discrepancy was studied further by making cooling simulations with other low Z targets, which are listed in Table 3.2. Absorber widths were chosen to achieve an energy loss of ΔE = 10.86 MeV (12.37 MeV/c) in a p_z = 200 MeV/c beam†. Figure 3.7 shows $\Delta\varepsilon_n$ (z) for 200 MeV/c beams in all seven absorbers, illustrating the dependence on both Z and the input emittance. The larger the input emittance of the beam the greater the reduction in emittance. Conversely, the larger the atomic number, Z, of the material the greater the increase in emittance due to scattering. As a result, a 1 mm beam will neither heat nor cool in LH_2 ($\Delta\varepsilon_n = 0$), but will heat by $\Delta\varepsilon_n$ = 0.2 mm in C. A 10 mm beam in LH_2 ($\Delta\varepsilon_n$ = 0.58 mm) cools by over twice the value expected for C ($\Delta\varepsilon_n$ = 0.28 mm). All cooling predictions are given in Table 3.3.

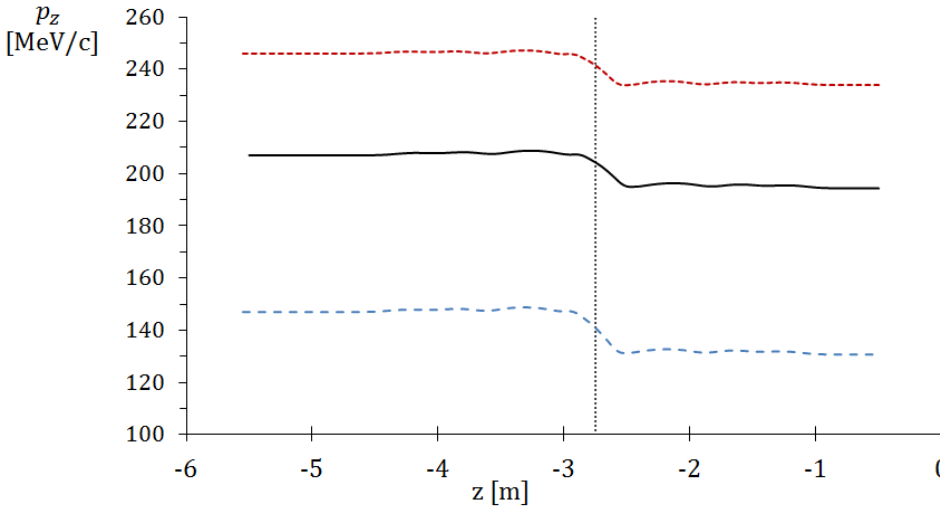

(a) $p_z\,(z)$.

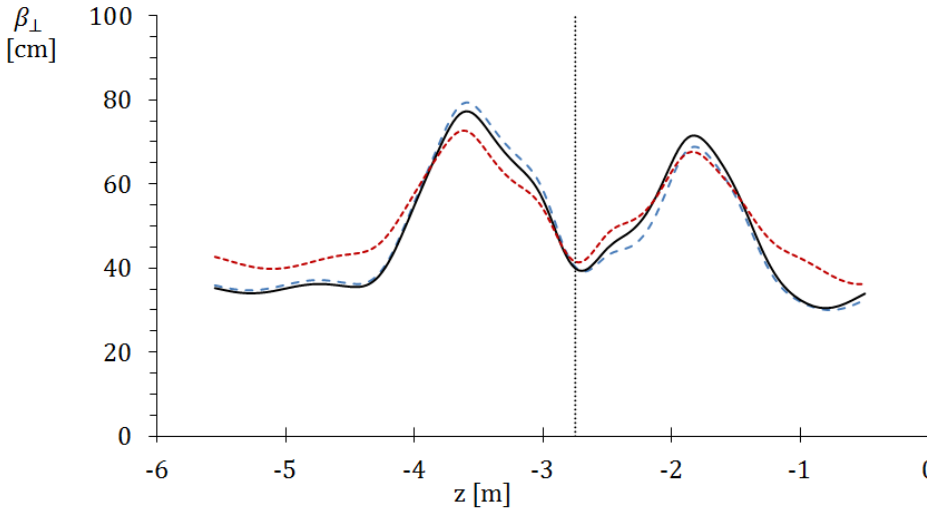

(b) $\beta_\perp\,(z)$.

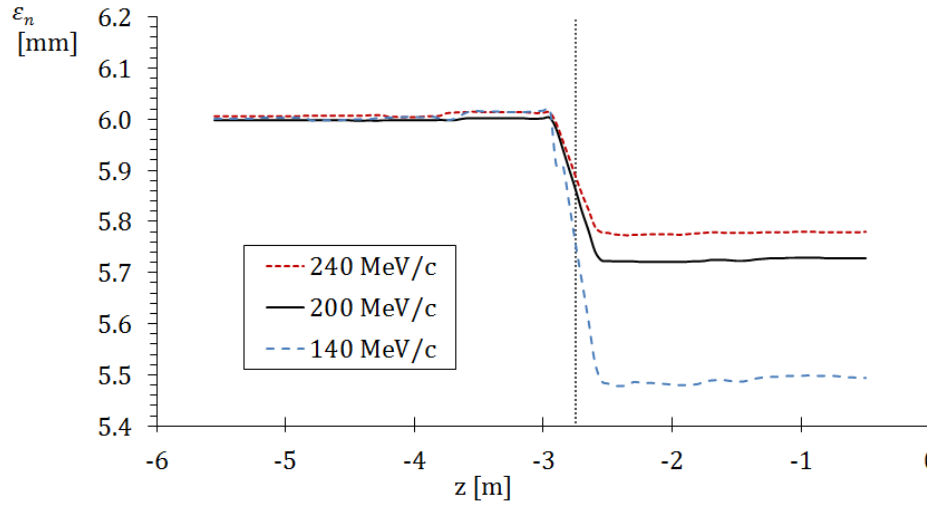

(c) $\varepsilon_n\,(z)$.

Figure 3.5: Maus simulations of a 6 mm emittance beam in Step IV with a 35 cm LH_2 absorber, showing the evolution of its momentum, p_z, beta function, $\beta_\perp$, and emittance, ε_n, along the channel. The vertical dashed lines indicate the centre of the absorber.

3.3 Determination of equilibrium emittance

The equilibrium emittance, ε_0, is defined as being the emittance at which the effects of heating (multiple scattering) and cooling (energy loss) are equal, so that $\Delta\varepsilon_n = 0$ across an absorber. An input beam with $\varepsilon_i < \varepsilon_0$ will increase in emittance (heat) through the material, and reduce emittance (cool) when $\varepsilon_i > \varepsilon_0$. This is illustrated in Figure 3.7, where the sign of $\Delta\varepsilon_n$ changes about ε_0. In LHe, for example, $\varepsilon_0 \approx 2\,\text{mm}$ (at $200\,\text{MeV}/c$, $\beta_\perp = 40\,\text{mm}$), so heating will occur in $\varepsilon_i = 1\,\text{mm}$ beam whilst a 3 mm beam will cool.

As a result, ε_0 can be obtained from Maus by making linear fits to plots of $\Delta\varepsilon_n$ versus ε_i, as shown in Figure 3.8. The interpolated ε_0 values are plotted as a function of (central) p_z in Figure 3.9, and given in Table 3.4. The predicted ε_0 values increase with momentum for all Z, most significantly in carbon, where $\varepsilon_0 = 4.40\,\text{mm}$ at $140\,\text{MeV}/c$ and 6.03 mm at $240\,\text{MeV}/c$, an increase of 37%. In LH_2 the increase was smallest (12%). Also included are the cooling formula (CF) predictions for LH_2 and C, which are calculated using Equation 2.10. Both sets of values suggest a much smaller p_z dependence than predicted in Maus. At all three momenta the CF prediction was 25 – 30% greater than the Monte Carlo values in LH_2. At $140\,\text{MeV}/c$, in the other materials, this excess was significantly smaller, from 2 – 7%. The Monte Carlo ε_0 predictions increase with Z and p_z, which is expected, but at a faster rate than the CF values. The Monte Carlo values in Be and C_2H_4, for example, were 4 – 7% above the prediction at $200\,\text{MeV}/c$ which increases to 12 – 15% at $240\,\text{MeV}/c$. The greatest disagreement was in C, where the CF prediction of 5.04 mm was 26% below the Monte Carlo value (6.03 mm). In LHe, LiH and Li, however, the Monte Carlo and CF agree to within 2% at $240\,\text{MeV}/c$.

The disagreement between Maus/Geant4 and theory was consistent with a previous study in LiH [46] using ICOOL[‡] [47] , in which ε_0 was 25 – 50% less than predicted using the CF. Based upon the predictions of two Monte Carlo simulation codes, which use different physics models, it was concluded that the cooling formula significantly underestimates cooling in low Z materials.

[*] For the purposes of these simulation studies this mismatching is unimportant.
[†] As is the convention for the standard MICE LH_2 and LiH absorbers.
[‡] ICOOL uses Geant3 [48], which is the predecessor to Geant4 and is written in Fortran.

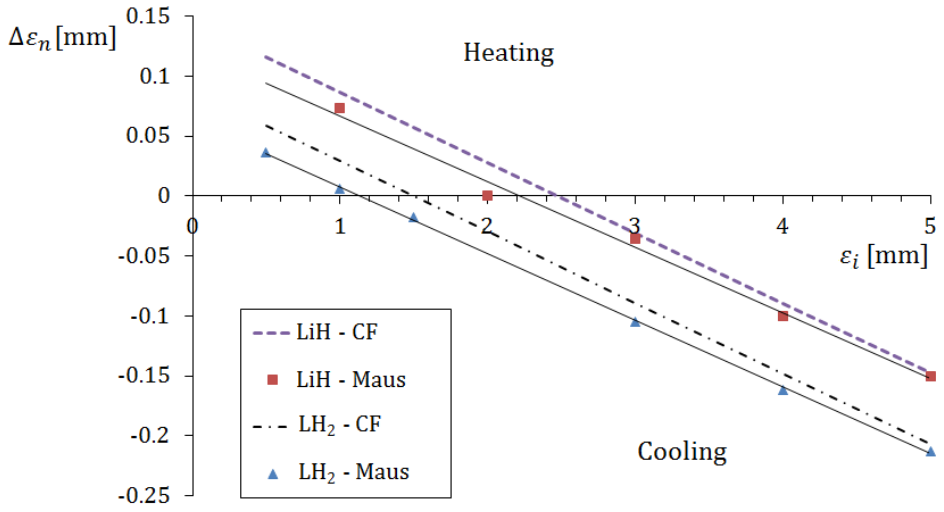

Figure 3.6: Cooling in 35 cm LH_2 and 63 mm LiH absorbers for a beam with initial $\langle p_z \rangle$ = 207 MeV/c (central p_z = 200 MeV/c) as predicted in Maus and the standard cooling formula (CF). Errors were approximately 1% of $\Delta\varepsilon_n$.

Z		Δz [cm]	$\langle dE/dz \rangle$ [MeV g^{-1}cm^2]			ΔE [MeV]		
1	LH_2	35	5.10	4.39	4.21	12.63	10.86	10.42
2	LHe	41.78	2.41	2.08	2.00	12.59	10.86	10.44
	LiH	6.3	2.45	2.09	2.00	12.71	10.86	10.38
3	Li	11.37	2.08	1.79	1.71	12.63	10.86	10.40
4	Be	3.37	2.03	1.74	1.67	12.65	10.86	10.40
	C_2H_4	5.06	2.67	3.87	2.18	12.68	10.86	10.39
6	C	2.84	2.23	1.91	1.82	12.68	10.86	10.39
		p_z [MeV/c]	140	200	240	140	200	240

Table 3.2: Seven absorbers were used in Step IV cooling simulations in Maus. Their thicknesses, Δz, are scaled to give the same amount of energy loss, ΔE, for a 200 MeV/c beam. $\langle dE/dz \rangle$ values are derived from the PDG Review [32].

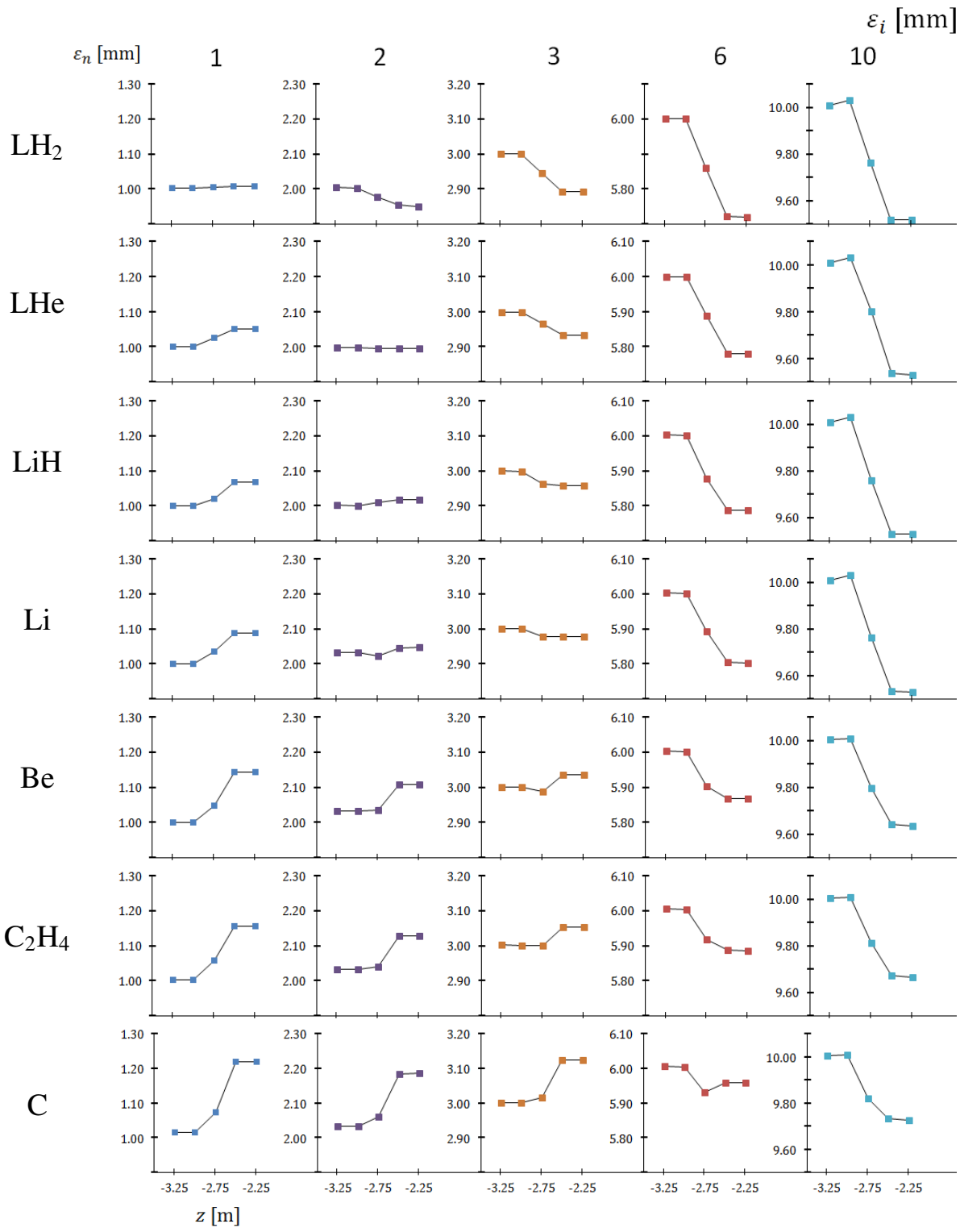

Figure 3.7: Emittance, ε_n [mm], versus z for different absorbers in Step IV, using an input beam of central p_z = 200 MeV/c. Input emittance increases horizontally, from 1–10 mm, as given in the header. Emittance growth occurs when the input emittance is below the equilibrium emittance of the material.

	140 MeV/c			200 MeV/c			240 MeV/c		
	ε_i	ε_f	$\Delta\varepsilon_n$	ε_i	ε_f	$\Delta\varepsilon_n$	ε_i	ε_f	$\Delta\varepsilon_n$
LH_2	1.00	1.007	0.007	1.00	1.01	0.01	1.00	1.01	0.01
	2.00	1.90	-0.10	2.00	1.95	-0.05	2.00	1.96	-0.04
	3.00	2.80	-0.20	3.00	2.89	-0.11	3.00	2.92	-0.08
	6.10	5.59	-0.51	6.00	5.72	-0.28	6.00	5.76	-0.24
	9.92	9.02	-0.90	10.01	9.52	-0.49	10.09	9.67	-0.42
LHe	1.00	1.08	0.08	1.00	1.05	0.05	1.00	1.05	0.05
	2.03	2.01	-0.02	2.00	2.00	0.00	2.03	2.03	0.00
	3.00	2.88	-0.12	3.00	2.93	-0.07	3.00	2.96	-0.04
	6.00	5.58	-0.41	6.00	5.78	-0.22	6.00	5.83	-0.17
	9.86	9.05	-0.81	10.01	9.53	-0.48	10.09	9.69	-0.40
LiH	1.00	1.11	0.11	1.00	1.07	0.07	1.00	1.06	0.06
	2.03	2.02	-0.01	2.00	2.02	0.02	2.03	2.05	0.02
	3.00	2.90	-0.10	3.00	2.96	-0.04	3.00	2.98	-0.02
	6.00	5.61	-0.39	6.00	5.79	-0.21	6.00	5.85	-0.15
	9.92	9.10	-0.82	10.01	9.53	-0.48	10.09	9.74	-0.35
Li	1.00	1.14	0.14	1.00	1.09	0.09	1.00	1.08	0.08
	2.03	2.05	0.02	2.03	2.05	0.02	2.03	2.06	0.03
	3.00	2.93	-0.07	3.00	2.98	-0.02	3.00	2.99	-0.01
	6.00	5.63	-0.37	6.00	5.80	-0.20	6.00	5.86	-0.14
	9.86	9.03	-0.83	10.01	9.53	-0.48	10.09	9.77	-0.32
Be	1.02	1.23	0.21	1.00	1.15	0.15	1.02	1.12	0.10
	2.03	2.14	0.11	2.03	2.11	0.08	2.03	2.09	0.06
	3.00	3.01	0.01	3.00	3.04	0.04	3.00	3.05	0.05
	6.00	5.69	-0.31	6.01	5.87	-0.14	6.00	5.92	-0.08
	9.80	9.10	-0.70	10.01	9.64	-0.37	9.98	9.74	-0.24
C_2H_4	1.02	1.24	0.22	1.00	1.16	0.16	1.02	1.15	0.13
	2.03	2.16	0.13	2.03	2.13	0.10	2.03	2.13	0.10
	3.00	3.04	0.04	3.00	3.05	0.05	3.00	3.06	0.06
	6.00	5.72	-0.28	6.01	5.89	-0.12	6.00	5.93	-0.06
	9.80	9.17	-0.65	10.01	9.67	-0.34	9.98	9.76	-0.23
C	1.02	1.32	0.30	1.02	1.22	0.20	1.02	1.19	0.17
	2.03	2.26	0.23	2.03	2.19	0.16	2.03	2.16	0.13
	3.00	3.15	0.15	3.00	3.13	0.13	3.00	3.12	0.12
	6.00	5.83	-0.17	6.01	5.96	-0.05	6.00	6.00	0.00
	9.80	9.21	-0.59	10.01	9.73	-0.28	9.98	9.81	-0.17

Table 3.3: Change in emittance, $\Delta\varepsilon_n$ [mm], as predicted in Maus for Step IV, at central p_z of 140, 200 and 240 MeV/c. Negative $\Delta\varepsilon_n$ represents cooling, where $\Delta\varepsilon_n = \varepsilon_f$ (output) $- \varepsilon_i$ (input). For the 140, 200 and 240 MeV/c runs the (central) $\beta_\perp = 39, 40$ & 41 cm respectively, the exception being the 140 MeV/c beam in LH_2 where $\beta_\perp = 40$ cm. Simulations used beams of 10,000 muons and $\sigma_{p_z} = 1$ MeV/c.

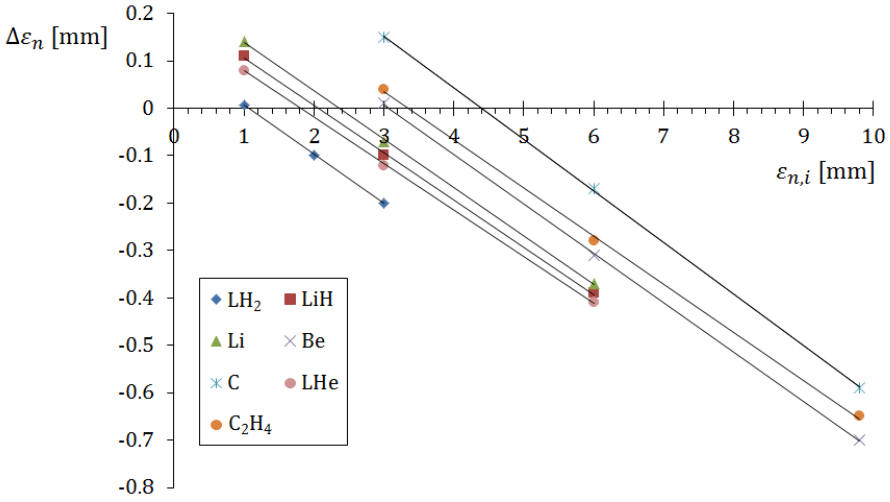

(a) $p_z = 140\,\text{MeV}/c, \beta_\perp = 39\,\text{cm}$ (40 cm in LH_2).

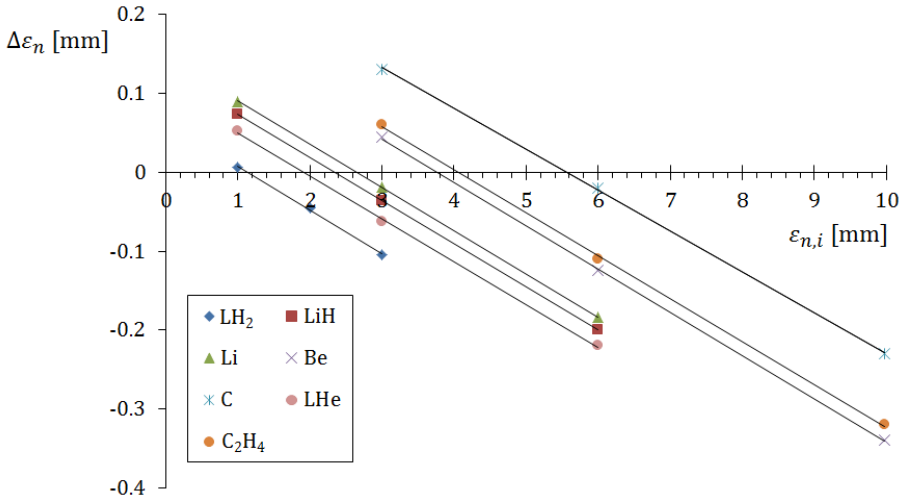

(b) $p_z = 200\,\text{MeV}/c, \beta_\perp = 40\,\text{cm}$.

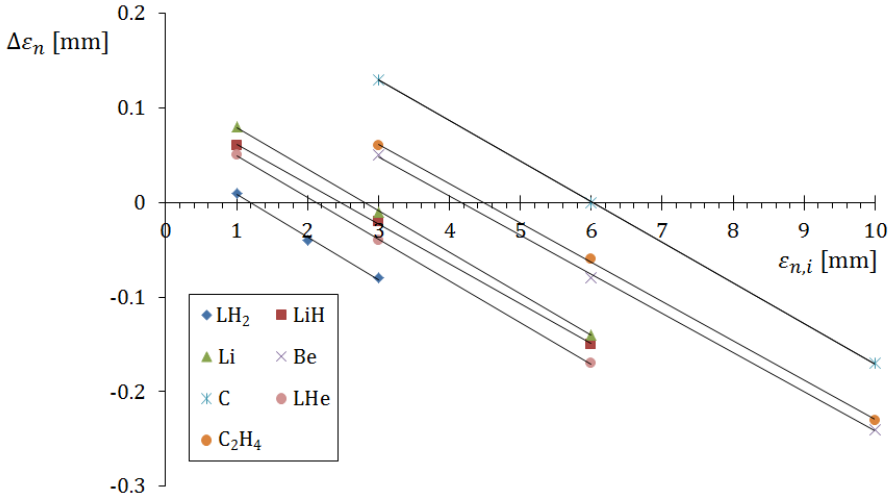

(c) $p_z = 240\,\text{MeV}/c, \beta_\perp = 41\,\text{cm}$.

Figure 3.8: Step IV cooling predictions in Maus, where $\Delta\varepsilon_n$ is the change in emittance, given as a function of input emittance, ε_i, for three central momenta.

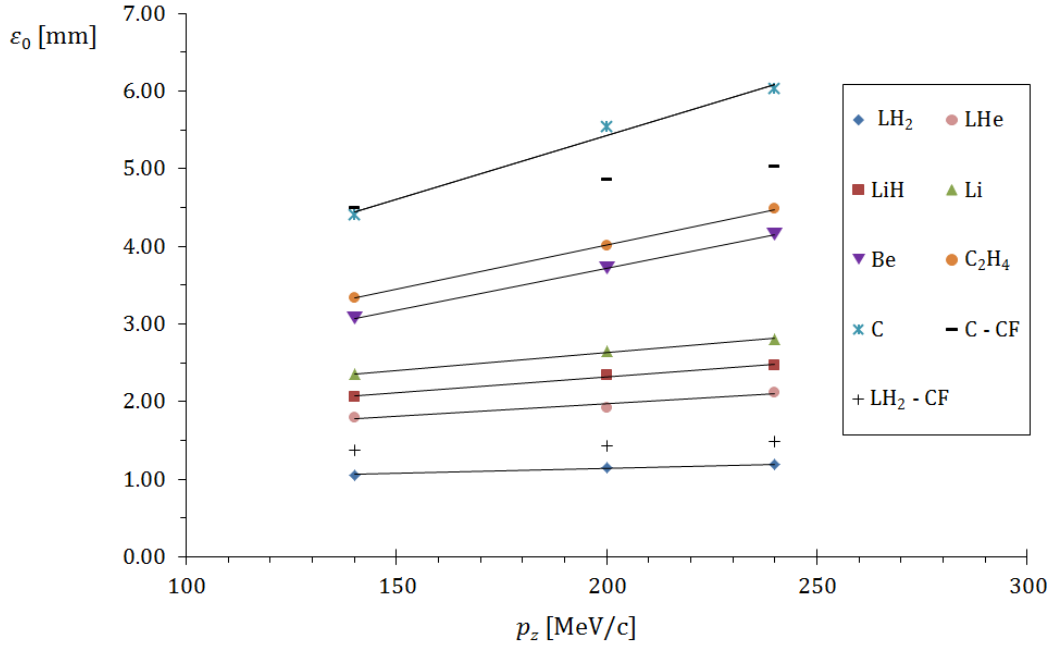

Figure 3.9: Equilibrium emittance, ε_0, as predicted in Maus at central $p_z = 140, 200$ and 240 MeV/c, with $\beta_\perp = 39$ (40 for LH_2), 40 and 41 cm respectively. Cooling formula (CF) values for LH_2 and C are plotted also for comparison.

	140 MeV/c		200 MeV/c		240 MeV/c	
	CF	Maus	CF	Maus	CF	Maus
LH_2	1.37	1.06	1.43	1.14	1.48	1.18
LHe	1.88	1.80	2.02	1.93	2.08	2.12
LiH	2.19	2.06	2.38	2.34	2.46	2.46
Li	2.48	2.35	2.67	2.65	2.76	2.81
Be	3.23	3.07	3.48	3.71	3.60	4.15
C_2H_4	3.58	3.34	3.87	4.01	4.01	4.48
C	4.50	4.40	4.87	5.53	5.04	6.03

Table 3.4: Equilibrium emittance, ε_0 [mm], as predicted in simulations and by the standard cooling formula (CF).

3.4 Summary

MICE will make the first muon cooling measurements in Step IV, which begins in 2014. Step IV aims to measure cooling in different absorber materials, including 35 cm of LH_2 and 63 mm of LiH, across a range of momenta and focusing ($\beta_\perp$). Maus/Geant4 values for the anticipated cooling and equilibrium emittance were found to disagree with the predictions of the standard cooling formula by up to 30%, which was unprecedented. In Chapter 4 this discrepancy will be investigated, where the energy loss and MCS models in Monte Carlo are compared with the approximations used in the cooling formula. A new Monte Carlo model for multiple scattering is described in Chapter 7 as well.

Chapter 4

Multiple Scattering and Energy Loss

Multiple Coulomb scattering and energy loss are the two key physics processes involved in ionization cooling. The disagreement between the cooling formula and Maus/Geant4 Monte Carlo is shown to originate from their treatment of multiple scattering. The cooling formula uses a widely-used scattering approximation known as the Particle Data Group/Highland formula, whereas Monte Carlo typically obtain the actual scattering distributions using a theory of multiple scattering. Both the cooling formula and Monte Carlo use a form of the Bethe stopping power formula to treat energy loss, and agree to a few percent.

Multiple scattering and energy loss are traditionally treated as distinct, independent processes in Monte Carlo, such as in Geant4. This assumption is based on that fact that MCS is predominantly the product of nuclear scatters whereas energy loss derives almost entirely from scatters with electrons. This result is described in the next section. There are slight correlations however, for the inelastic, hard scatters with electrons, which result in large-angle deflections with large energy transfers. Energy losses are very low in scatters with heavy nuclei due to the minimal recoil experienced by the scattering nucleus.

The ELMS (energy loss and multiple scattering) model [49] includes the correlations between energy loss and MCS, using a double differential cross-section (in energy loss and the transverse momentum transfer) derived from first principles, given as Equation 3.20 in [50]. ELMS treats scattering with the entire atom, and is an entirely different approach to traditional Monte Carlo treatments (in which energy loss and MCS are entirely independent processes). It uses tables of energy loss and transverse momentum transfer pairs in thin slices of material to generate probability distributions, after a finite thickness of LH_2, of energy loss and scattering. ELMS is implemented in ICOOL [47], for hydrogen only.

Energy loss in Geant4 is handled using a form of the Bethe stopping power formula [32], which gives the average energy loss of charged particles in matter. Fluctuations in energy loss are modelled on the Landau distribution [51]. ELMS, however, uses a more accurate expression for the energy loss cross-section, given as Equation 3.19 in [50], which avoids the various assumptions contained in the Bethe formula*. Scattering models in traditional Monte Carlo obtain angular distributions using a particular theory of multiple scattering, such as Geant4 which uses Lewis Theory [52]. Multiple scattering theories will be discussed in more detail in Chapter 6. The approximations for energy loss and multiple Coulomb scattering (MCS) used in the cooling formula (CF) are compared with simulations.

4.1 The physical processes

When muons pass through an absorber they interact many times with the constituent atoms in the material. In each interaction the muon scatters off the atomic potential and loses energy. In all but the lightest materials, the atomic potential is dominated by the charge of the nucleus, which scales with Z^2, whereas the net electron charge scales only with Z. As a result, it is reasonable to assume that only nuclear interactions contribute to the distribution of scattering angles, in all but the lightest materials. Scatters with electrons are most important at $Z = 1$, where the nuclear and electron potentials are equal in magnitude. Energy loss however, is inversely proportional to mass of the target, so nuclear scatters account for only a very small amount of energy loss, and the electron scatters dominate. Muon energy losses at $O(200\,\mathrm{MeV}/c)$ are almost entirely through ionization, since Bremßtrahlung and e^+e^- pair production losses are negligible below GeV energies. Collisions with electrons can result in atomic energy level excitation or "hard" collisions where the electron can be ejected from the atom.

The strong dependencies of scattering and energy loss can be shown using kinematics, as illustrated in Figure 4.1. An incident muon, of energy E and momentum p, collides with a constituent electron (in the rest frame of the electron) in an atom. The muon scatters elastically off the electron into an angle θ losing kinetic energy, ν, which is transferred to the electron. Using $E^2 = p^2 + m^2$ one can

*Holmes discusses these assumptions in Section 3.8 of [50].

write the following for the outgoing muon and electron:

$$(m_e + \nu)^2 - (\vec{p} - \vec{q})^2 = m_e^2$$
$$(E - \nu)^2 - \vec{q}^2 = m_\mu^2,$$

which can be manipulated to give an expression for $\vec{p}.\vec{q}$. The angle of scattering, θ, can then be expressed using the definition of the scalar product ($|p||q|\cos\theta = \vec{p}.\vec{q}$) to give the following result:

$$\cos\theta = \frac{p^2 - (E + m_e)\nu}{|p||q|}, \tag{4.1}$$

where $|q| = \sqrt{(E - \nu)^2 - m_\mu^2}$.

Figure 4.2 shows the scattering angle, θ, and energy transfer, ν, of a muon when scattering with a free electron, a proton and a beryllium nucleus. For a given θ, ν is several orders of magnitude greater in a electron scatter than with a nucleus. For a given ν, however, a muon will experience a far larger θ with a nucleus than with an electron. The minimum scattering angle in an electron collision corresponds to an energy transfer equal to the binding energy of the particular shell; below this energy the electron remains bound and cannot be considered "free". This minimum angle is considered to approximately correspond to the angle θ_1^e, which is calculated using Equation 5.9, and will be discussed in Chapter 5.

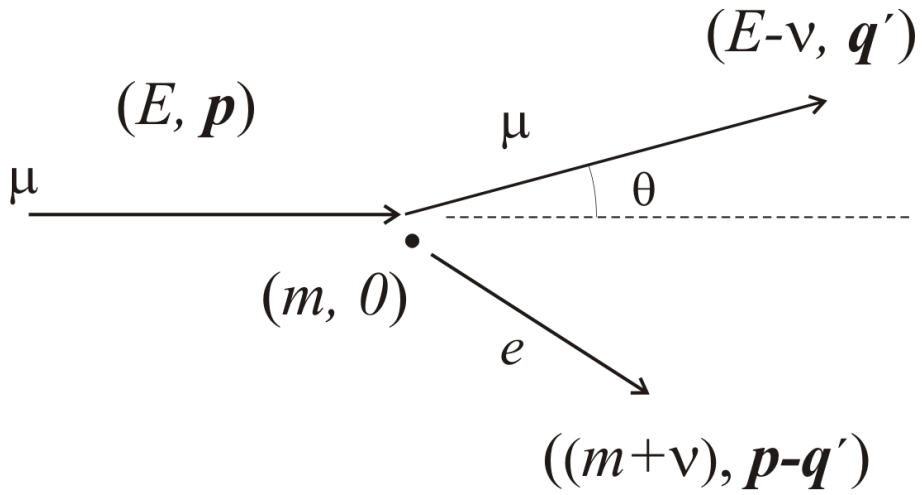

Figure 4.1: Kinematics of an incident muon scattering off an electron.

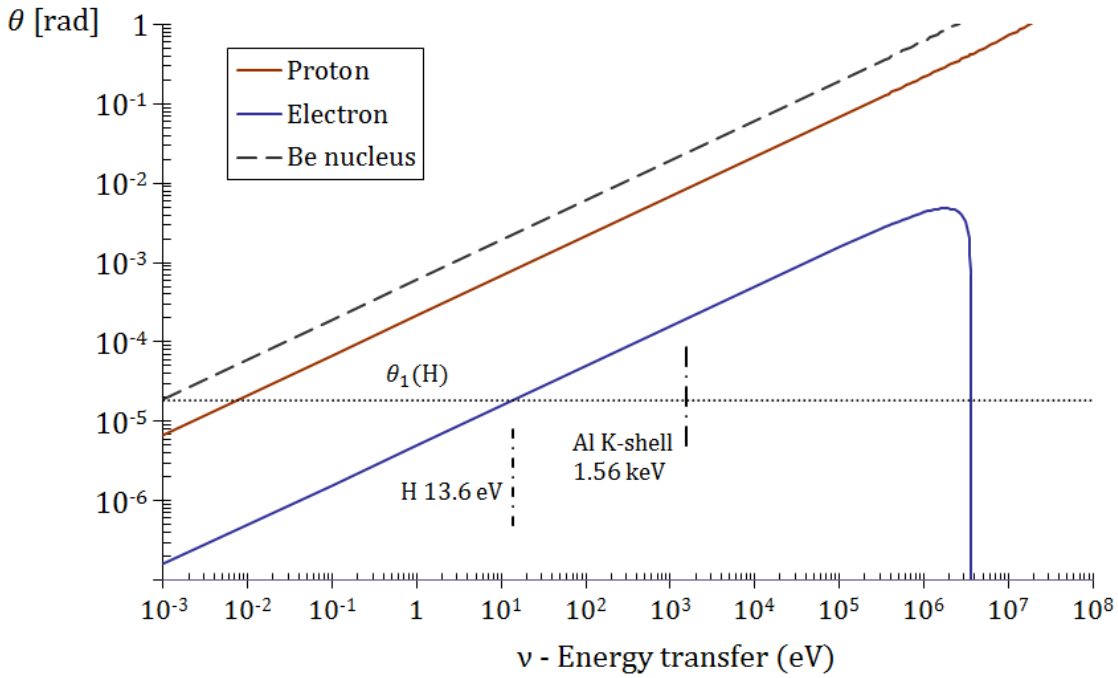

Figure 4.2: The kinematic lines of scattering angle, θ, and energy transfer for a 200 MeV/c incident muon in an elastic collision with an electron, proton and Be nucleus. The dashed line shows the screening angle, θ_1, for a hydrogen atom, as predicted by Equation 5.9. This angle corresponds to an energy transfer equal to the ground state electron binding energy in hydrogen (13.6 eV), implying that $\theta_1 \approx \theta_1^e$. For heavier elements such as aluminium, electrons are more tightly bound in the innermost shell and the binding energy is larger, therefore θ_1^e is greater.

4.2 Monte Carlo multiple scattering models

Monte Carlo treatments of MCS fall into two main categories[†]: "detailed" and "condensed" simulation, as discussed in Section 6.1.1 of [53]. Condensed simulation, which is the most common approach, reduces processing time by segmenting particle tracks into "steps", in which a large number of collisions occur. The size of each step, known as the step length, is much greater than the mean free path of the particle. At the end of each step the global effects of collisions are computed by sampling distributions, characteristic of the chosen step length. These distribution include energy loss, net displacement, and the incident particle's change of direction. Distributions of scattering angles after a step are obtained from a single-scattering cross-section using a particular theory of multiple scattering, and will be discussed in more detail in Chapter 6. Detailed Monte Carlo codes simulate all particle collisions according to the cross-section, so the treatment is exact. This approach is, however, only practical when the number of collisions is small, *i.e.* at low energies or in thin absorbers.

All Maus results presented in this thesis were made using the default, *Urban* scattering model in Geant4, which is a condensed treatment, where the step length can be defined by the user or set automatically. A description of the MCS models in Geant4 is given in [55]. A strong step length dependency was found in G4MICE, which was used to simulate MICE prior to the development of Maus, and used an older Geant4 release (4.9.2.p04). Geant4 gives the user some flexibility over the maximum length in which it steps particles through the geometry (using the G4StepMax parameter), assuming it is above the minimum length required by the physics processes [53]. Reducing the step length increases the total number of simulation steps Geant4 must process, and consequently is much more CPU intensive.

Figure 4.3 shows the change in emittance, $\Delta\varepsilon_n$, for G4MICE simulations of Step IV with a 35 cm LH_2 absorber, at different step lengths, as set by the Geant4 parameter G4StepMax. Increasing the step length from 0.1 mm to 100 mm lead to a $\approx 45\%$ increase in ε_0, which is a very strong effect. The Maus values are independent of step length. The root of the problem was not identified, and

[†] A relatively new approach is "mixed" Monte Carlo, which uses detailed simulation for the hard, inelastic collisions (of which there are relatively few), but use a condensed treatment for the very large numbers of soft, elastic collisions at small angles [54].

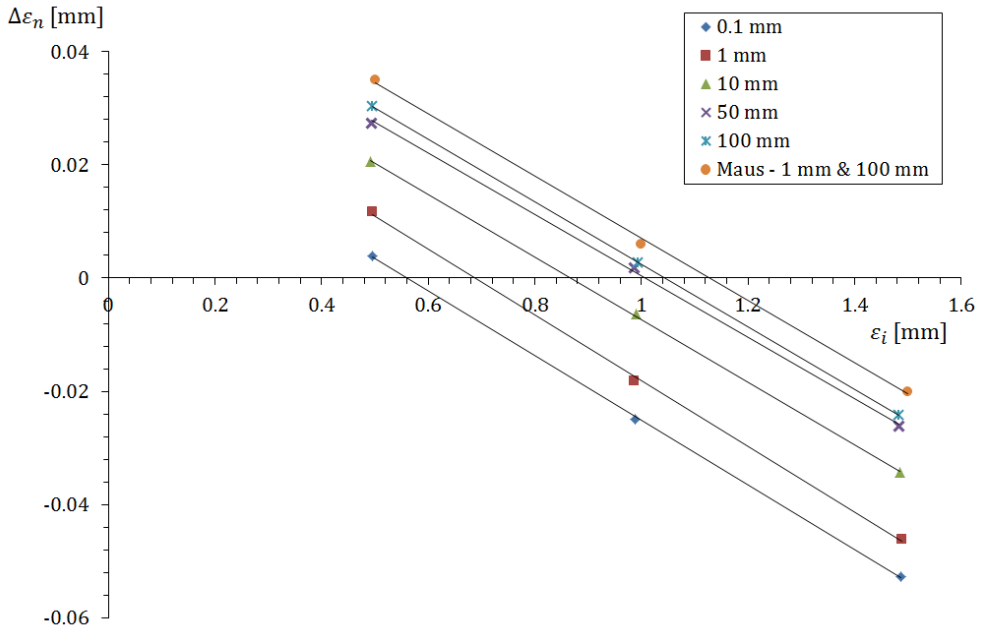

Figure 4.3: A step length dependency was observed in G4MICE/Geant4.9.2.p04, which was not observed in Maus. Simulations are for Step IV with 35 cm of LH_2 with initial $p_z = 207\,\text{MeV}/c$.

partly motivated the development of new software (Maus), using a more recent Geant4 release. Whilst this problem wasted significant amounts of time it did highlight how complex and opaque the MCS models within Geant4 are to the general, non-specialist user. In light of this, and the disagreement between Monte Carlo and the CF, a new Monte Carlo MCS model was developed to see whether scattering distributions could be obtained using only the simple, fundamental physics. This model will be discussed in detail in Chapter 7.

4.3 Further studies

The cooling formula is an approximate expression giving the net change in emittance as the difference between an energy loss term and a multiple scattering term. In light of the observed disagreement with Monte Carlo (in both Geant4 and ICOOL) the energy loss and MCS approximations will now be compared, separately, with the predictions given in Monte Carlo models.

4.3.1 Multiple scattering

As shown in Chapter 2, the standard cooling formula (CF) uses the following expression to account for multiple scattering:

$$\frac{d\langle\theta_0^2\rangle}{dz} = \left(\frac{13.6\text{ MeV}}{p\beta}\right)^2 \frac{1}{X_0}.$$

The expression is based on the formula given in the PDG Review [32] which gives the rms width of the central 98% of a projected (2D) angular distribution (assumed to be Gaussian) as:

$$\theta_0 = \frac{1}{\sqrt{2}}\theta_{space}^{rms} = \frac{13.6\text{ MeV}}{p\beta}\sqrt{\frac{\Delta z}{X_0}}\left[1 + 0.038\ln(\Delta z/X_0)\right], \tag{4.2}$$

which has a stated accuracy of 11% or better for $10^{-3} < \Delta z/X_0 < 100$. The expression is widely used by experimentalists, but its origins are not commonly known and date back to the 1941 paper of Rossi and Greisen [34], presented also in Rossi's 1955 book [56]. The log term was added by Highland in 1975 [57]. The PDG formula is also used as a parameter in the Geant4 MCS models[‡], as discussed in the Geant4 documentation [53]. The expression is derived, and discussed in detail, in Chapter 5.

Maus simulations were made in eleven absorbers to evaluate the agreement with the PDG approximation, with and without the natural log term. Absorber thicknesses, given in Table 4.1, were scaled to give the same fraction of a radiation length as the 63 mm LiH MICE absorber ($\Delta z/X_0 = 6.49\%$). As a result the PDG values θ_0 were fixed, for all materials, to 17.64 and 19.68 mrad (no log term). Simulations used "pencil" beams of 100, 000 muons, directed along the central axis ($x, y = 0$, $p_{x,y} = 0$) with initial $p = p_z = 207\,\text{MeV}/c$. Figure 4.4 shows distributions of θ_x for the LH_2 and carbon absorbers, where the central 98% is shown by the red curves. The rms width of the central 98% was 15.19 mrad in LH_2 and 16.46 mrad in C, both of which are less than the PDG prediction.

Figure 4.5 shows the projected rms projected angle, θ_0, as a function of Z, obtained in Maus,

[‡]Labelled as the Highland-Lynch-Dahl formula.

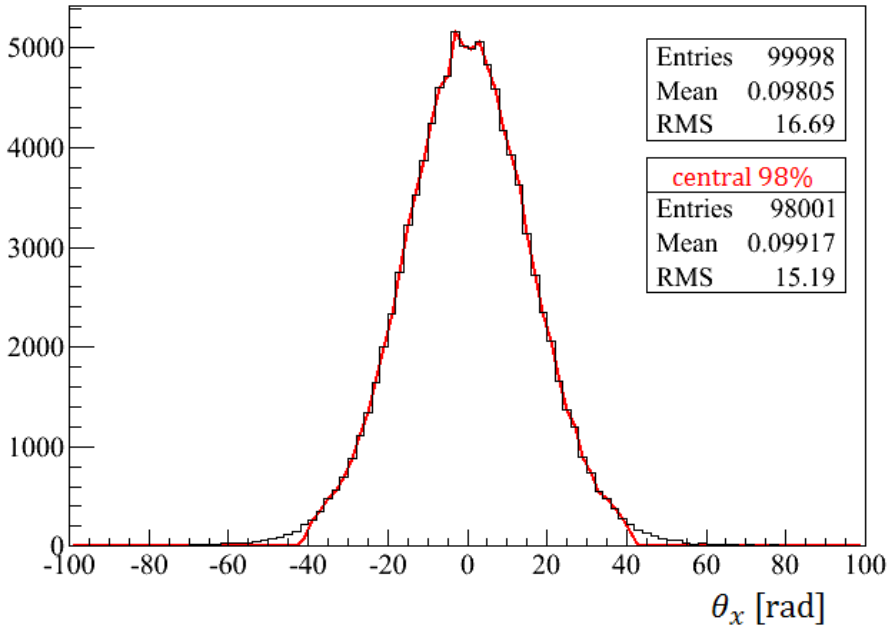

(a) 57.79 cm LH_2

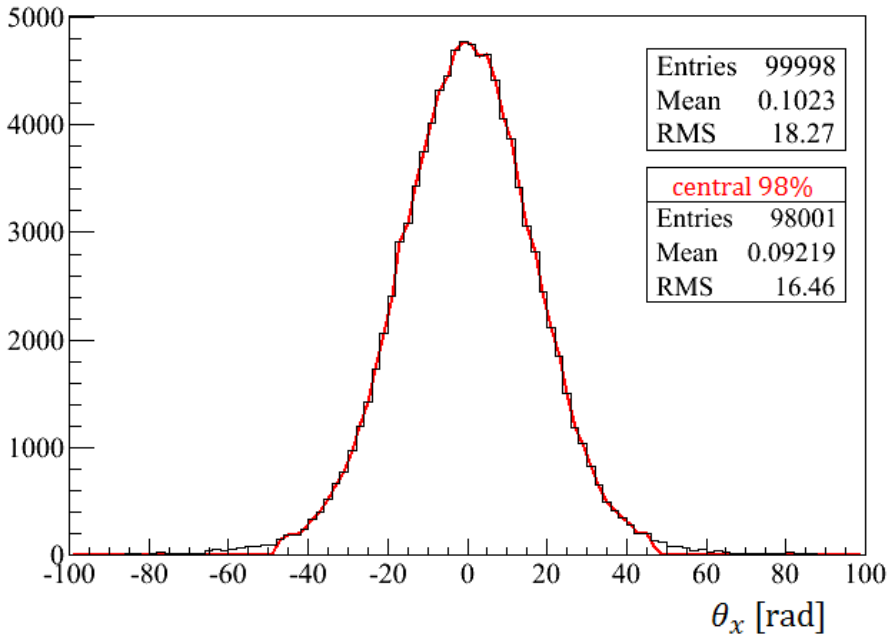

(b) 1.39 cm C

Figure 4.4: Distributions of θ_x in Maus simulations, using $p_z = 207\,\text{MeV}/c$, straight-line beams. RMS widths ($\equiv \theta_0$) are given for the full distribution and the central 98% (red curve). The PDG formula gives $\theta_0 = 17.64\,\text{mrad}$ (for the central 98%) for both targets.

Z		Δz [cm]	θ_0 [mrad]			ΔE [MeV]	
			Maus (98%)	PDG	PDG no log (CF)	Maus	Bethe
1	LH_2	57.79	15.19	17.64	19.68	17.89	18.04
2	LHe	48.96	16.24	17.64	19.68	12.67	12.81
	LiH	6.30	16.26	17.64	19.68	10.75	10.88
3	Li	10.06	16.27	17.64	19.68	9.52	9.67
4	Be	2.29	16.36	17.64	19.68	7.33	7.42
	C_2H_4	3.09	16.07	17.64	19.68	6.53	6.67
6	C	1.39	16.46	17.64	19.68	5.27	5.33
13	Al	0.58	16.52	17.64	19.68	2.62	2.71
22	Ti	0.23	16.74	17.64	19.68	1.61	1.67
26	Fe	0.11	16.51	17.64	19.68	1.35	1.40
29	Cu	0.09	16.60	17.64	19.68	1.24	1.26

Table 4.1: Scattering and cooling predictions, for 207 MeV/c beams.

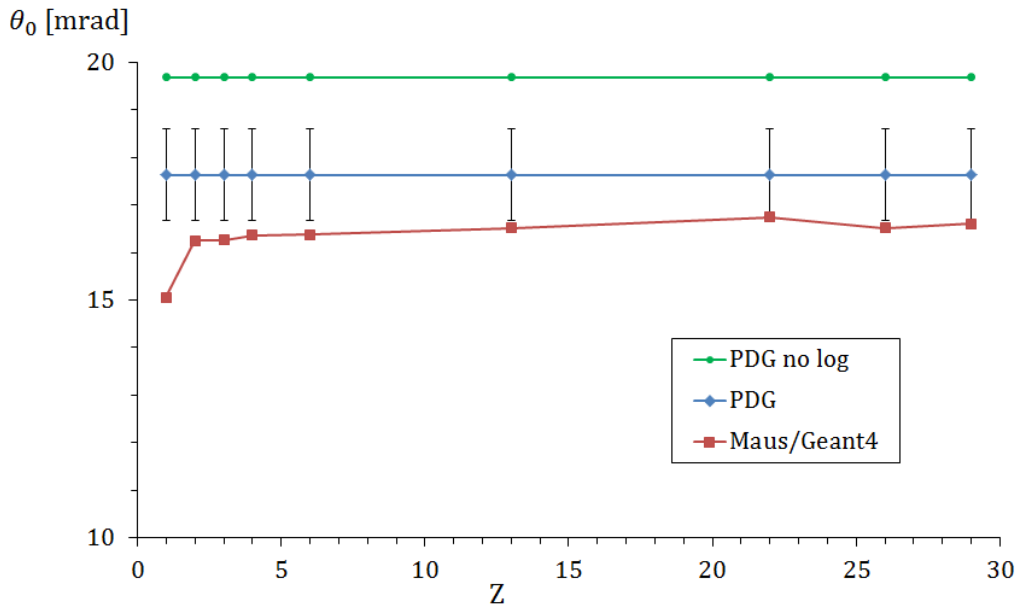

Figure 4.5: Rms projected angle of scattering, θ_0, as implicit in the cooling formula (which uses the PDG approximation without the log term) compared with the full PDG expression and Maus/Geant4 Monte Carlo.

compared with the PDG formula, with and without the log term. In LH_2 the Maus value was 15% less than predicted by the (full) PDG formula, and 6–8% less in higher Z materials. Omission of the log term in the PDG formula increases the disagreement by as much as $\sim$ 10%. Such a comparison between Monte Carlo and theory requires a caveat however, regarding the angular range of histograms. Widths from Monte Carlo are dependent on the probability of very large angle scatters, since they define the range (upper limit) of the distribution. The PDG formula gives the rms width assuming a Gaussian distribution (the central 98%) including angles up to θ_2 (Equation 5.10), above which the cross-section drops rapidly to zero [56]. θ_2 is associated with the finite size of the nucleus, and is discussed in Section 5.3. The disagreement between Monte Carlo and the CF is particularly important due to the fact that it appears most significant in hydrogen, i.e. at lowest Z, the most suitable medium for ionization cooling. Whilst the CF is often used as a rough approximation, it is not suitable for cooling channel performance studies. Feasibility Study II [19], for example, used ICOOL. It remains important, however, to understand the discrepancy, and to identify it. MICE Step IV has the capacity to measure scattering distributions, simultaneously with cooling (*i.e.* using helical tracks) and using straight tracks, with no magnetic field. Both methods will require corrections to account for the tracker resolution and multiple scattering however, as will be discussed in Chapter 8.

4.3.2 Energy loss

The cooling formula uses the mean energy loss predictions of the Bethe formula, which is described in [32]. Table 2.1 gives $\langle dE/dz \rangle$ values in low Z elements for muons of 200 MeV kinetic energy. Figure 4.6 compares the predictions of the Bethe formula with the energy loss models in Maus, for material of $Z = 1$ (LH_2) to 29 (Cu). Absorber widths and ΔE values are given in Table 4.1. Simulations used pencil beams of 100,000 muons with initial $p_z = 207\,\text{MeV}/c$. Monte Carlo values were within $\approx 2\%$ of the Bethe predictions in all materials apart from Al, Ti and Fe, where agreement was slightly worse at about 4%.

Figure 4.7 shows energy loss distributions for the standard 35 cm LH_2 and 63 mm LiH MICE absorbers plus a 10 cm LH_2 target, obtained in Maus. As expected the distributions consist of

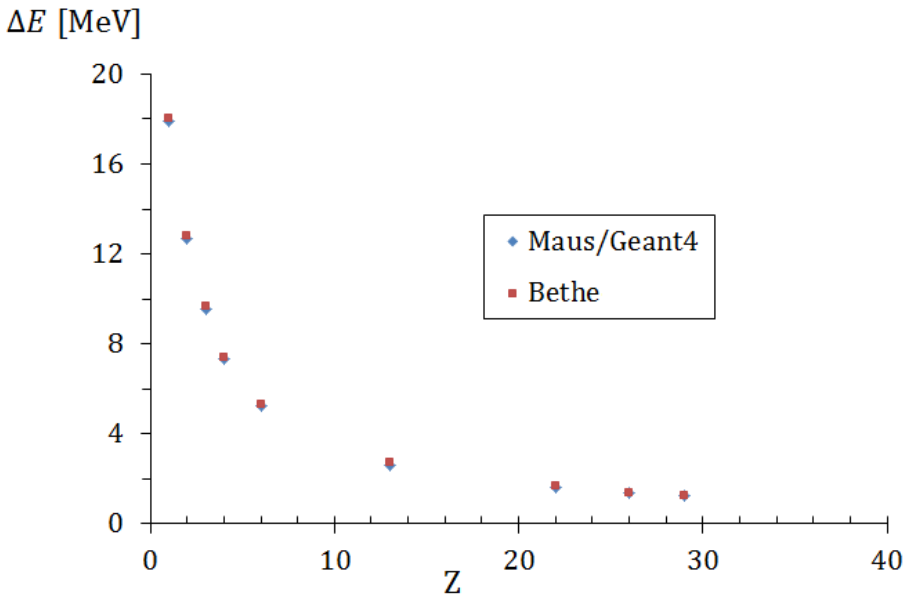

Figure 4.6: Mean energy loss, ΔE, predictions of the Bethe equation and Maus, using straight-line beams with $p_z = 200\,\text{MeV}/c$. Absorbers thicknesses, Δz, are scaled so $\Delta z/X_0 = 6.49\%$, and are given in Table 4.1.

an asymmetric Gaussian with a high E tail, and are known as Landau distributions [51]. Large fluctuations in ΔE are due to small numbers of collisions with large energy transfers. The rms width of energy loss distributions is known as the Landau width.

As shown in Figures 4.7b and 4.7c, the Landau width of the 35 cm LH_2 and 63 mm LiH distributions is approximately 1 MeV. The MICE trackers have an energy resolution of approximately 3.49 MeV so unfortunately the width cannot be measured directly. The greatest source of error lies in the measurement of p_z, where the tracker resolution is $\sigma_{p_z} = 4.58\,\text{MeV}/c$ [58], because of the difficulty in measuring p_z for muons with low transverse momenta. Whilst the TOFs and EMR have a better p_z resolution, $\approx 3.5\,\text{MeV}/c$, they are unlikely to help achieve a sensitivity sufficient to observe the Landau width.

The energy loss models in ELMS were compared with an older Geant4 release (Geant4.5.2p02) in Section 3.2 of [50], and found to agree to a few percent. In 10 cm of LH_2 ELMS predicts a Landau width of 0.46 MeV with a mean of 3.05 MeV, compared with 3.09 MeV (rms) in Geant4.5.2p02. As shown in Figure 4.7a, Maus, using Geant4.9.2.p04, gives better agreement with ELMS, predicting an rms of 0.57 MeV and mean value of 3.02 MeV.

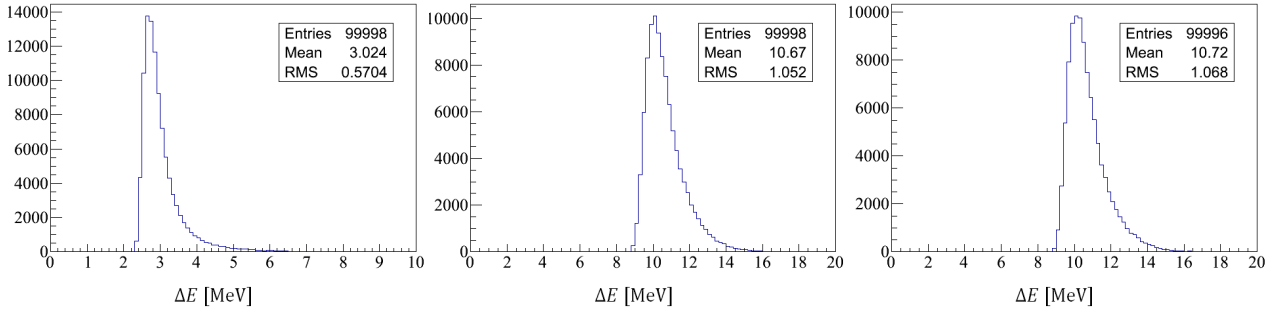

(a) 10 cm LH_2 (b) 35 cm LH_2 (c) 63 mm LiH

Figure 4.7: Energy loss distributions generated in Maus/Geant4, using straight-line beams of 100,000 muons with initial $p_z = 207\,\text{MeV}/c$.

4.4 Summary

Cooling studies in Maus and ICOOL have shown disagreement with the standard cooling formula by up to 30%. Whilst the cooling formula is no more than a useful approximation, it is widely used, so its accuracy is important. The disagreement seems to lie in the the treatment of multiple Coulomb scattering, which inflates emittance. Maus simulations predict rms scattering angles of up to 23% less than expected from the PDG expression. Additional step length dependency problems in past Monte Carlo releases added additional uncertainty as to the reliability of the MCS models, unaided by the fact that the actual physics contained within these models is largely invisible to the average user.

The perceived inaccuracy in the cooling formula combined with uncertainties in the Monte Carlo MCS models emphasized the need to go right back to the fundamental physics of scattering. In Chapter 5, the origins of the Rossi-Greisen and PDG approximations will be discussed, and more accurate expressions for equilibrium emittance presented.

Chapter 5

Developing a more accurate cooling formula

The standard expression for the rms scattering angle, used in the cooling formula, dates back to work by Rossi and Greisen in 1955, and derives from Rutherford's single scattering law. The expression differs from Monte Carlo predictions by up to 25%. Alternative expressions which incorporate atomic screening and the scattering effects of electrons are developed, which agree with the Monte Carlo to within 2% in LH_2.

The cooling formula (Equation 2.9) is an approximate expression used to predict the rate of change of the transverse emittance of a beam of particles, and was derived in Chapter 2. Charged particles, when traversing material, are deflected by many single, small-angle scatters, largely due to Coulomb interactions with nuclei, known as multiple Coulomb scattering (MCS). Large-scale Monte Carlo codes generate angular MCS distributions using multiple scattering theories, which are based on specific single-scattering cross-sections.

As discussed in Chapter 3, Monte Carlo cooling studies in Geant4 and ICOOL disagree with the cooling formula by up to 25% in low Z materials, which are, ironically, the most effective cooling media. The greatest source of this disagreement was found to lie in the multiple scattering term, illustrated in Figure 4.5 in Chapter 4. The term is only an approximation, derived from work by Rossi and Greisen in 1942 [34] which used Rutherford's original single-scattering cross-section.

A short introduction is presented to the single-scattering cross-sections of Rutherford and Wentzel followed by a derivation of the Rossi-Greisen approximation.

5.1 The Rutherford cross-section

The simplest, and most basic understanding of scattering dates back to the α-particle scattering experiments of Rutherford at the start of the 20th century [59]. In 1906 Rutherford observed the slight deflection of α-particles in matter, suggesting the existence of a positive charge in the atom. Three years later Rutherford instructed Geiger and Marsden to search for α-scattering at large angles using gold foil, although this was more of a laboratory exercise for Geiger who was an undergraduate student at the time - as far as Rutherford was concerned there was little prospect of observation! Geiger and Marsden did in fact find that a very small fraction of α-particles back-scattered, an event Rutherford later described as "quite the most incredible event that ever happened to me in my life". Geiger and Marsden's results could not be explained by the Thompson's "Plum Pudding Model" (1904) [60], which considered the atom as a uniform sphere of mass and positive charge, as it was unable to generate a strong enough electric field to deflect an α-particle through such a large angle. Despite Rutherford's support for the model, his only recourse was to conclude that the scattering field, and most of the atomic mass, must in fact be concentrated in a central nucleus, far smaller ($< 10^{-13}$ m) in fact that the radius of the atom (10^{-10} m). The Rutherford model supplanted the Plum Pudding Model, becoming Rutherford's most famous contribution to science, his 1908 Nobel Prize winning work in Chemistry notwithstanding! Rutherford also derived an expression using classical mechanics to explain Geiger and Marsden's measurements, known as the Rutherford differential cross-section (DCS), which is discussed in Section 13.6 of [61].

The Rutherford DCS describes the deflection of a singly charged particle into a solid angle $d\omega$ by the electric field of a nucleus [61],

$$\frac{d\sigma}{d\omega} = \left(\frac{Z\alpha}{2p\beta}\right)^2 \frac{1}{\sin^4(\frac{\theta}{2})} \approx \left(\frac{2Z\alpha}{p\beta}\right)^2 \frac{1}{\theta^4}, \tag{5.1}$$

in the small-angle approximation. The fine structure constant $\alpha = e^2/4\pi\epsilon_0 \approx 1/137$. Rutherford's result can also be derived in non-relativistic quantum mechanics using the Born approximation, and is presented in Section 5.2 of [62]. The small-angle approximation is appropriate since MCS distributions consist of a dominant, approximately Gaussian distribution at small angles, with an

asymptotic tail to large angles. The scattering potential of the nucleus is represented as a point charge Ze, where screening by atomic electrons is neglected and inelastic scattering off electrons is not considered. Other factors including target recoil, spin, relativity effects are neglected also, but these omissions are considered insignificant at moderate (MeV) energies and small angles [63].

5.2 The Wentzel cross-section

In 1927 Wentzel published a DCS which included the screening of the nuclear field by orbiting electrons, derived using quantum mechanics, [64]. Screening involves the shielding of the nuclear field by electrons which reduces the net (scattering) potential felt by an incident particle. The electric charge distribution of the scattering atom is modelled by a spherically symmetric potential, $V(r)$, with which the incident particle interacts and is then deflected. Figure 5.1 illustrates the difference between the Wentzel and Rutherford models.

Wentzel obtained his DCS using the first Born approximation* and an exponentially screened (Yukawa) potential:

$$V(r) = \frac{Z_1 Z_2 e^2}{r} e^{(-r/R)}, \tag{5.2}$$

where R is the atomic size (also called the screening radius), typically taken to be the Thomas-Fermi radius:

$$r_a = \frac{r_e}{Z^{1/3}\alpha^2}, \tag{5.3}$$

which derives from the Thomas-Fermi model of the atom†. r_e is the classical radius of the electron.

*The Born approximation can be used to obtain a simpler, approximate solution to the differential scattering cross-section [65]. It applies only to systems where the scattering potential $V(\mathbf{r})$ is weak, a special case in which the wave functions of the incoming and outgoing (scattering) particle can be described by the plane waves, $\propto e^{ikz}$, as shown in [66]. Implicit in the Born approximation are that the scattering potential is a function of radial distance r only, $V = V(r)$, and that scattering is well-described by the momentum transferred by the incident particle. Higher orders of the Born approximation exist, but are difficult to implement. The first and second Born approximations are compared with an analytical field by Salvat in [67].

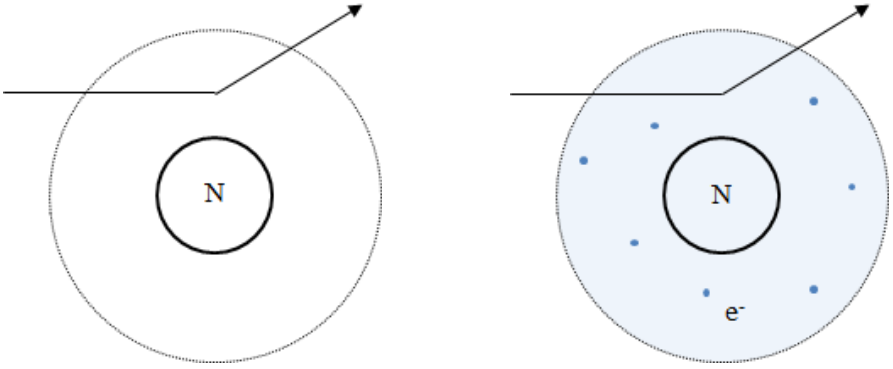

(a) (b)

Figure 5.1: (a) The classical Rutherford description of scattering and (b) the Wentzel treatment which includes the screening effects of atomic electrons. Both descriptions assume the electric field of the nucleus to be of a point charge Ze.

The Wentzel DCS can be written in the small-angle approximation as [64]:

$$\frac{d\sigma}{d\omega} = \left(\frac{2Z\alpha}{p\beta}\right)^2 \frac{1}{(\theta^2 + \theta_1^2)^2}. \tag{5.4}$$

The parameter θ_1 is known as the Born screening angle [63] and can be written as:

$$\theta_1^2 = \frac{1}{k^2 R^2} = \frac{\lambda\!\!\!^{-2}}{R^2}, \tag{5.5}$$

where k is the wave number of the incident particle and $1/k = \lambda\!\!\!^{-}$, the de Broglie wavelength of the particle. θ_1 can be derived using the Uncertainty Principle, $\Delta x \Delta p \lesssim \hbar/2$, where the uncertainty in momentum $\Delta p = p_\perp$, the transverse momentum transfer, and the uncertainty in position, Δx, corresponds to the impact parameter. If one assumes the nuclear field to be zero outside of the atom, the impact parameter for a collision must be no greater than the rms radius of the atom, R. Beyond this distance the particle feels no potential and will not scatter. The Uncertainty Principle can be used to give an expression for the scattering angle, θ, where $\Delta p = p_\perp = p\theta = \hbar/2\Delta x$. The minimum angle of scattering, θ_1, is then obtained by setting $\Delta x = R$, where the wave number k is equivalent to p by $k = p/\hbar$.

Figure 5.2 compares the behaviour of the two differential cross-sections at small angles in hydro-

[†]The Thomas-Fermi atomic model [68, 69] is an approximate description of the electron distribution about the atomic nucleus. It represents the electron cloud as a negatively charged, zero-temperature Fermi-Dirac fluid.

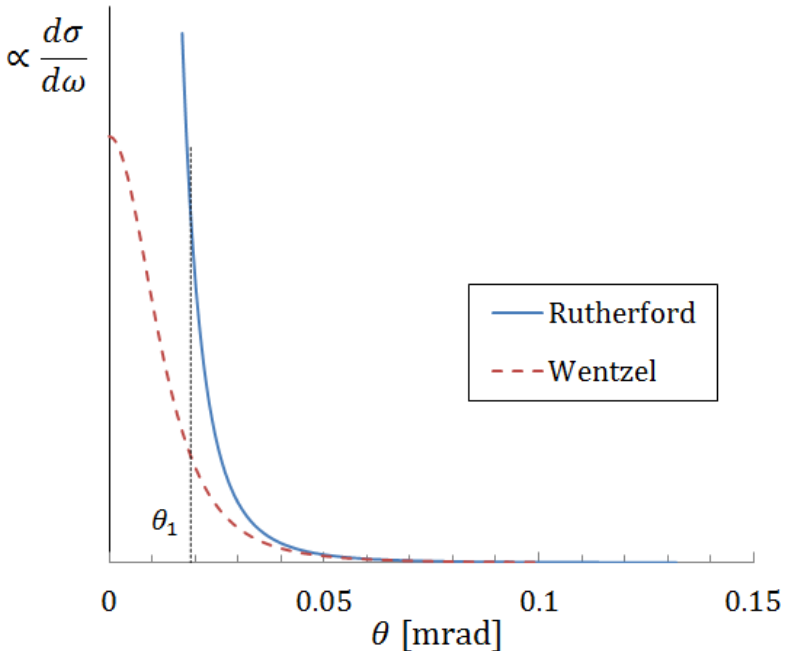

Figure 5.2: Comparison of the Rutherford and Wentzel differential cross-sections in hydrogen. The Rutherford form is considered unphysical at very small angles, so a cut-off is commonly applied. For 200 MeV/c muons in hydrogen this is approximately $\theta_1 = 0.019$ mrad.

gen. θ_1 acts as both a a small-angle cut-off to the Rutherford DCS, below which it is considered unphysical, and as the screening angle parameter in the Wentzel DCS, as shown in Equation 5.4. θ_1 is calculated using Equation 5.9, which is derived from the Thomas-Fermi model of the atom. For muons of $p = 200$ MeV/c in hydrogen $\theta_1^n = 0.019$ mrad. Wentzel's adjustment to Rutherford's DCS gives a finite, rather than infinite, value for the cross-section at $\theta = 0$, as shown in the figure.

5.3 Origins of the PDG scattering approximation

As discussed in the Chapter 3, the cooling formula and Monte Carlo disagree by up to 30% in low Z materials. The greatest source of disagreement resides in their treatments of MCS. The cooling formula uses an approximation for the rms scattering angle (Equation 2.2), known as the PDG formula, which originates from work by Rossi and Greisen [34]. A more detailed exposition is given in Rossi's book [56], written in 1952. Since the origins of the PDG formula are not well known, Rossi and Greisen's method is now presented, starting from Rutherford's original cross-section (Equation 5.1).

An expression for the probability of scattering, at an angle of θ to its original motion into a solid angle $d\omega$, can be derived using the Rutherford DCS:

$$\Xi(\theta)d\omega dz = \frac{d\sigma}{d\omega}\frac{N_A}{A}d\omega dz, \tag{5.6}$$

where N_A/A is the number of atoms in a thickness dz [g cm^{-2}][‡] of material, and $d\omega = 2\pi\theta d\theta$ in the small-angle approximation ($\sin\theta \approx \theta$). The expression evaluates to give:

$$\Xi(\theta)d\omega dz = 4N_A\frac{Z^2}{A}r_e^2\left(\frac{m_e c}{p\beta}\right)^2\frac{d\omega}{\theta^4}dz, \tag{5.7}$$

known as the Rutherford scattering formula. According to Rossi and Greisen [34], the scattering probability, Ξ, can be integrated to give the rate of change of mean square scattering angle,

$$\frac{d\langle\theta^2\rangle}{dz} = \int_{\theta_1}^{\theta_2}\theta^2\Xi(\theta)d\omega, \tag{5.8}$$

where the limits θ_1 and θ_2 define the range over which the Rutherford DCS is considered physical, related to the size of the atom and nucleus respectively. Setting $R = r_a$ in Equation 5.5, where r_a is the Thomas-Fermi radius defined in Equation 5.3, gives,

$$\theta_1 = \frac{\lambda\!\!\!^{-}}{r_a} = Z^{1/3}\alpha^2\frac{\lambda\!\!\!^{-}}{r_e} = \frac{Z^{1/3}}{137}\frac{m_e c}{p}, \tag{5.9}$$

which is also known as the Born screening angle, where r_e is the radius of the electron. The Uncertainty Principle can be invoked at large θ (Δp_{max}) also, where the smallest possible impact parameter is the radius of the nucleus. Smaller impact parameters are possible however, where particles penetrate the structure of the nucleus, scattering off the constituent protons and neutrons. This is known as inelastic nuclear scattering, to very large angles ($\theta > \theta_2$). This cross-section is very small however, so the contribution to the scattering distribution above θ_2 is negligible.

Rossi [56] defines the upper angular limit as:

[‡]For consistency dz is used throughout this thesis, although Rossi and Greisen use dx.

$$\theta_2 = \frac{\lambda\!\!\!^{-}}{0.49 r_e A^{1/3}} = 280 A^{-1/3} \frac{m_e c}{p}, \tag{5.10}$$

based upon an approximate nuclear radius $r_n = 0.49 r_e A^{1/3}$. For muons of $p = 200\,\mathrm{MeV}/c$ in LH_2 $\theta_1 = 0.019\,\mathrm{mrad}$ and $\theta_2 = 714\,\mathrm{mrad}$, and in carbon $\theta_1 = 0.034\,\mathrm{mrad}$ and $\theta_2 = 312\,\mathrm{mrad}$. Table 7.2 gives $\theta_{1,2}$ values for $p = 172\,\mathrm{MeV}/c$ muons (as used in the MuScat Experiment [28], discussed in Chapter 7) in low Z materials from LH_2 to Fe.

Evaluation of the integral in Equation 5.8 using the limits $\theta_{1,2}$ gives:

$$\begin{aligned} \frac{d\langle\theta^2\rangle}{dz} &= 8\pi N_A \frac{Z^2}{A} r_e^2 \left(\frac{m_e c}{p\beta}\right)^2 \ln\left(\frac{\theta_2}{\theta_1}\right) \\ &= 16\pi N_A \frac{Z^2}{A} r_e^2 \left(\frac{m_e c}{p\beta}\right)^2 \ln\left[196 Z^{-1/3} \left(\frac{Z}{A}\right)^{\frac{1}{6}}\right]. \end{aligned} \tag{5.11}$$

Rossi suggests using 1 as an upper limit of integration when $\theta_2 > 1$, which gives a slightly different result, given as Equation 2.16.5 in [56]. Rossi and Greisen's key observation was to recognise that the log dependency in the above equation is very similar to the log term in the definition of radiation length:

$$\frac{1}{X_0} = 4\alpha \frac{N_A}{A} Z^2 r_e^2 \ln(183 Z^{-1/3}), \tag{5.12}$$

given in [34] and on p54 of [56]. They then substitute the definition for X_0 into Equation 5.11, cancelling the log terms to obtain a new expression:

$$\begin{aligned} \frac{d\langle\theta^2\rangle}{dz} &= \frac{1}{X_0} \frac{4\pi}{\alpha} \left(\frac{m_e c}{p\beta}\right)^2 \\ &= \frac{E_s^2}{p^2\beta^2} \frac{1}{X_0}, \end{aligned} \tag{5.13}$$

where $E_s = 21.2\,\mathrm{MeV}$, originally. The log terms in Equations 5.11 and 5.12 are equal at $Z = 1$, and differ only slightly at large Z (2.3% for $Z = 82$ (lead)), so this substitution was in fact very accurate.

Integrating Equation 5.11 over a material thickness Δz gives the rms scattering angle in two dimensions:

$$\theta_0 = \frac{1}{\sqrt{2}} \frac{E_s \,\mathrm{MeV}}{p\beta} \sqrt{\frac{\Delta z}{X_0}} = \frac{E_{s,x} \,\mathrm{MeV}}{p\beta} \sqrt{\frac{\Delta z}{X_0}},$$

where $E_{s,x} = E_s/\sqrt{(2)} = 14.85\,\mathrm{MeV}$. The expression allows experimentalists to make quick, straightforward predictions since X_0 values are readily available. This spares the experimentalist from getting embroiled in having to obtain an rms width from distributions generated using a theory of MCS, which can be difficult and time-consuming. In spite of these advantages Rossi and Greisen's approximations were shown by Highland [57] in 1975 to be somewhat crude at low Z.

Highland evaluated $d\langle\theta^2\rangle/dz$ using Molière's theory of multiple scattering[§] [70] for different Z targets, with thickness $\Delta z = 0.1X_0$, and then computed E_s by rearranging Equation 5.13, which is supposed to be a constant term. The E_s term was however far from constant, especially at low Z, as illustrated in Figure 5.3 which shows Highland's original plot of E_s (Z) [57]. Highland adjusted the value of E_s from 21.2 to 17.5 MeV, but made no attempt to account for the clear Z dependency at low Z. Highland also found a strong path length dependency, illustrated by Lynch and Dahl in their review [71], for which he attempted to correct by adding a natural log term, $\ln(\Delta z/X_0)$. Lynch and Dahl also made their own revision, adjusting the E_s term to 19.23 MeV, corresponding to $E_{s,x} = 13.6\,\mathrm{MeV}$. The Particle Data Group review quotes Highland's formula with this adjustment, giving the 2D rms angle as:

$$\theta_0 = \frac{13.6\,\mathrm{MeV}}{p\beta} \sqrt{\frac{\Delta z}{X_0}} \left[1 + 0.038 \ln(\Delta z/X_0)\right],$$

which was quoted previously as Equation 4.2. The cooling formula uses this expression, minus Highland's log term, and contains no explicit dependence on Z.

[§] An introduction to multiple scattering theories is given in Chapter 6.

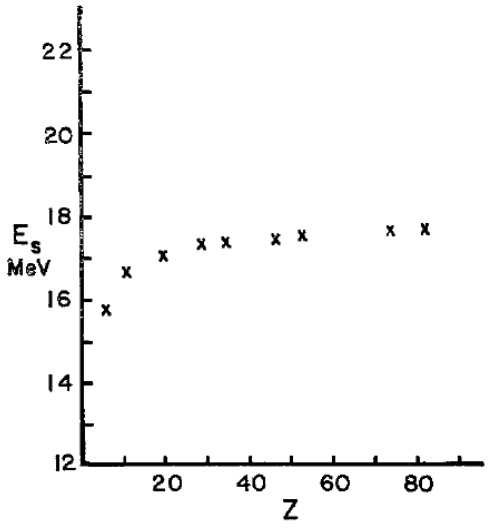

Figure 5.3: Highland's [57] plot of E_s as a function of atomic number, Z, computed from Molière Theory for absorbers of thickness $\Delta z = 0.1 X_0$ and momenta $\beta = 1$.

5.4 Inclusion of atomic electrons

5.4.1 Scattering

The Rutherford scattering formula (Equation 5.11) does not include scattering off constituent electrons, only nuclei, as implied by the Z^2 dependence. Rossi [56] suggests rectifying this by replacing the Z^2 term with $Z(Z + 1)$, as recommended by several authors including Bethe [70]. Considering Rossi and Greisen's approximation contains no Z dependence, however, it is fortunate that the same logic can be applied to definition of radiation length (Equation 5.12), rewritten as:

$$\frac{1}{X_0} = 4\alpha \frac{N_A}{A} Z(Z+1) r_e^2 \ln(183 Z^{-1/3}),$$

to include electron scattering, as recommended by Rossi [56]. In fact the quoted (modern) X_0 values in the PDG Review [32], which are calculated according to Tsai [33], are very similar to the values calculated using Rossi's modified formula, as shown in Figure 5.4. As a result, use of the Rossi-Greisen expression with the PDG values effectively includes electrons. It is important to note that the expression still makes no allowance for the Z dependence in the E_s term, as shown by Highland in Figure 5.3.

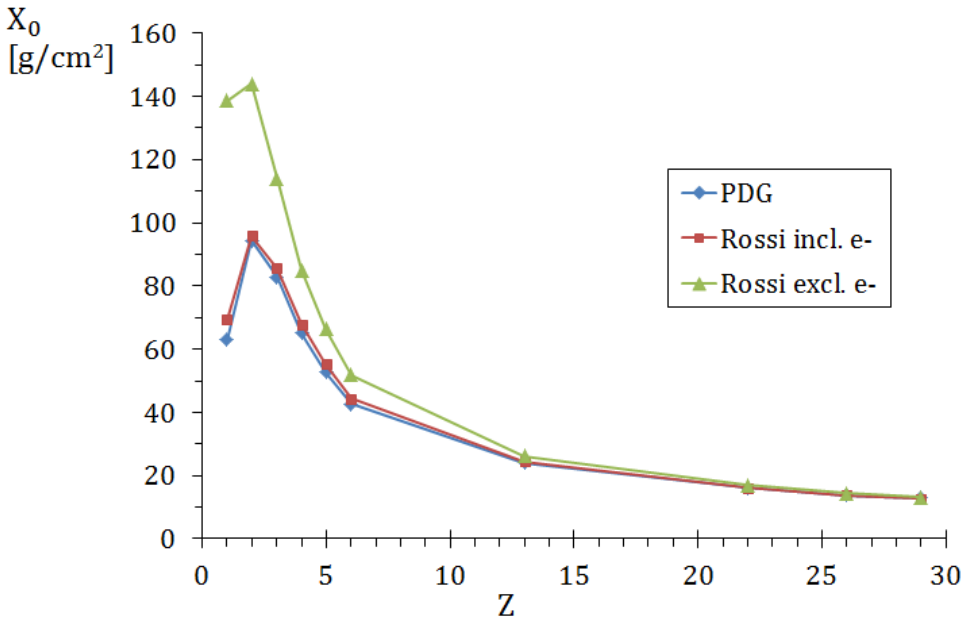

Figure 5.4: Comparison between the PDG value for radiation length, X_0, and the (now obsolete) formulae used by Rossi in his 1955 book [56].

It is possible, however, to develop a more nuanced approach by expanding the redefined Rutherford formula, using $Z(Z+1)$, into separate nuclear and electronic components, with distinct limits of integration, $\theta_{1,2}$ and $\theta^e_{1,2}$ respectively. As before one must assume the same $d\sigma/d\omega$ for scatters with electrons. Equation 5.8 can now be expanded to reflect atomic scattering, giving:

$$\frac{d\langle\theta^2\rangle}{dz} = Z^2 \int_{\theta_1}^{\theta_2} \theta^2 \Xi'(\theta) d\omega + Z \int_{\theta_1^e}^{\theta_2^e} \theta^2 \Xi'(\theta) d\omega. \tag{5.14}$$

where Ξ' is simply Equation 5.7 (using $Z(Z+1)$) with the Z terms removed, and placed outside the integral. $d\langle\theta^2\rangle/dz$ clearly scales with Z^2 for nuclear scatters and Z for electrons.

Scattering from electrons is somewhat different to nuclear scattering, since electrons are not screened and are much less massive than even small nuclei. As a result, the θ^e_1 parameter is just a low-angle cut-off to the cross-section and is not a screening parameter as such. The angle corresponds, approximately, to the smallest angle of scattering at which the electrons can be considered to be free, i.e. the θ for an energy transfer equal to the binding energy of the particular shell.

Approximate values for θ_1^e can be obtained using:

$$\cos\theta = \frac{p^2 - (E + m_e)\nu}{|p||p'|},$$

(Equation 4.1) by setting the energy transfer, ν, equal to the binding energy of the scattering atom, which are as follows: H (13.6 eV), Li (55 eV), Be (112 eV), C (284 eV), Al (1.56 keV) and Fe (7.1 keV), taken from [72]. The K-shell values are used for the heavier elements. The corresponding values for θ_1^e [mrad] are (H) 0.019, (Li) 0.038, (Be) 0.054, (C) 0.083, (Al) 0.200 and (Fe) 0.426. For 200 MeV/c muons the nuclear cut-off angle $\theta_1^n = \theta_1^e$ in hydrogen, where θ_1^n is calculated using Equation 5.9. At higher Z however θ_1^n increases slower ($\propto Z^{1/3}$) than θ_1^e, and the values diverge, which is discussed in Section 7.3. Scatters from electrons becomes unimportant as Z increases, as the nuclear charge rapidly dwarfs the potential of the orbiting electrons.

It is reasonable, therefore, to assume $\theta_1^e \approx \theta_1^n$ for all Z, and use a single angle, θ_1, as the lower limit for both integrals. A multiple scattering distribution for a single muon will contain very many (thousands) of collisions, so the precise value of both θ_1^e and θ_1 is unlikely to make any discernible difference to the distribution. Figure 4.2 shows the angle of scattering as a function of the energy transfer, for a 200 MeV/c muon scattering off an electron, a proton and a Be nucleus. The binding energies of H and Al (K-shell) are included in the figure, below which scattering is considered unimportant. For a 200 MeV/c muon ($\beta = 0.88$) the maximum energy transfer is 3.59 MeV, as illustrated in the figure.

The maximum angle of scattering, for a muon off a constituent electron, θ_2^e, corresponds to a 90° deflection in the centre of mass frame. This angle is approximately 4.84 mrad (for $\nu = 1.76$ and 1.93 MeV) above which momentum conservation fails. This value agrees with Scott's definition:

$$\theta_2^e \approx \frac{m_e}{m_\mu}, \tag{5.15}$$

which is given as Equation 6.71 in [63]. Above θ_2^e only nuclear collisions contribute to the cross-section since θ_2^n is much larger (830 mrad in H, 436 mrad in Li). As a result the scattering distribu-

tion tends to the Rutherford result (θ^{-4}) at large angles, where the Gaussian region of the scattering distribution (at small-angles) includes θ_2^e.

The integral given in Equation 5.14 can now be evaluated using these limits to give the rate of change of mean square scattering angle for scattering off an atom:

$$\frac{d\langle\theta^2\rangle}{dz} = 8\pi N_A \frac{Z^2}{A} r_e^2 \left(\frac{m_e c}{\beta p}\right)^2 \left[\ln\left(\frac{\theta_2}{\theta_1}\right) + \frac{1}{Z}\ln\left(\frac{\theta_2^e}{\theta_1^e}\right)\right], \tag{5.16}$$

where the electron scattering contribution is given by omitting the first (nuclear) term in the brace.

For easy comparison, Figure 5.5 shows $X_0 d\langle\theta^2\rangle/dz$ for elements from hydrogen to iron, illustrating the Z dependence. Values for all formulae are given in Table 5.1. Angles are calculated for the total atomic cross-section (Equation 5.16) and the separate nuclear and electron components. Predictions are given according to three approximations: the Rossi-Greisen form (Equation 5.13), the original Rutherford formula (Equation 5.11, which uses $Z(Z+1)$), and the PDG formula without the natural log term (Equation 2.2) as used in the standard cooling formula. The new atomic Rutherford formula predicts a clear Z dependence, in contrast to the original Rutherford formula and PDG/Rossi-Greisen approximations which are very similar since the latter is simply an approximation of the former. The electron component is most significant at $Z = 1$ (30% of the total angle) and drops off significantly with Z, as expected.

5.4.2 Screening of the nucleus

As noted earlier, electrons also screen the nuclear charge from incident particles, reducing the net field and therefore the amount of scattering. Whilst screening is absent from Rutherford's classically derived formula, the Wentzel DCS (Equation 5.4) includes screening, as described earlier in Section 5.2. Substituting the Wentzel DCS into Equation 5.6 gives the Wentzel scattering probability:

$$\Xi(\theta) d\omega dz = 4N_A \frac{Z^2}{A} r_e^2 \left(\frac{m_e c}{\beta p}\right)^2 \frac{d\omega}{(\theta_1^2 + \theta^2)^2} dz. \tag{5.17}$$

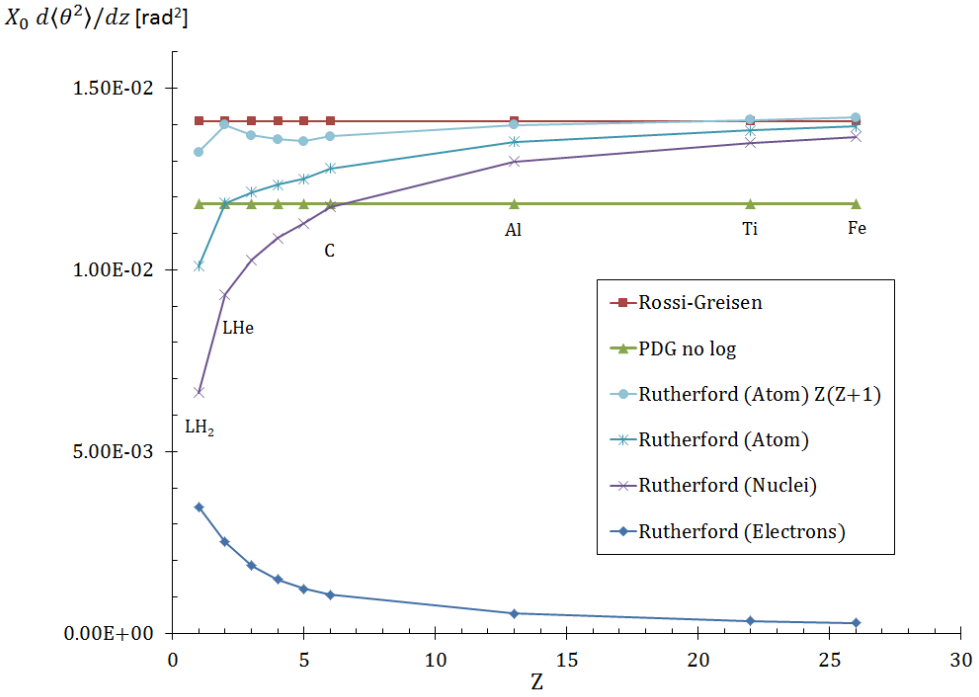

Figure 5.5: Mean square angle of scattering per X_0, for $p = 200\,\mathrm{MeV}/c$ muons, predicted using the new, modified Rutherford formula.

The expression is analogous to the Rutherford form given in Equation 5.7 and θ_1 is the screening angle (Equation 5.9) [56]. Whilst the formula is attributed by Rossi to Goudsmit and Saunderson [73, 74], it derives from the differential cross-section by Wentzel [64] (Equation 5.4). The formula can be inserted inside the integral in Equation 5.8 and evaluated to give the rate of change of mean square scattering angle:

$$\frac{d\langle\theta^2\rangle}{dz} = 4\pi N_A \frac{Z^2}{A} r_e^2 \left(\frac{m_e c}{\beta p}\right)^2 \left\{\ln\left[\left(\frac{\theta_2}{\theta_1}\right)^2 + 1\right] - 1\right\}. \tag{5.18}$$

Following the same procedure explained in the previous section one can obtain an atomic expression using the integral given in Equation 5.14, where Ξ' is now defined to be the Wentzel formula given in Equation 5.17. Once again it is assumed that nuclear and electron scatters have the same cross-section ($d\sigma/d\omega$) and the angular limits $\theta_{1,2}$ and θ_2^e remain unchanged. The resultant atomic form of the Wentzel scattering formula is as follows:

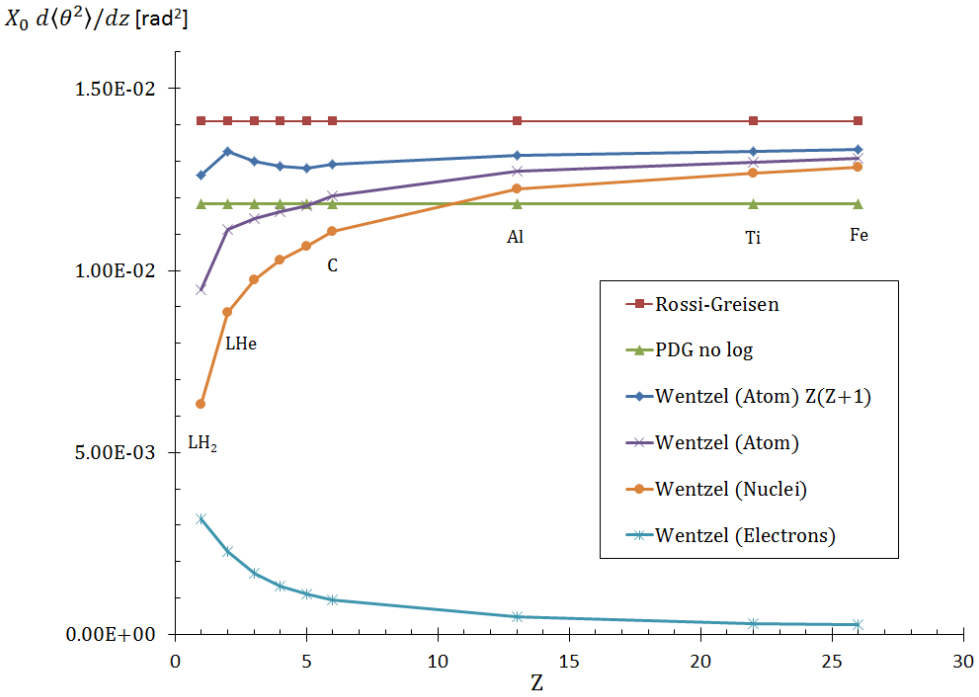

Figure 5.6: Mean square angle of scattering per X_0, for $p = 200\,\text{MeV}/c$ muons, calculated using the new, modified Wentzel formula.

$$\frac{d\langle\theta^2\rangle}{dz} = 4\pi N_A \frac{Z^2}{A} r_e^2 \left(\frac{m_e c}{\beta p}\right)^2 \left\{\ln\left[\left(\frac{\theta_2}{\theta_1}\right)^2 + 1\right] - 1 + \frac{1}{Z}\left(\ln\left[\left(\frac{\theta_2^e}{\theta_1^e}\right)^2 + 1\right] - 1\right)\right\}, \tag{5.19}$$

in which the nuclear and electron components once again scale with Z^2 and Z respectively.

Figure 5.6 shows $X_0\, d\langle\theta^2\rangle/dz$ versus Z for the Wentzel DCS-based formulae, analogous to the Rutherford plots in Figure 5.5. The new atomic description (Equation 5.19) gives a clear dependence on Z, otherwise absent from the Rossi-Greisen, PDG and original Wentzel formulae. In LH_2 the mean square angle was 9.5×10^{-3} rad^2 per X_0 using the new formula, 25% less than the Rossi-Greisen line. Values are listed in Table 5.1. The predictions from the new Rutherford and Wentzel expressions will now be compared with ELMS and the Lynch and Dahl formula.

		LH_2	LHe	Li	Be	B	C	Al	Fe
		$(Z=)1$	2	3	4	5	6	13	26
Rutherford	nuclei	.0066	.0093	.0103	.0109	.0113	.0117	.0130	.0137
	electrons	.0035	.0025	.0019	.0015	.0012	.0011	.0005	.0003
	atom	.0101	.0118	.0121	.0123	.0125	.0128	.0135	.0140
	$Z(Z+1)$	.0132	.0140	.0137	.0136	.0135	.0137	.0140	.0142
Rossi-Greisen		.0141	.0141	.0141	.0141	.0141	.0141	.0141	.0141
PDG (no log term)		.0118	.0118	.0118	.0118	.0118	.0118	.0118	.0118
Lynch and Dahl		.0104	.0115	.0115	.0115	.0115	.0117	.0123	.0128
ELMS		.0082							
Wentzel	nuclei	.0063	.0089	.0097	.0103	.0107	.0111	.0122	.0128
	electrons	.0032	.0023	.0017	.0013	.0011	.0010	.0005	.0003
	atom	.0095	.0111	.0114	.0116	.0118	.0120	.0127	.0131
	$Z(Z+1)$	.0126	.0133	.0130	.0129	.0128	.0129	.0132	.0133

Table 5.1: Predictions for the mean square scattering angle per radiation length, $X_0 d\langle\theta^2\rangle/dz$ [rad^2 per X_0].

5.5 Comparison

Lynch and Dahl comment in their review paper [71] that radiation length is in fact a poor measure of scattering, and present their own expression:

$$\frac{d\langle\theta^2\rangle}{dz} = \frac{\theta_c^2}{1+F^2}\left[\frac{1+\nu}{\nu}\ln(1+\nu) - 1\right],$$

which is independent of X_0 and was motivated by angular distributions from a screened Rutherford cross-section. The parameter $\nu = 0.5\Omega/(1-F)$, where Ω represents the mean number of scatters, $\Omega = \theta_c^2/\theta_a^2$. θ_c^2 is known as the characteristic angle and θ_a^2 the screening angle, defined according to Molière Theory (Equations 6.1 and 6.2). Note that θ is used in place of Lynch and Dahl's notation (χ) for consistency. F denotes the central fraction of tracks used in the scattering distribution. Lynch and Dahl state that for F in the range $90\% - 99.5\%$ the form represents Molière Theory to better than 2%, for $10^{-3} \leq \Omega < 10^8$ and $\Delta z/X_0$ between 10^{-3} and 100, for all Z. Whilst Lynch and Dahl comment that it is "much better" than the Rossi-Greisen and PDG (Highland) expression they do not present the comparison in their paper. In addition, no derivation is provided, so the underlying physics behind the expression is unclear.

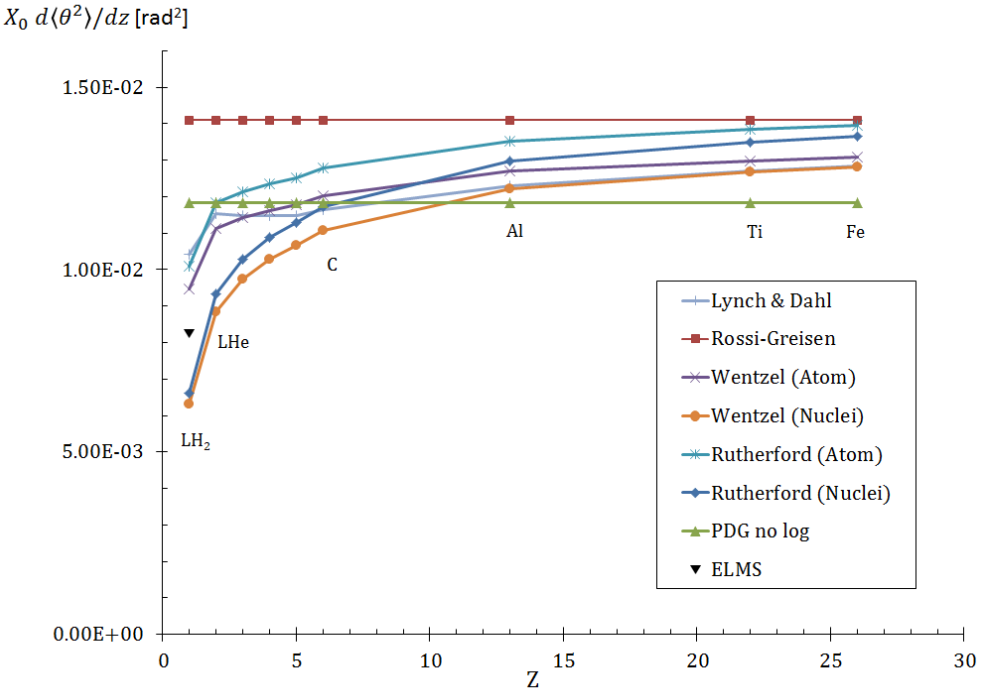

Figure 5.7: Mean square scattering angle per X_0, for $p = 200\,\text{MeV}/c$ muons, comparison between expressions.

Figure 5.7 presents the mean square angle per X_0 calculated from the original scattering formulae of Rutherford and Wentzel, alongside the new formulae already described. The ELMS value in LH_2 is included also, computed using the rms projected momentum transfer ($1.361\,\text{MeV}/c$) taken from Table 3.5 on page 63 of Holmes' thesis [50]. The Rossi-Greisen and PDG (no log term) lines ($E_s = 21, 16\,\text{MeV}$) are plotted, and also the Lynch and Dahl prediction (Equation 5.13). Values are given in Table 5.1. The angle predicted by the Wentzel formula for the total cross-section is approximately 6% less than the Rutherford value for all Z. This was anticipated since screening reduces the scattering potential seen by the incident particle, absent from the Rutherford description. The Rutherford and Wentzel formulae predict less scattering at low Z, most significantly in hydrogen. The ELMS value was $\sim 20\%$ below those of the Rutherford and Wentzel atomic expressions however. The Lynch and Dahl prediction was less than the cooling formula value for $Z \leq 6$ but was significantly larger than the ELMS value in LH_2.

5.6 Equilibrium emittance predictions

In Chapter 2 the following general form for the equilibrium emittance was derived (Equation 2.8):

$$\varepsilon_0 = \frac{p^2\beta\beta_\perp}{2m}\frac{d\sigma_{x'}^2}{dz}\left\langle\frac{dE}{dz}\right\rangle^{-1},$$

where $d\sigma_{x'}^2/dz \equiv d\langle\theta_0^2\rangle/dz$. This general expression may now be evaluated using the new expressions for $d\langle\theta_0^2\rangle/dz$, both of which do not incorporate the radiation length of the material. Table 5.2 lists ε_0 values for seven targets at three central momenta for the four formulae. Values for the Maus Monte Carlo are given in Table 3.4. The rms scattering angles for the compounds LiH and C_2H_4 (polyethylene) were calculated by a weighted sum:

$$\frac{d\langle\theta_0^2\rangle}{dz} = \frac{1}{M_w}\sum_{i=1}^{n} N_i A_i \frac{d\langle\theta_i^2\rangle}{dz},$$

where the angle for each element, $d\langle\theta_i^2\rangle/dz$, is weighted according to the ratio of its mass number, A_i, to the molecular weight, M_w. Figure 5.8 shows ε_0 for central p_z of 140, 200 and 240 MeV/c respectively, which are the standard MICE operating momenta. The Wentzel atomic expression clearly gives a lower value than the cooling formula in LH_2, which agrees with the Monte Carlo results. At $p_z = 200$ MeV/c for example, $\varepsilon_0 = 1.14$ mm (Maus) and 1.15 mm (Wentzel expression) compared with the cooling formula value of 1.43 mm. As Z increases, however, the Monte Carlo values tend to the cooling formula result, diverging from the Wentzel expression. The Rutherford values are greater than Wentzel in all cases, which is expected since Wentzel incorporates screening which will reduce the effective scattering field producing less multiple scattering.

Figure 5.9 shows the ratio $\varepsilon_0/\varepsilon_{CF}$, where ε_{CF} represents the value predicted by the cooling formula. The greatest disagreement is in LH_2 where predictions in Maus and the $d\langle\theta_0^2\rangle/dz$ expressions (based on the Rutherford and Wentzel cross-sections) are up to 20% less than the cooling formula value. The source of this disagreement has been shown to lie in the MCS term of the CF as it doesn't treat electron scatters properly, which are important at $Z = 1$ (LH_2). Use of the Wentzel DCS, which includes screening, along with specific angular limits (θ_2^e) gives much better agreement with

Material	Central p_z [MeV/c]	Standard Cooling Formula	Rossi-Greisen	Rutherford (atom)	Wentzel (atom)
LH_2	140	1.37	1.63	1.14	1.07
	200	1.43	1.71	1.22	1.15
	240	1.48	1.76	1.28	1.20
LHe	140	1.88	2.24	1.86	1.74
	200	2.02	2.41	2.02	1.90
	240	2.08	2.48	2.10	1.97
LiH	140	2.19	2.61	2.40	2.03
	200	2.38	2.83	2.60	2.23
	240	2.46	2.94	2.69	2.33
Li	140	2.48	2.96	2.52	2.37
	200	2.67	3.19	2.74	2.58
	240	2.76	3.30	2.85	2.68
Be	140	3.23	3.85	3.35	3.15
	200	3.48	4.15	3.64	3.42
	240	3.60	4.30	3.78	3.56
C_2H_4	140	3.58	4.27	3.77	3.54
	200	3.87	4.62	4.10	3.86
	240	4.01	4.78	4.26	4.01
C	140	4.50	5.37	4.84	4.55
	200	4.87	5.80	5.26	4.95
	240	5.04	6.00	5.46	5.14

Table 5.2: Equilibrium emittance predictions, ε_0 [mm], for $\beta_\perp = 42$ cm.

Monte Carlo in LH_2, but less so as Z increases which was not understood. The ε_0 predictions in Table 3.4 can be compared with experimental measurements in Step IV.

The discussion of scattering so far has only considered the equilibrium emittance and the rms angle of scattering, both of which are single numbers describing complex processes. The next chapter discusses how the actual distributions of scattering angles are obtained, through multiple scattering theories, such as Molière theory.

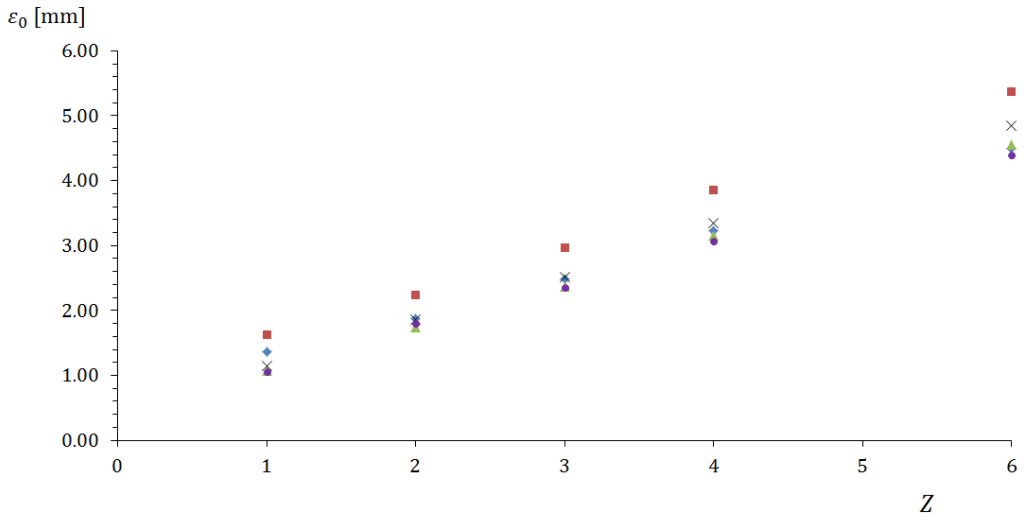

(a) $p_z = 140\,\mathrm{MeV}/c$.

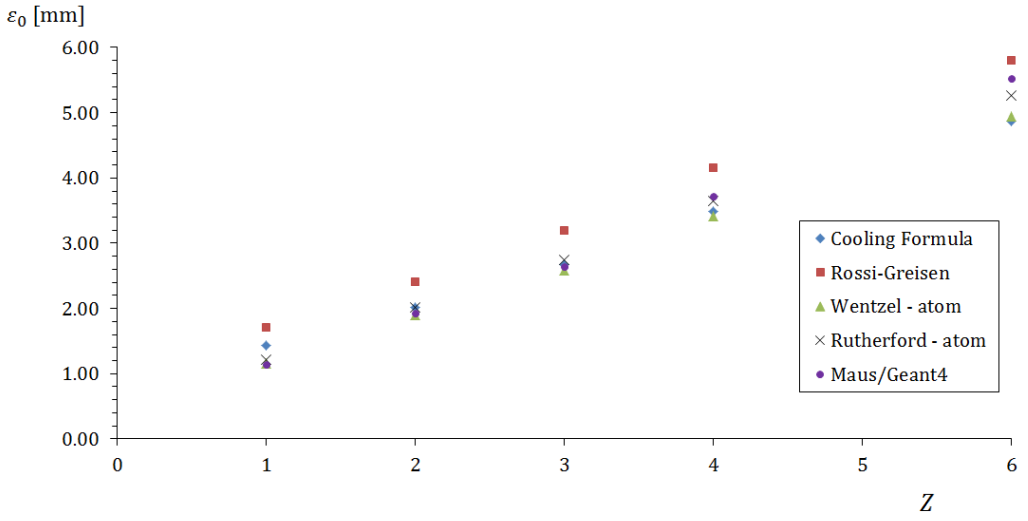

(b) $p_z = 200\,\mathrm{MeV}/c$.

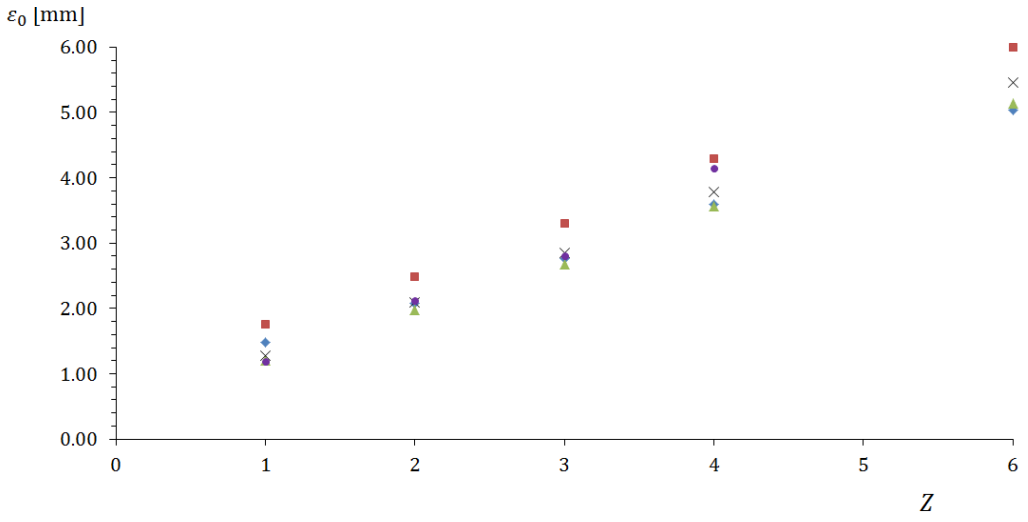

(c) $p_z = 240\,\mathrm{MeV}/c$.

Figure 5.8: Equilibrium emittance, ε_0, predicted by formulae and obtained in Maus.

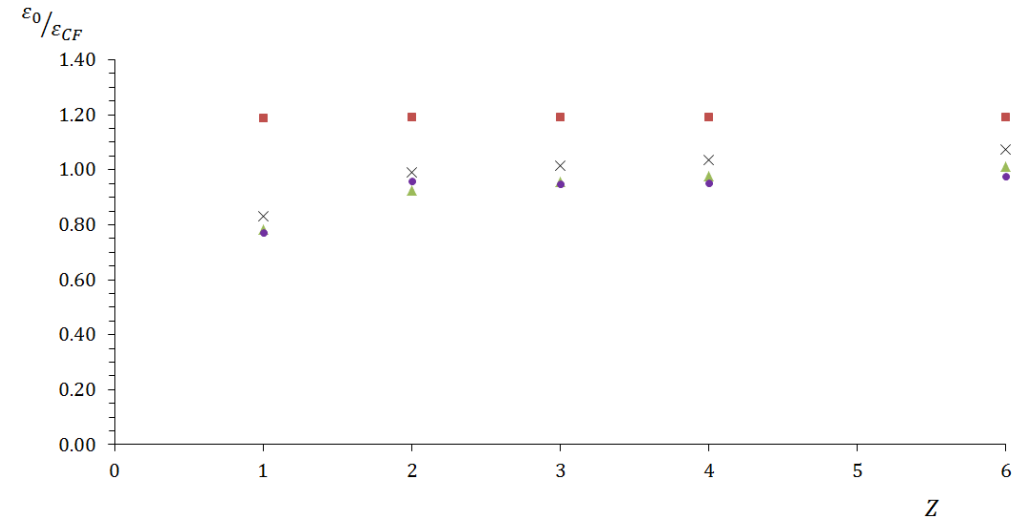

(a) $p_z = 140\,\mathrm{MeV}/c$.

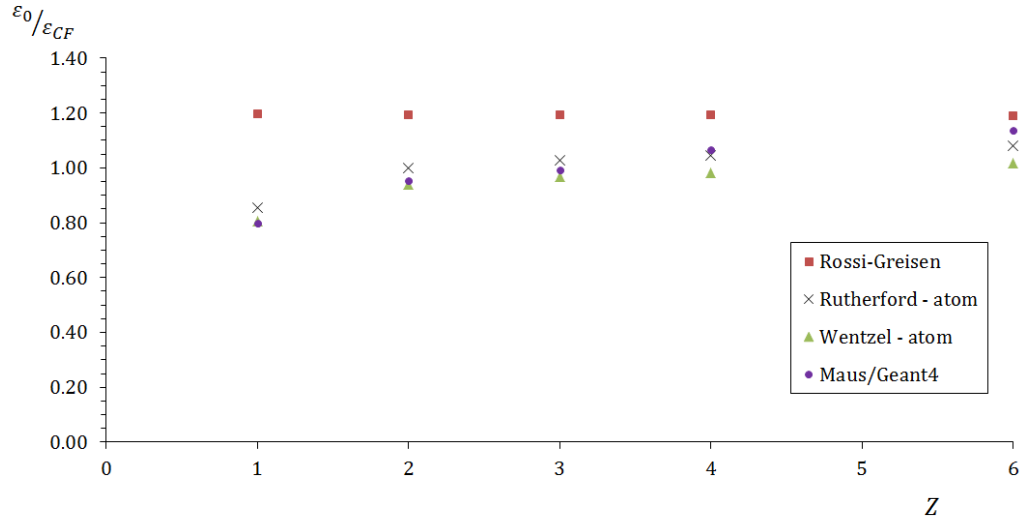

(b) $p_z = 200\,\mathrm{MeV}/c$.

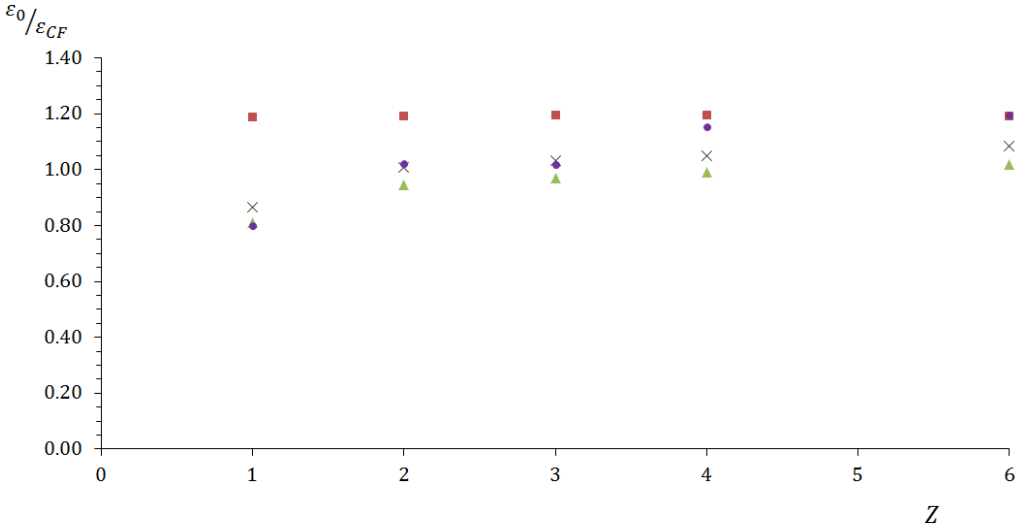

(c) $p_z = 240\mathrm{MeV}/c$.

Figure 5.9: Ratio of ε_0 to the cooling formula predictions, ε_{CF}.

Chapter 6

The Distribution of Scattering Angles

Multiple scattering theories, such as Molière's theory, predict the distribution of angles after a finite thickness of material. Distributions are derived by solving the transport equation in conjunction with a differential cross-section. An introduction to Molière theory, the most commonly used treatment, is presented.

The discussion of multiple Coulomb scattering (MCS) so far has only considered the rms width of scattering distributions, θ_0. As shown in Chapter 4, Monte Carlo values for θ_0 disagreed with the predictions of the PDG expression by up to 30%. In Chapter 5, a new expression for $d\langle\theta^2\rangle/dz$ was derived from the Wentzel single-scattering differential cross-section (DCS) (Equation 5.17), which includes the screening of the nucleus by atomic electrons and improved the agreement with Monte Carlo in LH_2.

The distribution of scattering angles after a thin slice of material is generated from a given DCS using a theory of multiple scattering. Prior to the development of high-speed computing (*i.e.* Monte Carlo) it would be left to the physicist to carry out the necessary convolution to then scale the distribution to the desired thickness of material. As discussed in Section 4.2, most Monte Carlo codes use condensed models that sample distributions (given by MCS theories) according to the chosen step length, instead of simulating all collisions, which can be very time-consuming. ELMS [49] and the XYZ model (described in Chapter 7) are the exception however, as they are atomistic (detailed) treatments, simulating all collisions, and do not use a theory of MCS, instead generating distributions using the differential cross-section.

It is important to emphasize that there is no reason to assume the Monte Carlo results are necessarily correct, as instabilities such as step length dependencies are not uncommon, as reported

in Section 4.2, and also in Section 3.8.3 of [50] (in Geant4.5.2p02). As a result experimental measurements are crucial to validate the scattering models in Monte Carlo.

This chapter introduces the multiple scattering theories of Molière and others, and presents a literature review of various scattering experiments. The most significant muon scattering experiment is the MuScat Experiment (2003) [28], which measured scattering distributions of 172 MeV/c muons in low Z targets, and is described in Section 7.2.

6.1 Introduction

Multiple scattering theories attempt to derive an analytic expression for the angular distribution, $f(\theta, t)$, of particles after a passing through a thickness t [g cm^{-2}] of material. These distributions are obtained by solving the transport equation [70], which considers successive scatters:

$$\frac{\partial f(\theta,t)}{\partial t} = -Nf(\theta,t)\int \sigma(\chi)\chi d\chi + N\int f(\vec{\theta'},t)\sigma(\chi)d\vec{\chi},$$

where θ is the angle of scattering after an initial thickness dt and χ the angle after a further dt. The first term on the right-hand side represents the probability of scattering out of, and the second the probability of scattering into, an annulus $d\theta$ after a thickness dt, as illustrated in Figure 6.1. N is the number of scattering atoms per cm^3, $\sigma(\chi)$ is the differential cross-section for single-scattering by an angle χ and $d\vec{\chi} = \chi d\chi d\phi/2\pi$. The azimuthal angle is represented by ϕ. The vector $\vec{\theta}$ is a 2D representation of the scattering angle, expressed in the plane perpendicular to the z-axis. The fraction in $d\theta$ after a further step dt equals the fraction that scatters into $d\theta$ ($\vec{\theta'} = \vec{\theta} - \vec{\chi}$), minus the flux that scatters out ($\vec{\theta}$). Solutions to this transport equation involve some form of transform (Bessel, Fourier) plus some numerical calculations and approximations.

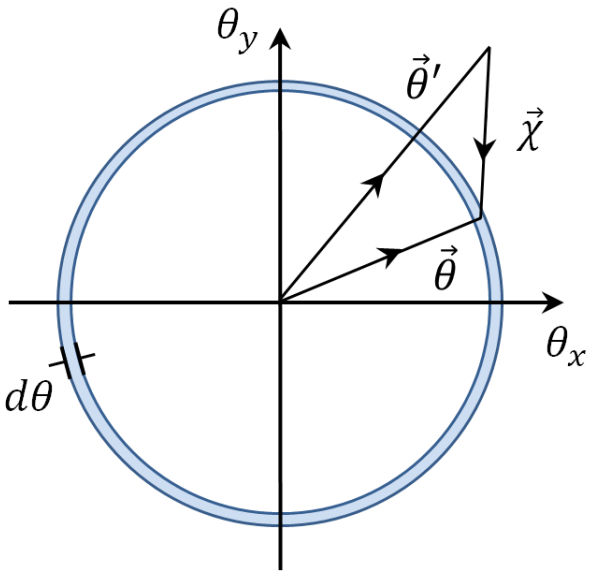

(a)

Figure 6.1: After scattering in a thickness t a muon will be moving with projected angles $\theta_x = p_x/p_z$ and $\theta_y = p_y/p_z$ such that $(\theta_x^2 + \theta_y^2) = \theta^2$. Its position in "angle space" (equivalently (p_x, p_y) space) is therefore specified by the vector $\vec{\theta} = (\theta_x, \theta_y)$. For a muon at $\vec{\theta}'$ to scatter into $d\theta$ at θ, in a subsequent element of thickness dt, the vector scattering angle $\vec{\chi}$ must satisfy $\vec{\theta}' + \vec{\chi} = \theta$.

One of the earliest multiple scattering theories was by Williams in 1939/40 [75, 76], who assumed a Gaussian distribution at small angles with a single-scattering tail to large-angles. This approach was however only "moderately successful" [63], and was soon superseded by a number of closely related MCS theories, notably those of Goudsmit and Saunderson [73, 74] (1940), Molière [77, 78] (1948, in German), which was expanded and clarified by Bethe in 1953 [70] and Lewis [52] (1950). The theory of Goudsmit-Saunderson is a complete description, giving the exact angular distribution for all angles, using Legendre polynomial expansion. Lewis theory uses a different method but obtains the same angular distribution function as Goudsmit and Saunderson, and computes the first moments of the spatial distribution also. Lewis theory forms the basis of the Urban scattering models in Geant4 [44]. Both Molière and Goudsmit and Saunderson show that the angular distribution, $f(\theta)$, is insensitive to the precise form of the cross-section, assuming it approaches the Rutherford cross-section at large angles. Section 1 of Scott's 1963 review paper provides a useful introduction to the topic [63]. Fernàndez-Varea et al. also present an excellent discussion of both MCS theory and simulation in their 1992 paper [54].

6.2 Molière theory

Molière's theory of multiple scattering [78] is the most widely-used theory of multiple scattering and uses the small-angle approximation. It exists in several forms after revisions by Bethe [70] (who presents a simpler derivation of Molière's method) and Fano [79], which will both be discussed later. Whilst other theories are more comprehensive (those of Goudsmit and Saunderson and Lewis for example) their results can often be obtained through Molière theory (which is simpler) with certain approximations. Bethe shows that Molière theory can obtain the Goudsmit and Saunderson distribution up to quite large thicknesses, and also supplies a correction factor to improve the agreement at large angles, where Molière theory is less accurate. The theory of Snyder and Scott [80] (1949), which also uses the small-angle approximation, was shown to be equivalent to Molière theory by Scott [63].

Molière's theory is distinct from similar theories because he did not use a Yukawa potential (Equation 5.2) and the first Born approximation, as done by Wentzel (and others), to describe the screened potential field of the nucleus. Instead he made his own calculation using the Thomas-Fermi field [69, 68] based upon the numerical solutions calculated and tabulated by Bullard and Massey [81]. He obtained the following potential [63]:

$$V(r) = \frac{Z_1 Z_2 e^2}{r} \omega_M(r, R),$$

where his fit can be written as $\omega_M(r') = 0.10e^{-6r'} + 0.55e^{-1.2r'} + 0.35e^{-0.3r'}$, by setting $r/R = r'$. As discussed in Chapter 5, the atomic size, R, is commonly defined according to the Thomas-Fermi radius (Equation 5.3). The Thomas-Fermi field is not considered to give an accurate description of the scattering field in low Z materials, however, as it only works well in atoms with a sufficient number of electrons, and so becomes inaccurate in light elements [82].

One of the most important results in Molière theory is that scattering is described through a single parameter known as the screening angle*, which was introduced in Chapter 5. The Molière screening angle is defined as [70]:

$$\chi_a = \chi_0 \sqrt{1.13 + 3.76\left(\frac{\alpha Z}{\beta}\right)^2}, \tag{6.1}$$

calculated using the eikonal approximation†, where the squared term represents the deviation from the Born approximation, i.e. the Born screening angle $\theta_1 (\equiv \chi_0)$ defined in Equation 5.9. Molière's modification is negligible however for muons of $O\,(200\,\mathrm{MeV}/c)$.

Molière describes the thickness of the scattering material, t, via a second parameter, the unit probability angle χ_c [70]:

$$\chi_c^2 = 4\pi N t e^4 Z^2/(p\beta)^2, \tag{6.2}$$

where N is the number of scattering atoms per cm^3. χ_c can be interpreted as being the angle for which on average there is only one collision with $\theta > \chi_c$. The ratio $\chi_c^2/\chi_a^{'2}$ represents the effective number of collisions in the target,

$$\frac{\chi_c^2}{\chi_a^{'2}} = \frac{6680t}{\beta^2}\frac{(Z+1)Z^{1/3}}{A(1+3.34(\alpha Z/\beta)^2)} = e^b, \tag{6.3}$$

where $\chi_a^{'2} = 1.167\chi_a^2$ (following Bethe's derivation).

The Molière distribution function, as given by Bethe [70] in Equation 25, is:

$$f(\theta)\theta d\theta = \vartheta d\vartheta[f^{(0)}(\vartheta) + B^{-1}f^{(1)}(\vartheta) + B^{-2}f^{(2)}(\vartheta) + ...]$$

where $\vartheta = \theta/(\chi_c B^{1/2})$ and $f^{(n)}$ are functions of ϑ, where the first term, $f^{(0)}$, is Gaussian.

*Goudsmit-Saunderson theory also uses a single parameter but Molière theory is simpler and considerably more transparent [70].

†A high-energy, small-angle approximation that neglects spin effects [83]. Subsequent derivation of Molière's screening angle, χ_a, with modern computing techniques, where the Molière cross-section was evaluated numerically, has highlighted the accuracy of Molière's original method [84, 85].

The parameter B is the solution to the following equation:

$$B - \ln B = b,$$

where b was defined previously in Equation 6.3, but is included only for completeness. The key point is that the distribution of angles is obtained solely using the angles χ_c and χ_a.

Molière makes certain approximations and assumptions to obtain the distribution function in a semi-analytical form, which is calculated and tabulated in the papers of Molière [78] and Bethe [70], and plotted in Ahn's 1992 review [82]. Monte Carlo codes incorporate MCS theories, in tabulated form (often with additional parametrizations and assumptions), to obtain scattering angle distributions after material.

6.3 The Bethe and Fano modifications to Molière theory

In its original form, Molière theory did not include scatters from atomic electrons, despite the fact they make a significant contribution to the cross-section at low Z as was discussed in the previous chapter. Bethe attempted to correct this omission, following a suggestion by Kulchitsky and Latyshev (1941) [86], by modifying the squared unit probability angle χ_c^2 (Equation 6.2) by replacing the Z^2 factor with $Z(Z+1)$, given as Equation 10 in his paper [70]. Bethe reports excellent agreement with the 15.7 MeV electron scattering measurements, in beryllium and aluminium, of Hanson et al. [87], improving upon the original Molière result. Lynch and Dahl comment that this agreement may well be fortuitous in light of the known inaccuracies of the Thomas-Fermi field at low Z [71].

Bethe's $Z(Z + 1)$ modification to χ_c^2 was soon disputed by Fano in his 1954 paper [79], on the basis that it incorrectly assumed that nuclear (elastic) and electron (inelastic) collisions contribute equally to the cross-section. Fano retained the $Z(Z + 1)$ factor only for incident electrons, and reverted to Molière's original Z^2 definition for heavy incident particles.

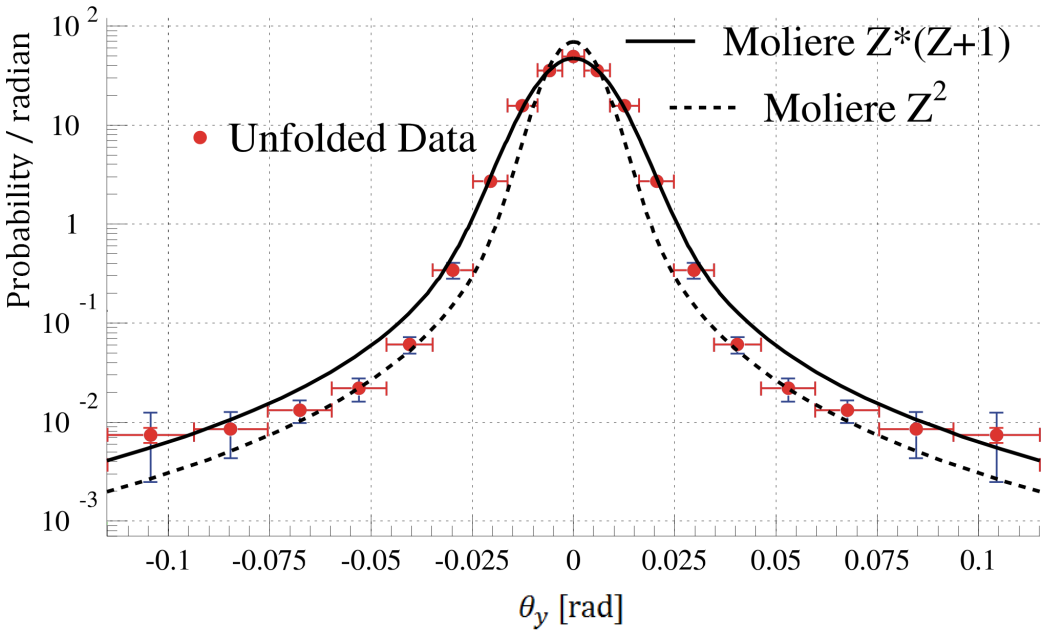

Figure 6.2: Projected scattering angle distribution for $p = 172\,\text{MeV}/c$ muons in 15.9 cm LH_2 as measured by The MuScat Experiment and predicted by Molière theory, taken from [28].

Unlike Bethe and Molière, Fano considered the scattering cross-section, σ, as the sum of distinct elastic (σ_{el}) and inelastic (σ_{inel}) components (taken from Equation 2 of Fano's paper [79]):

$$\sigma(\chi) = \sigma_{el}(\chi) + \sigma_{inel}(\chi),$$

as they depart differently from the Rutherford formula. To account for this Fano introduced an inelastic cut-off angle, χ_{in}, into Molière theory by modifying the parameter b (Equation 6.3) as shown in Equation 13 of [79]. Since the electrons are not technically screened by the nucleus χ_{in} can be interpreted solely as corresponding to a low-angle cut-off to the Rutherford cross-section, $\equiv \theta_1^e$, which was introduced in the previous chapter. Unfortunately Fano gives only an integral form for χ_{in} in his paper, rather than a simple equation. As shown in Chapter 4, however, it is reasonable to assume $\theta_1^e \approx \theta_1$ in low Z materials, where θ_1^e is defined (roughly) as the angle corresponding to an energy transfer equal to the binding energy of the electron (as illustrated in Figure 4.2).

At larger angles however the electron and nuclear distributions are markedly different. As discussed in Section 5.4.1, scatters with electrons are kinematically limited to a maximum angle of $\theta_2^e \approx 4.8\,\text{mrad}$, which is much less than the corresponding angle for nuclei, θ_2, apart from at

very low kinetic energies ($\approx 3\,\mathrm{keV}$). As a result, only nuclear deflections contribute to the single-scattering tails of distributions (which follow Z^2), since electrons do not contribute above θ_2^e. This effect is clear in Figure 6.2 which shows the probability (per radian) distribution measured by MuScat compared with two Molière distributions, where χ_c^2 is defined using Z^2 and $Z(Z+1)$ (Bethe) respectively. The distributions are for a $p = 172\,\mathrm{MeV}/c$ muon beam on a 15.9 cm LH_2 target, all of which are given in the MuScat paper [28]. The data are clearly in better agreement with the Z^2 curve at moderate to large angles, which is reasonable since only nuclei contribute to the cross-section. At small-angles, however, the data agree with the Bethe modification ($Z(Z+1)$), which is consistent since electron scattering contributes to the distribution. Electron scattering contributes most significantly to the total atomic cross-section in LH_2, i.e. at the lowest Z, so the effect becomes less important in larger atoms. Scott [63] describes how to apply Fano's treatment to thick compound targets, as the original treatment is only applicable for thin elementary targets.

Berger and Wang supply numerical correction factors with which χ_a can be multiplied to provide an analogous screening angle according to the more accurate Hartree-Fock potential [85], parametrized by Cox and Burnham [88]. Gottschalk et al. helpfully plot the factors in their review (Figure 17) [89], but note that the net effect of the correction is small due to fact that the screening angle generally enters Molière theory as a logarithm, through the b parameter.

6.4 NSW theory

A related theory is NSW theory [90] which was proposed by Nigam, Sundaresan and Wu in 1959. They used a differential cross-section derived using the second Born approximation, and also claim to correct (alleged) errors in Molière's original calculation, although Gottschalk et al. are somewhat sceptical of their validity in Section 5.1 of their paper [89]. Whilst NSW theory isn't in common usage it does share similarities with Molière theory, as Gottschalk et al. note, in that scattering enters through the ratio χ_c^2/χ_a^2. In NSW theory the squared screening angle is defined as

$$\chi_a^2 = (\mu\chi_0)^2\left\{1 + 4\alpha(\mu\chi_0)\left[\left(\frac{1-\beta^2}{\beta}\right)\ln(\mu\chi_1) + \frac{0.2310}{\beta} + 1.4480\beta\right]\right\}, \tag{6.4}$$

where μ is a constant of order 1 [90], set to 1.8 from fits to Au and Be data. At momenta of $O(200\,\mathrm{MeV}/c)$ ($\beta \sim 0.89$) the braced term is very close to unity and the equation reduces to:

$$\chi_a = \mu\chi_0. \tag{6.5}$$

where $\chi_0 \equiv \theta_1$ (defined in Equation 5.9). Whilst claimed to be superior to Molière theory by its authors, Scott neglects to give a conclusive opinion in his review [63]. A simpler, approximate form of the theory was published by Marion and Zimmerman [91] in 1967. They also emphasized the difference between NSW theory and Molière theory was "quite small", based upon proton scattering measurements at medium energies ($\sim 100\,\mathrm{MeV}$). More recent analysis by Gottschalk et al. [89] (1992) disagreed entirely however, finding NSW theory (in both forms) to be in "substantially worse" agreement with the experimental results than Molière theory. They add that NSW theory does not incorporate atomic electron scattering, energy loss and compounds and mixtures, and can therefore be considered "less complete" than the Fano-Molière formalism. Ahn [82] also finds NSW theory to overestimate the angular distribution, most significantly in Ag and Ta.

6.5 Comparison with experiment

Gottschalk et al. collate and analyse the results of seven proton scattering experiments from energies of 1 MeV to 200 GeV (including their own measurements at 160 MeV) and find the Fano-Molière form "accurate to better than 1%" on average across many different target materials at medium energies [89]. Lynch and Dahl [71] consider the Bethe form to be superior to Fano formalism, citing the measurements by Shen et al. [92]. Whilst Gottschalk et al. agree with Lynch and Dahl in that the Bethe form is more accurate in hydrogen, they find the Fano formalism to be better in Beryllium, a discrepancy which was not understood. For the purposes of muon cooling, however, only heavy particle scattering at $100-300\,\mathrm{MeV}/c$ is really of relevance. Unfortunately no comparison was made between the MuScat measurements and the Fano-Molière treatment in the MuScat paper [28], only with the Bethe and original Molière forms.

Ahn's 1992 review [82] makes comparisons between different theories (using various Molière

treatments) and measurements in Al ($Z = 13$), Ag (47) and Ta (73)) but not in low Z materials unfortunately. Distributions are derived using Molière theory in its original form and the Bethe and Fano revisions, with both the Thomas-Fermi potential (as is standard) and the more accurate Hartree-Fock potential, as well as using NSW theory. Ahn finds the different Molière treatments to all compare well with the experimental distributions apart from in thin foils and at low energies.

The treatment of electrons in Molière theory was reexamined more recently by Tollestrup and Monroe in 2000 [93], who make different changes to Fano, in an attempt to improve the accuracy of the Thomas-Fermi model at low Z. The Bethe, Fano and Tollestrup and Monroe forms of Molière theory are implemented in ICOOL. Fernow presents a comparison of the three models, and ELMS, with the MuScat measurements in [94] (2006) finding very good agreement. The Bethe model is found to exaggerate the scattering at large angles in all materials, most significantly in LH_2. The other models are in excellent agreement with MuScat up to 80 mrad. In contrast, the MuScat Collaboration made comparisons of their data with the Geant4 MCS models and found poor agreement [28].

Gottschalk et al. emphasize the opportunity for future experiments to make an impact in this area: "It will take more experimental and theoretical work to clarify the situation at very low Z", achieved partly through the MuScat Experiment in 2003 [28]. MICE has an opportunity to make such an impact by making its own muon scattering measurements, which are discussed in Chapter 8.

6.6 Summary

Multiple scattering theories solve the transport equation (Equation 6.1), using a specific DCS, to obtain distributions of scattering angles after material. Solutions involve the use of complex approximations and numerical calculations, the results of which are given (typically) in tabulated form. These theories are then implemented in MCS models in Monte Carlo codes such as Geant4, although the underlying physics involved can be largely obscured.

No real consensus exists on which MCS theory is best able to reproduce experimental results, although many theories are in fact very similar. Molière theory is the most commonly used theory,

but there is significant disagreement in literature over the correct treatment of electrons (Bethe, Fano, Tollestrup and Monroe), as discussed. Recent ICOOL studies by Fernow, however, find all three treatments to be in very good agreement with the measured distributions of the MuScat Experiment [28]. Fernow's results are consistent with Ahn's conclusions [82] but less so with the findings of Gottschalk et al. [89], although both authors compare only against proton scattering measurements.

As discussed in Chapter 3, the standard cooling formula (Equation 2.9) and Monte Carlo disagree by up to 30% in LH_2. This disagreement comes from their differing treatment of multiple scattering. Whilst the agreement was improved using new, more accurate MCS approximations, derived in Chapter 5, there is no reason to assume that the Monte Carlo results are accurate. As noted in Section 4.2, strong step length dependencies were found in earlier releases of the Monte Carlo. These issues raised the question of whether a much simpler MCS model could be developed, in which the physics is transparent and involves few approximations. Chapter 7 presents a new, original Monte Carlo model for scattering in which distributions are obtained from the Wentzel cross-section (Equation 5.17) without using a MCS theory. As a result the model is an entirely different approach to the models in standard Monte Carlo codes such as Geant4. The accuracy of the new model is assessed against the scattering measurements of MuScat, and compared with other Monte Carlo (Geant4, ELMS).

Chapter 7

A Simple Monte Carlo Model for Multiple Scattering

A simple Monte Carlo scattering model was developed to test whether scattering angle distributions could easily be obtained using just the fundamental physics. The model samples directly from the Wentzel single-scattering cross-section and simulates all collisions with nuclei and electrons. Comparison with the results of the MuScat Experiment showed excellent agreement in LH_2 and good agreement in higher Z materials up to Al.

Monte Carlo transport codes such as Geant4 [44] and ICOOL [47] use "condensed" physics models to handle processes such as multiple Coulomb scattering (MCS) and energy loss. As discussed in Chapter 6, scattering models are based on a theory of multiple scattering, which obtains the distribution of angles from a single-scattering cross-section. Scattering models use these results to generate distributions for finite thicknesses of material.

As shown in Chapter 3, there is significant disagreement between Maus/Geant4 and the standard PDG equation for the rms projected scattering angle, and step length instabilities that were not understood. Verification of the actual physics used in such models is particularly difficult, however, as the implementation of scattering in a Monte Carlo can involve additional approximations and assumptions.

This chapter describes a model for MCS which is transparent and based on only well-known physics, returning to the fundamental cross-section of Wentzel which was introduced in Chapter 5. Unlike standard treatments it does not use a theory of multiple scattering, and as a result contains no complex parametrizations or approximations. Instead it is a "brute-force" model which

simulates every scatter. The accuracy of the model is assessed through comparison with the measurements of the MuScat Experiment (2003) [28], performed at the TRIUMF laboratory, which was the first experiment to study muon scattering at the typical momentum for cooling channels of $O(200\,\mathrm{MeV}/c)$.

7.1 The XYZ model

The XYZ Model was developed to provide a simple treatment of MCS which can be clearly implemented and understood. It obtains the distribution of scattering angles after a finite thickness of material by repeatedly sampling the cross-section, simulating all collisions. The resultant angular scattering distribution is then obtained for a beam through an absorber. The model only considers scattering and makes no inclusion of energy loss, which is relatively unimportant in thin absorbers. Scattering and energy loss are also largely independent processes in all materials other than LH_2, as discussed in Section 4.3. The XYZ model is intended as a test of the underlying physics of scattering, and not as a comprehensive, all-particle transport code such as Geant4.

The model makes "detailed" simulations* of particle scattering in material, where all collisions experienced by a particle are simulated in succession. For each collision the model samples the angle of scattering, θ, from the DCS. The total number of collisions made by particles is assumed to be Gaussian distributed about the mean value, which is calculated in the model. The momentum, $p\,(\equiv p_z)$, number of particles, N, and the target material and thickness are external variables. The simplicity of the model means it can simulate all collisions of a 10^6 muon beam through an absorber in under 20 minutes.

The model uses the Wentzel DCS[64]:

$$\frac{d\sigma}{d\omega} = \left(\frac{2Z\alpha}{p\beta}\right)^2 \frac{1}{(\theta^2 + \theta_1^2)^2},$$

(Equation 5.4), for scattering from screened nuclei to obtain the distribution of scattering angles after a finite thickness of material. Screening is described through the screening angle, θ_1, as described in Chapter 5. The same form of $d\sigma/d\omega$ is used for electrons. The model will be now

be described in detail, and the results compared with the measurements of the MuScat Experiment [28].

7.1.1 Computing the number of collisions

The mean numbers of scatters with nuclei (N^N) and electrons (N^e) in a thickness dz are calculated by integrating over the differential scattering probability (Equation 5.17) [56] into a solid angle ω:

$$\Xi(\theta)d\omega dz = 4N\frac{Z^2}{A}r_e^2\left(\frac{m_e c}{\beta p}\right)^2\frac{d\omega}{(\theta_1^2+\theta^2)^2}dz,$$

where the parameters θ_2 and θ_2^e are the upper limits of integration respectively, and $\theta_1^e = \theta_1$. The four parameters were first introduced in Chapter 5. Incident particles scatter off nuclei into the range $0 < \theta < \theta_2$ and off electrons into $0 < \theta < \theta_2^e$. The mean number of collisions with nuclei in Δz is

$$\begin{aligned} N^N &= \Delta z\int_0^{\theta_2}\Xi(\theta)d\omega = \kappa\Delta z\int_0^{\theta_2}\frac{2\pi\theta}{(\theta^2+\theta_1^2)^2}d\theta, \\ &= \pi\kappa\Delta z\left[\frac{\theta_2^2}{\theta_1^2(\theta_1^2+\theta_2^2)}\right], \end{aligned} \tag{7.1}$$

and similarly for electrons:

$$\begin{aligned} N^e &= \Delta z\int_0^{\theta_2^e}\Xi(\theta)d\omega = \kappa\Delta z\int_0^{\theta_2^e}\frac{2\pi\theta}{(\theta^2+\theta_1^{e^2})^2}d\theta, \\ &= \frac{\pi\kappa\Delta z}{Z}\left[\frac{\theta_2^{e^2}}{\theta_1^{e^2}(\theta_1^{e^2}+\theta_2^{e^2})}\right], \end{aligned} \tag{7.2}$$

where Δz is the material thickness in g/cm^2. The constant κ is

$$\kappa = 4N_A\frac{Z^2}{A}r_e^2\left(\frac{m_e c}{\beta p}\right)^2$$

cm^2 mol^{-1}, so N^N scales with Z^2 whilst N^e scales only with Z. For $p = 172\,\text{MeV}/c$ muons ($\beta =$

*Monte Carlo MCS models can be roughly classified as "condensed", "detailed" or "mixed" simulations [54], as discussed in Section 4.3.

0.89) $\kappa = 7.31 \times 10^{-6}\,\mathrm{cm}^2\ \mathrm{mol}^{-1}$. Table 7.1 gives N^N and N^e values in six low Z materials and Fe, using three definitions for θ_1. For compounds the mean value is calculated using the weighted average $N^{N,e} = \Sigma N_i^{N,e} A_i / A_{MW}$, where the i denotes the type of atom and A_{MW} is molecular weight of the compound. Table 7.2 gives values for $\theta_1 (\equiv \theta_1^e)$ and θ_2 in six materials. Since both $\theta_2 \gg \theta_1$ and $\theta_2^e \gg \theta_1^e$, Equations 7.1 and 7.2 reduce (approximately) to $N^N \propto 1/\theta_1^2$ and $N^e \propto 1/\theta_1^{e^2}$ respectively. As a result, in LH_2 there are equal numbers of electron and nuclear collisions ($N^e = N^N$), since the expressions are identical at $Z = 1$ (assuming $\theta_1^e \equiv \theta_1$). On average, a 172 MeV/c muon experiences 1164 nuclear and electron collisions per g/cm^2 of LH_2, using the Born value for θ_1. This amounts to a total of $\approx 12,000$ collisions in the 10.9 cm LH_2 MuScat absorber. In higher Z materials the fraction of electron scatters rapidly diminishes, as N^e scales only with Z compared with Z^2 for nuclei. In Fe for example, one would expect an average of 6488 electron scatters per cm (using the Born θ_1), which accounts for just 4% of the total number of scatters, 175204.

The maximum angle for nuclear scatters[†], θ_2, is related to the size of the nucleus, and is calculated using Equation 5.10. For 172 MeV/c muons in LH_2, θ_1 is approximately 830 mrad, which is very large compared to the rms width of the distribution after a thickness of 30 cm, for example. The maximum deflection from atomic electrons, $\theta_2^e \ll \theta_2$, as it is limited by kinematics, as discussed in Section 5.4.1. The limit is approximately 4.8 mrad, given by the mass ratio (m_e/m_μ) (Equation 5.15).

Material	Born		Molière		NSW	
	Nuclei	e$^-$	Nuclei	e$^-$	Nuclei	e$^-$
LH_2	1164	1164	1030	1030	359	359
Li	5171	1724	4566	1522	1596	532
Be	20227	5057	17830	4457	6243	1560
C	23832	3972	20906	3484	7356	1226
CH_2	12099	2016	10614	1769	3734	622
Al	47502	3654	40371	3105	14661	1127
Fe	168716	6488	128153	4928	52073	2002

Table 7.1: Mean number of scatters per g/cm^2 of material for a $p = 172$ MeV/c muon.

[†]As discussed in Section 5.3, very large angle (deep inelastic) scatters are possible, where $\theta > \theta_2$, but lie far away from the MCS distributions which are at small-angles.

Material	θ_1 [mrad]			θ_2 [mrad]	
	Born	Molière	NSW	Nuclei	e^-
LH_2	.022	.023	.040	829.7	4.84
Li	.031	.033	.056	436.1	4.84
Be	.034	.037	.061	399.7	4.84
C	.039	.042	.070	363.2	4.84
Al	.051	.056	.092	277.4	4.84
Fe	.064	.074	.115	217.6	4.84

Table 7.2: Angular parameters calculated for $p = 172\,\mathrm{MeV}/c$ muons, according to theory.

7.1.2 Iterative procedure

The model simulates all collisions experienced by an incident particle in an absorber, calculating the angular deflection (3D), θ, incurred in each scatter. The number of nuclear and electron collisions made by a particle can be assumed to be normally distributed about the mean values,

$$N_i^N = N^N + j\sqrt{N^N},$$
$$N_i^e = N^e + k\sqrt{N^e},$$

where j and k are Gaussian random numbers with mean= 0 and rms of 1, drawn for each incident particle. The total number of collisions experienced by particle i is $N_i^N + N_i^e$. The model uses simple probability to decide whether the particle scatters from a nucleus or an electron. For each collision a random number, k, is drawn from a uniform distribution between 0 and 1. If $k < N_i^e/(N_i^N + N_i^e)$, the particle scatters off an electron. If $k > N_i^e/(N_i^N + N_i^e)$, the particle scatters off a nucleus.

The scattering angles for collisions with nuclei are obtained from the following single-scattering distribution:

$$f(\theta) \propto \frac{\theta}{(\theta_1^2 + \theta_2^2)^2},$$

where θ_1 and θ_2 are replaced by θ_1^e and θ_2^e to obtain the electron distribution. Efficient sampling of $f(\theta)$ in the Monte Carlo is made using the integrated distribution, $F(\theta) = \int_0^\theta f(\theta)d\theta$, which evaluates to

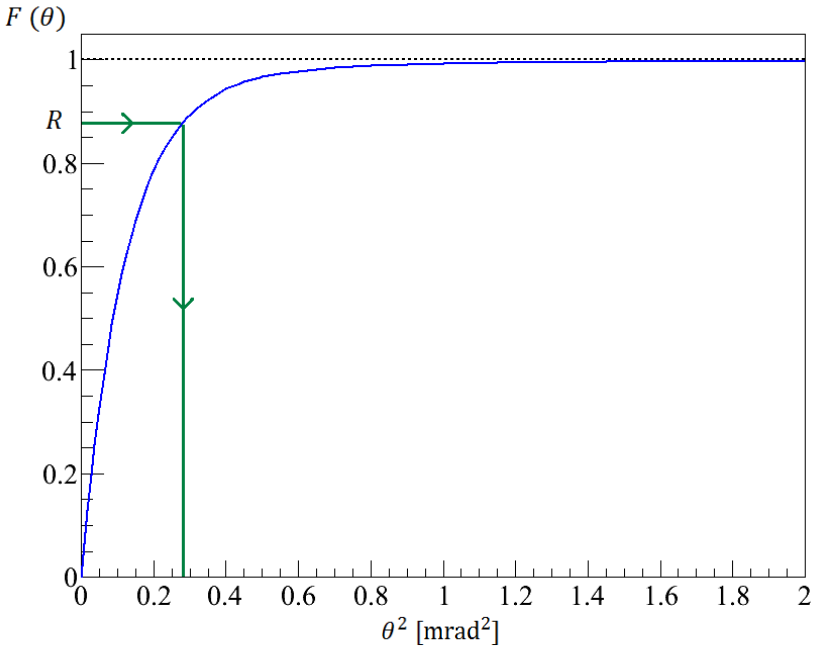

Figure 7.1: Integrated distribution of $F(\theta)$ (normalized). An angle of deflection, θ^2, is chosen for each collision using a random number, R, drawn from uniform distribution between 0 and 1.

$$F(\theta) = A\left[-\frac{1}{2}\frac{1}{(\theta_1^2+\theta^2)}\right]_0^{\theta} = -\frac{A}{2}\left[\frac{1}{(\theta_1^2+\theta^2)} - \frac{1}{\theta_1^2}\right], \tag{7.3}$$

where A is a constant. The function is normalized so $F(\theta_2) = 1$, where θ_2 is the maximum scattering angle from a nucleus. For every collision a random number, R, is drawn from a uniform distribution between 0 and 1. The scattering angle is given by $F(R)$, as illustrated in Figure 7.1. The constant term A can be written as

$$\frac{A}{2} = \left(\frac{\theta_1^2(\theta_1^2+\theta_2^2)}{\theta_2^2}\right).$$

Substitution into Equation 7.3 gives:

$$F(\theta) = \frac{(\theta_1^2+\theta_2^2)}{\theta_2^2}\frac{\theta^2}{(\theta_1^2+\theta^2)}.$$

Setting $F(\theta) = R$, the equation can be rearranged to give

$$\theta^2 = \frac{R\theta_1^2\theta_2^2}{\theta_1^2 + (1-R)\theta_2^2}.$$

The same method is used to the obtain the angular distribution for electron scatters, where θ_1^e and θ_2^e are used in place of θ_1 and θ_2 respectively.

The sampling procedure just described generates a polar angle around the muon direction for each collision. The scattering angles of successive collisions must be added vectorially. Consequently, for each collision an azimuthal angle, ϕ, is randomly generated between 0 and 2π, to obtain the (2D) projected scattering angles, θ_x and θ_y, defined as:

$$\theta_x = \theta \ \cos(\phi)$$

$$\theta_y = \theta \ \sin(\phi).$$

The model makes a running sum of θ_x and θ_y over all collisions in the absorber to calculate the total projected angles through which the particle is scattered. The total squared space angle for particle i is simply the sum of the squares,

$$\theta_i^2 = \Sigma\theta_x^2 + \Sigma\theta_y^2 \, .$$

For compound targets such as C_2H_4 (polyethylene) the method described above must be adapted to determine, for each collision, the type of atom off which the incident particle scatters, in this example either the two carbon or four hydrogen atoms. The probability of scattering by the two carbon atoms is proportional to the ratio nA_C/A_{MW}, where $n = 2$. A_{MW} is the molecular weight of the compound. As before, a random number, l, between 0 and 1 is drawn for each collision from a uniform distribution. If $l < nA_C/A_{MW}$, the particle scatters off a carbon atom. If $l > nA_C/A_{MW}$, the particle scatters off a hydrogen atom. The model then proceeds by determining the nature of the collision, be it with a nucleus or constituent electron, using the same method described earlier.

The screening angle, θ_1, has many definitions, depending on the preferred MCS theory. Three

definitions for θ_1 are used for the purposes of this study, given by Wentzel [64] (using the Born approximation), Molière [78] and Nigam, Sundaresan and Wu (NSW theory) [90]. All three use the Thomas-Fermi radius of the atom (Equation 5.3) to estimate the size of the atom. The simplest, and arguably the most transparent, definition was derived in Chapter 5 (Equation 5.9), where θ_1 is the de Broglie wavelength divided by the Thomas-Fermi radius, and will be referred to as the Born angle. Molière's screening angle, given in Equation 6.1, is very similar to the Born angle, since Molière's correction to the first Born approximation is small at $O(200\,\mathrm{MeV}/c)$. The NSW angle, at $p = 172\,\mathrm{MeV}/c$ (the MuScat momentum), is simply the Born angle multiplied by a constant scaling factor, μ, set to 1.8, and is given in Equation 6.5. As discussed in Section 5.4.1, it is reasonable, as a first approximation, to assume $\theta_1^e = \theta_1$. The sensitivity of the model to these parameters is investigated further in Section 7.3.

Figures 7.2 and 7.3 show the projected and space angle scattering distributions for a beam of 10^6 muons, at $p = 172\,\mathrm{MeV}/c$, after 10.9 cm of LH_2 and 3.73 mm of Be. The nuclear and electron scattering distributions are shown separately, along with the overall "atomic" distribution which is the sum of the two. As expected the electron and nuclear angular distributions in LH_2 are similar since N^N and N^e are identical at $Z = 1$, where $N^{N,e} = 12,000$ collisions, on average, in 10.9 cm. A scatter with a nucleus, however, can give a much larger deflection ($\theta_2 = 830$ mrad) than with an electron ($\theta_2^e = 4.84$ mrad) so the distributions are not identical. As shown in Figure 7.2 the nuclear scattering distribution runs to larger angles ($\theta \sim 32$ mrad) than for electrons (~ 22 mrad).

In Be a particle will scatter approximately six times more with nuclei than with electrons, since the fraction of electron collisions drops rapidly in progressively higher Z materials. Hence, the angular distributions for Be look very different from those for LH_2, as shown in Figure 7.3. The electron scattering distributions are concentrated at small-angles whereas the nuclear distributions extend to large angles and are very similar to the atomic distributions. As Z increases, scattering from electrons rapidly becomes unimportant to the scattering distribution. In Fe for example, which has $Z = 26$, a particle has only a 3% probability of scattering from an electron instead of the nucleus. The model will be now compared with the distributions measured by the MuScat Experiment [28].

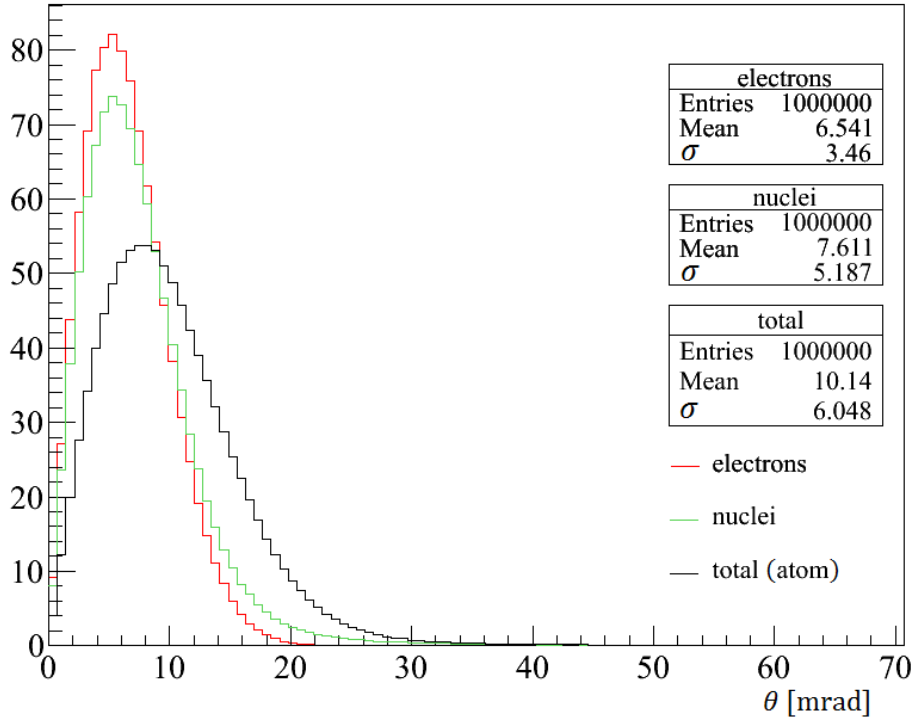

(a)

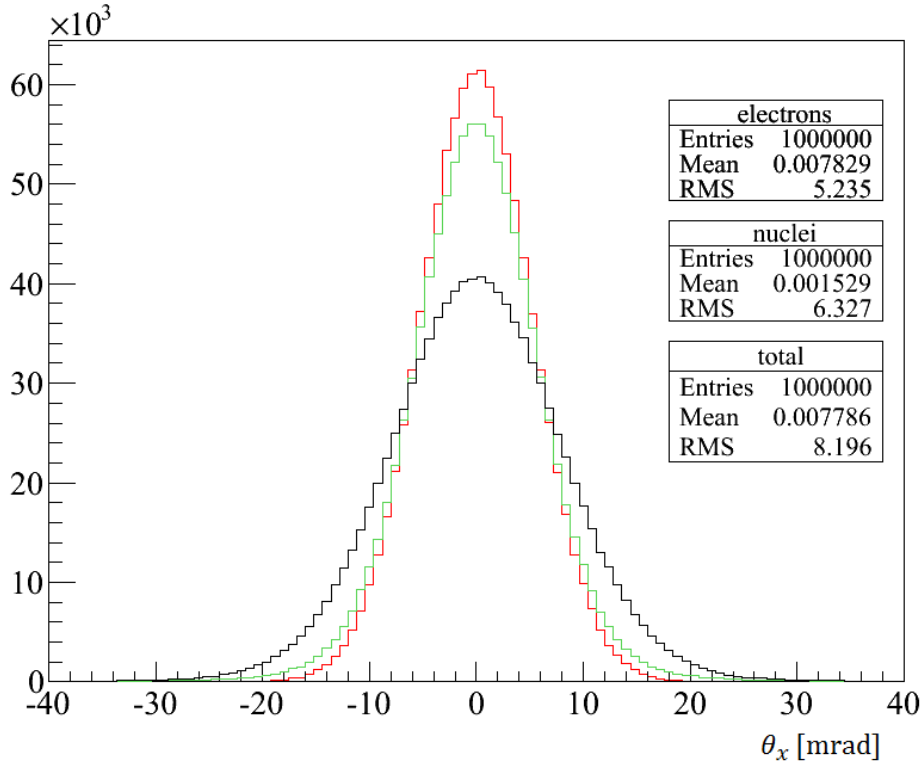

(b)

Figure 7.2: Distributions of space (a) and projected (b) scattering angles generated in the XYZ model for 10^6 muons at $p = 172\,\mathrm{MeV}/c$ after 10.9 cm of LH_2. θ_1 is defined according to the Born approximation. The total, atomic distribution is simply the sum of the electron and nuclear contributions.

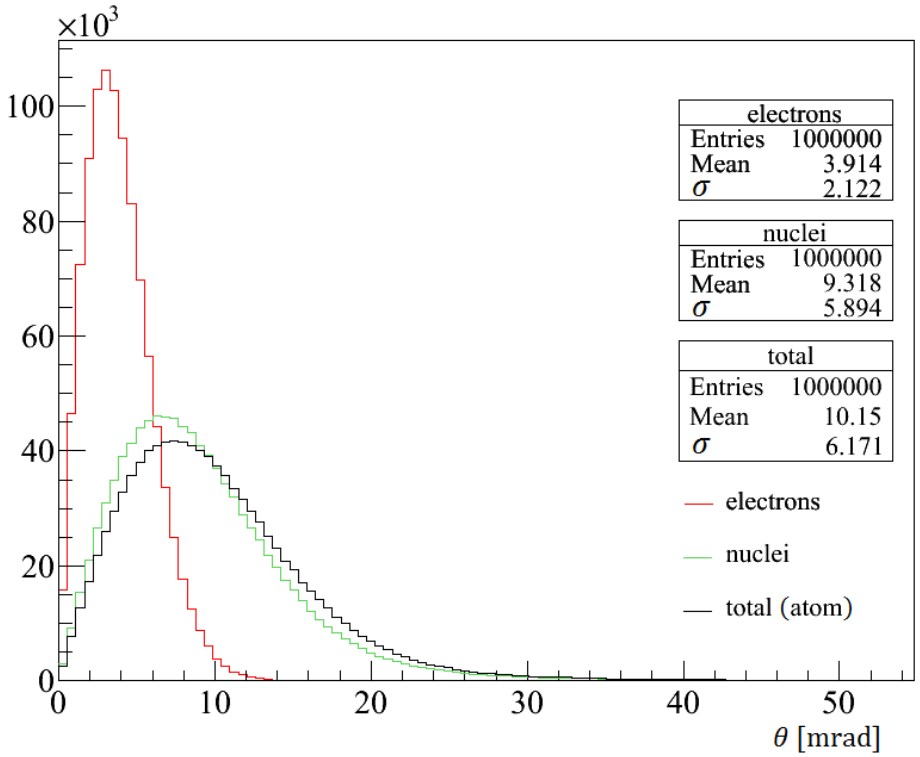

(a)

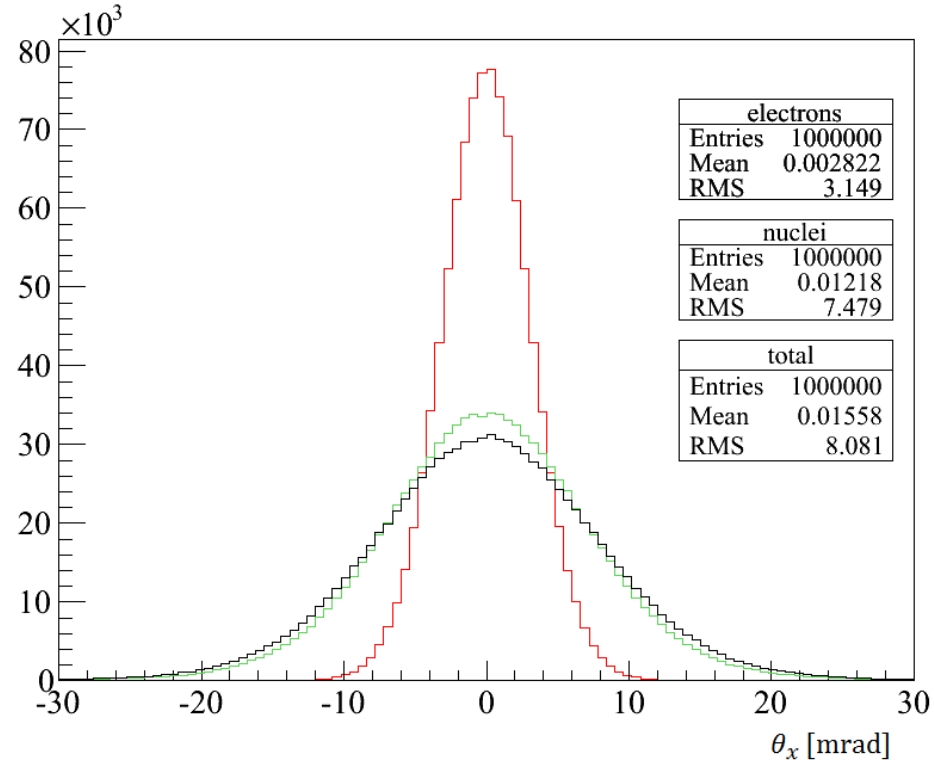

(b)

Figure 7.3: Distributions of space (a) and projected (b) angles after 0.373 cm of Be, see Figure 7.2.

7.2 Comparison with the MuScat Experiment

The MuScat Experiment [28] made scattering measurements of 172 ± 2 MeV/c muons in six elements: LH_2, Li, Be, C, Al and Fe, and the compound CH_2. Scattering distributions were measured using a tracker consisting of three double scintillating-fibre planes (read out by PMTs), positioned 1100 mm from the target. A series of lead collimators were positioned upstream of the target to define the beam at input. Two scintillator planes were used to identify particles that scattered in the lead and lost large amounts of energy. Solid targets were housed in a wheel controlled by a stepper motor; the LH_2 targets were contained in a separate vessel with thin mylar windows. A calorimeter (known as 'TINA') was positioned at the end of channel to study the composition of the beam. Figure 7.4 shows a Geant4 model of the experiment.

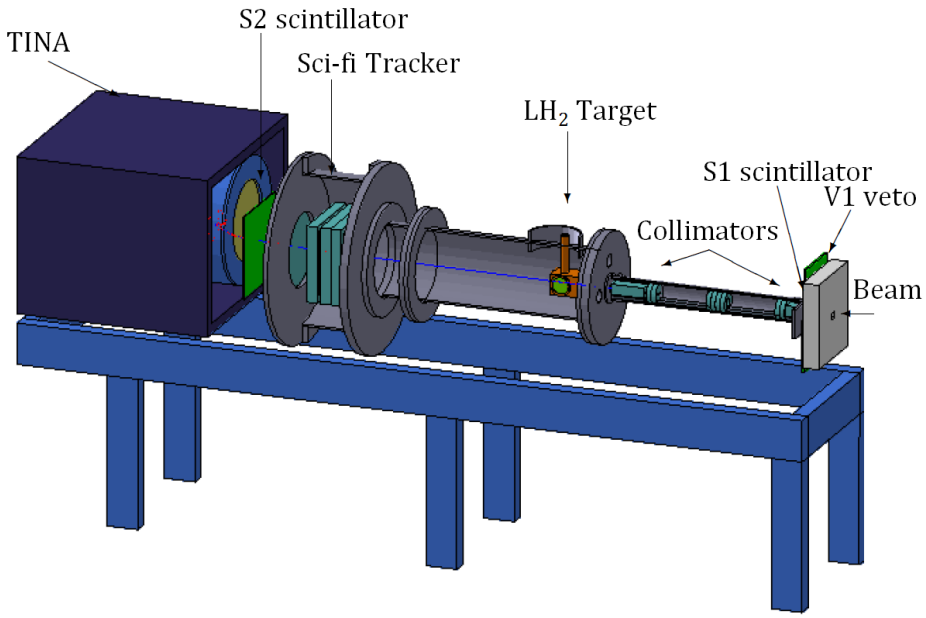

Figure 7.4: The MuScat detector, from the Geant4 model. Figure and caption taken from [28].

The MuScat Collaboration give their results as binned probability distributions in Table 2 of their paper [28]. The paper compares the measured distributions with the predicted distributions of Geant4.7.0p1 and ELMS (for LH_2), which are also tabulated. The paper concludes that none of the models are found to provide a good description of the data, with the exception of ELMS, which only works with LH_2. The MuScat results provide an excellent benchmark against which the new model will now be compared.

Target		Δz	ρ [g cm^{-3}]	Events
LH_2	(i)	10.9 cm	0.0755	2267683
	(ii)	15.9 cm	0.0755	1127045
Li	(i)	6.4 mm	0.53	882449
	(ii)	12.78 mm	0.53	1215336
Be	(i)	0.98 mm	1.85	500766
	(ii)	3.73 mm	1.85	1186528
C		2.5 mm	1.69	801899
CH_2		4.73 mm	0.93	802426
Al		1.5 mm	2.70	1201280
Fe		0.24 mm	7.86	845020

Table 7.3: Description of the ten targets used in the MuScat Experiment, taken from Table 1 of [28].

Simulations were made using the XYZ model for ten of the MuScat targets, listed in Table 7.3, using 10^6 muons with $p_z = 172\,\text{MeV}/c$. The measured LH_2 density, $0.0755\,\text{g/cm}^3$, was used instead of the standard value of $0.0708\,\text{g/cm}^3$. Angular scattering distributions were converted to probability distributions for comparison with MuScat. Figures 7.5 to 7.9 show the probability distributions obtained with the model for seven materials using the Born θ_1, which is defined as $\theta_1 = (Z^{1/3} m_e c)/137p$ (Equation 5.9), where the size of the atom is defined using the Thomas-Fermi radius.

Errors are proportional to $1/\sqrt{N}$, where N is the number of incident particles, but the errors bars are too small to be visible. The MuScat, Geant4.7.0p01 and ELMS (in LH_2 only) distributions are plotted also along with their respective errors, taken from the MuScat paper [28]. Distributions according to Molière theory (both the original and Bethe's revised form) are also compared with the MuScat data in the paper, as shown in Figure 6.2. The MuScat data for the 6.4 mm Li (i) and 0.98 mm Be (ii) targets have large errors in the tails, as is visible in Figures 7.6a and 7.7a, due to the large background subtraction required. Note that the MuScat Collaboration folded their distributions about zero to double the statistics so their histograms are symmetric, unlike the model results.

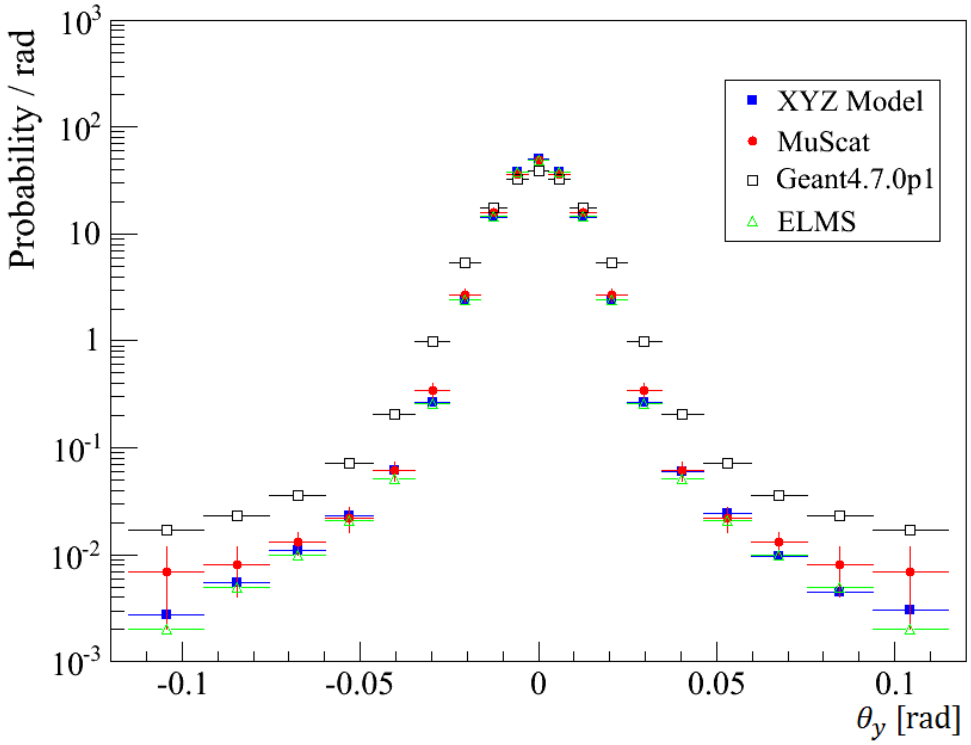

(a) 10.9 cm LH_2

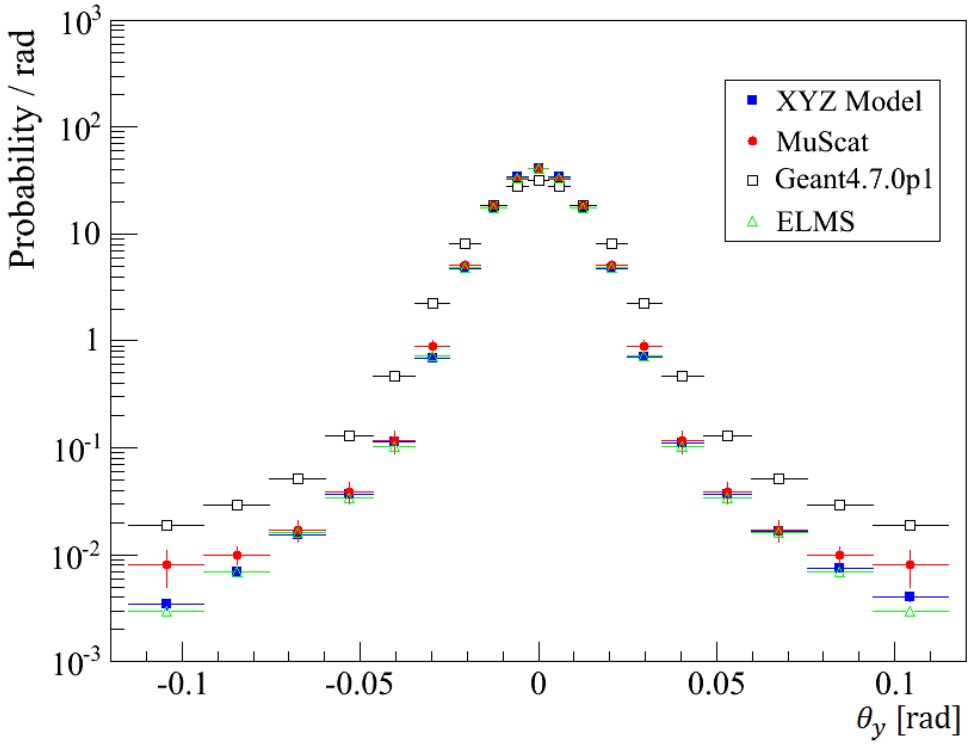

(b) 15.9 cm LH_2

Figure 7.5: Scattering probability distributions for liquid hydrogen (LH_2) obtained using the XYZ model compared with the MuScat data and other Monte Carlo, for $p = 172\,\mathrm{MeV}/c$ muons. The θ_1 parameter is defined according to the Born approximation.

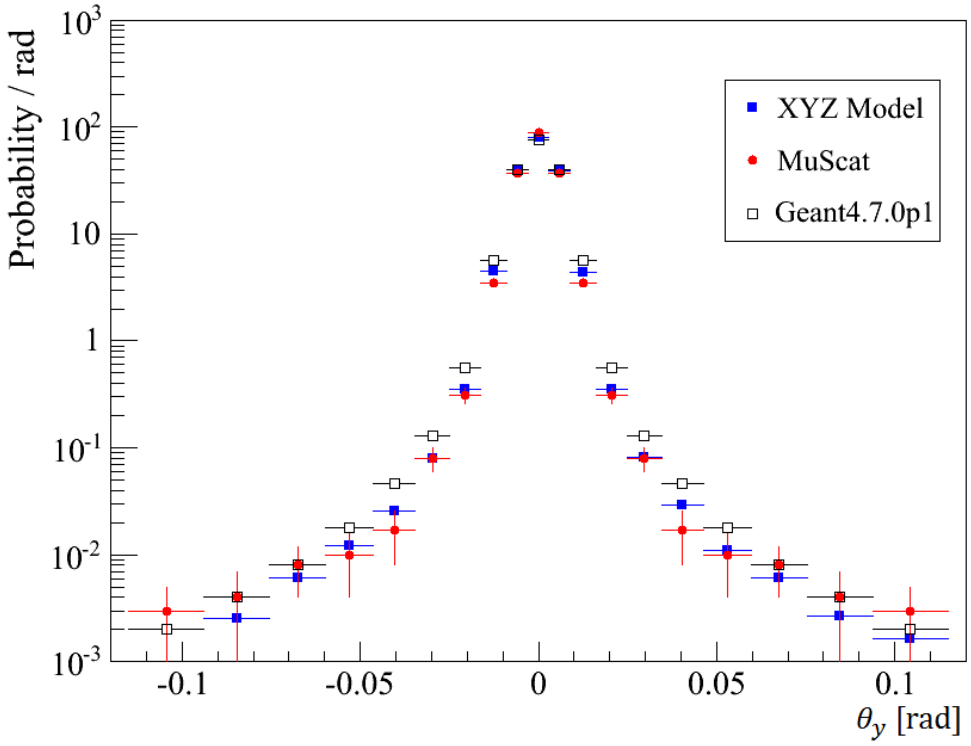

(a) 6.4 mm Li.

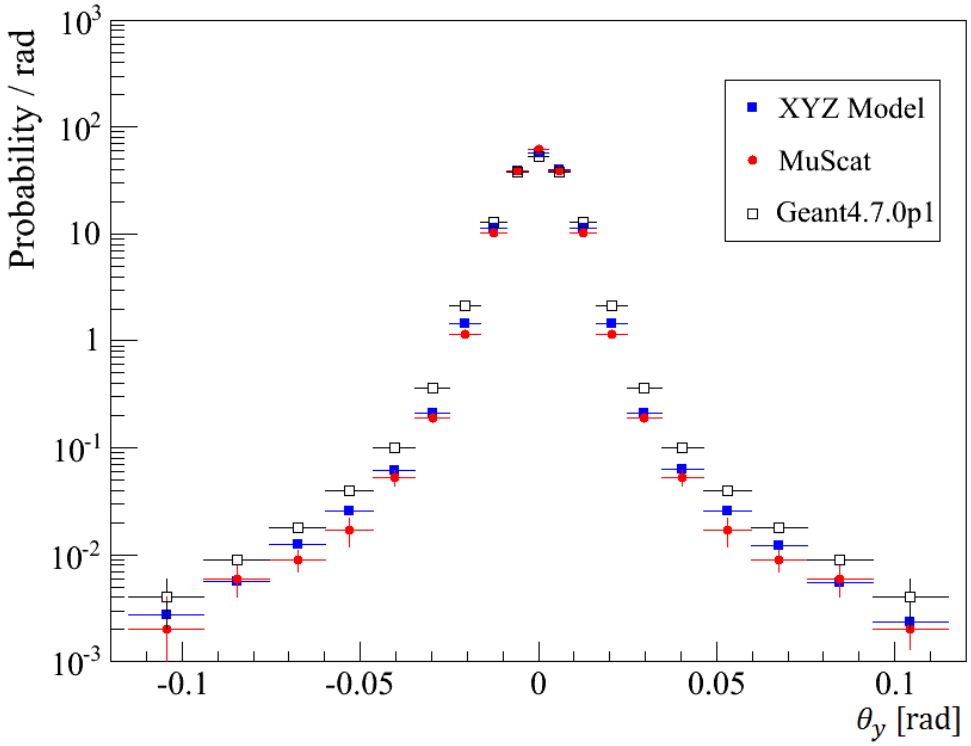

(b) 12.78 mm Li.

Figure 7.6: Scattering probability distributions for the two lithium targets, as described in Figure 7.5.

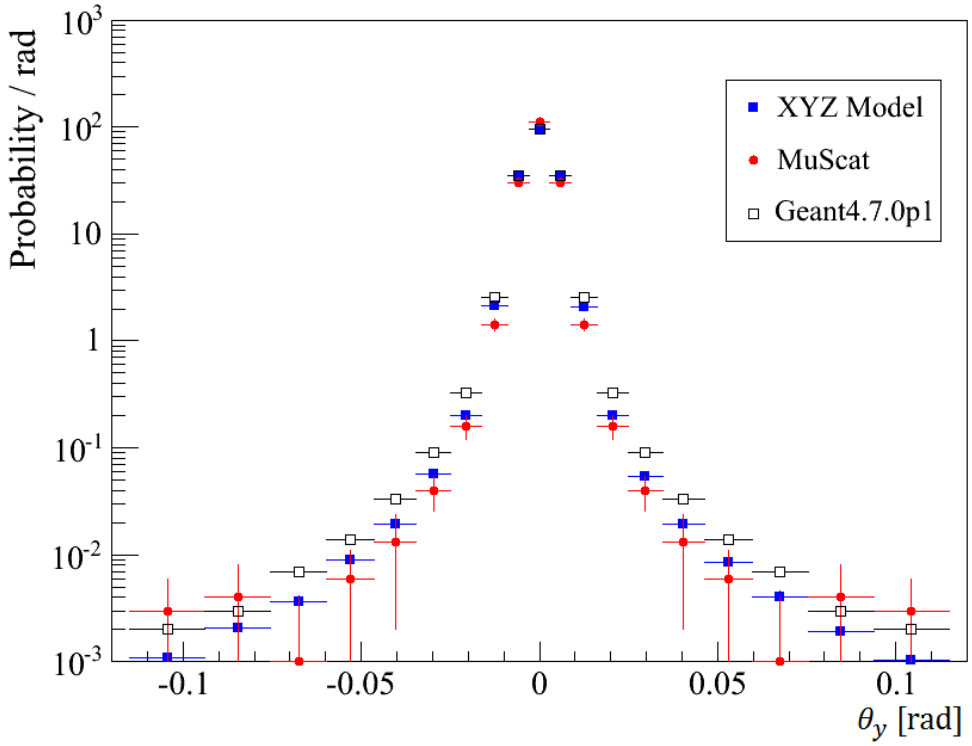

(a) 0.98 mm Be.

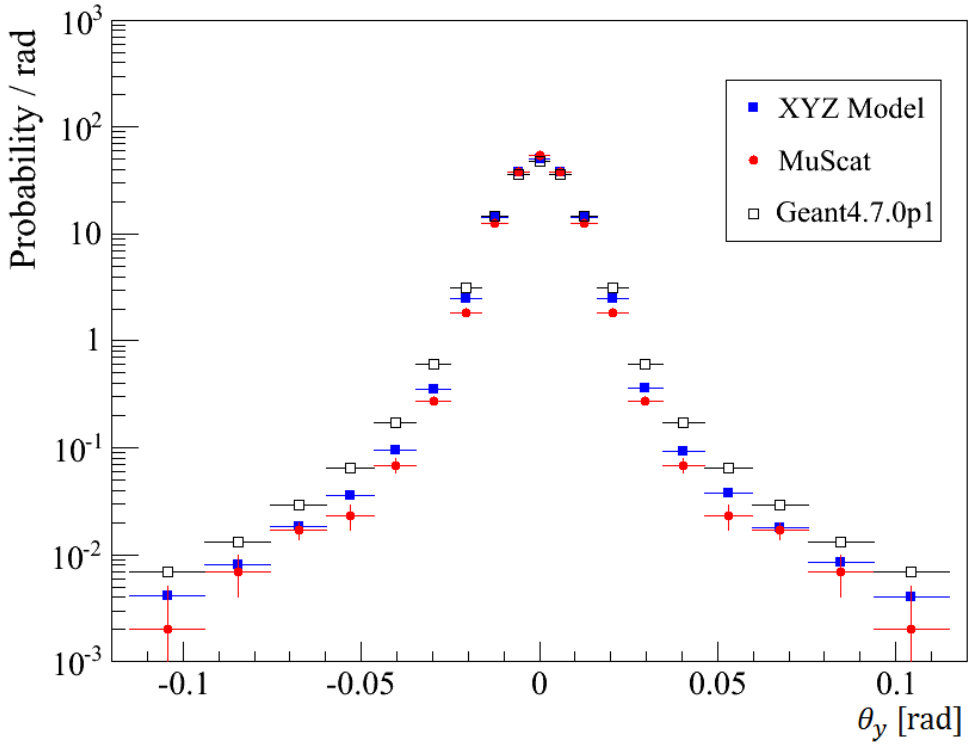

(b) 3.73 mm Be.

Figure 7.7: Scattering probability distributions for the two beryllium targets, as described in Figure 7.5.

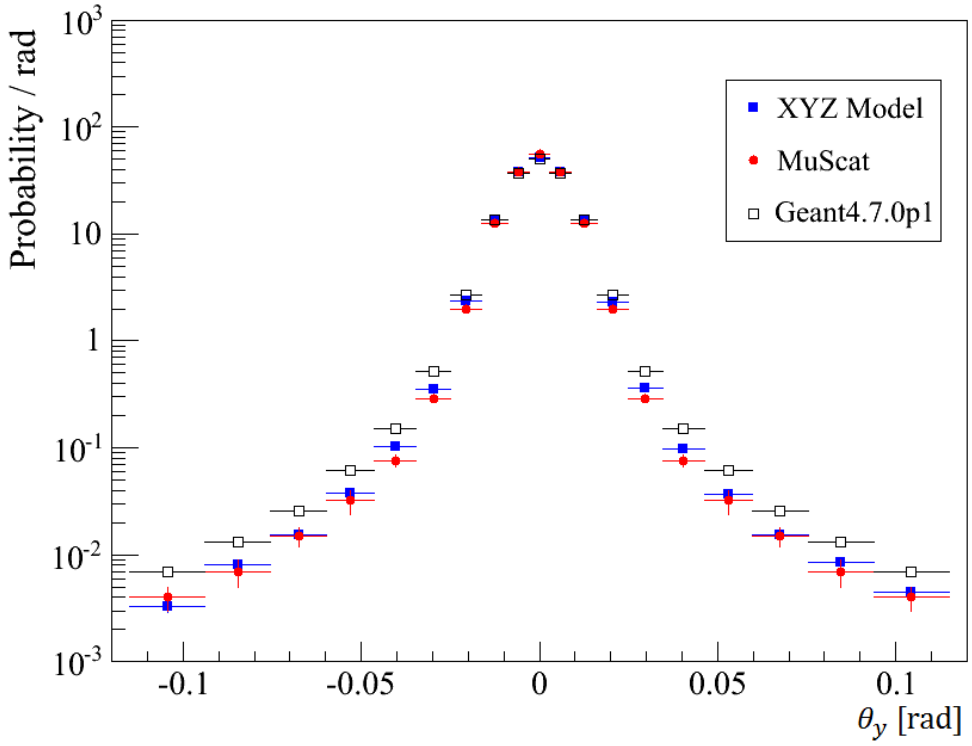

(a) 2.5 mm C.

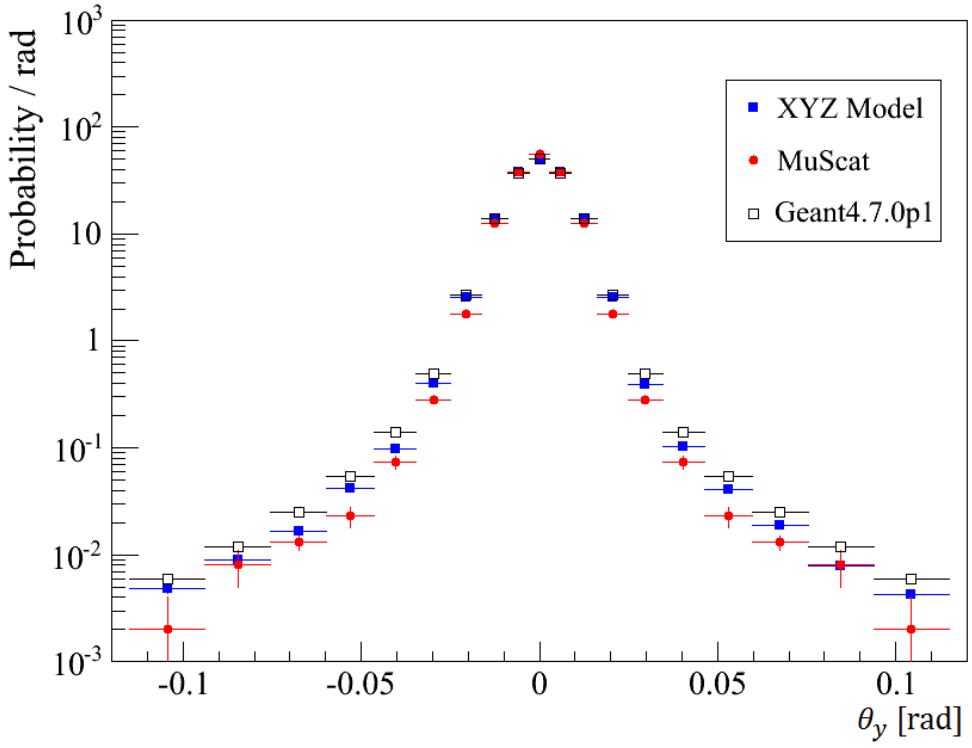

(b) 4.74 mm CH_2.

Figure 7.8: Scattering probability distributions for the carbon and CH_2 targets, as described in Figure 7.5.

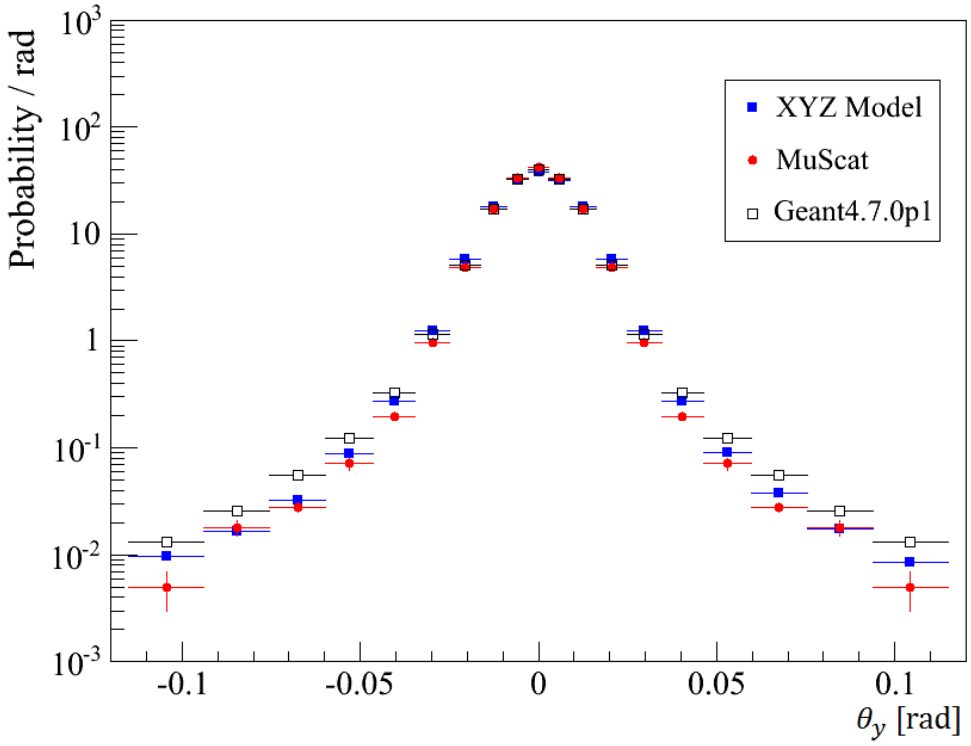

(a) 1.5 mm Al.

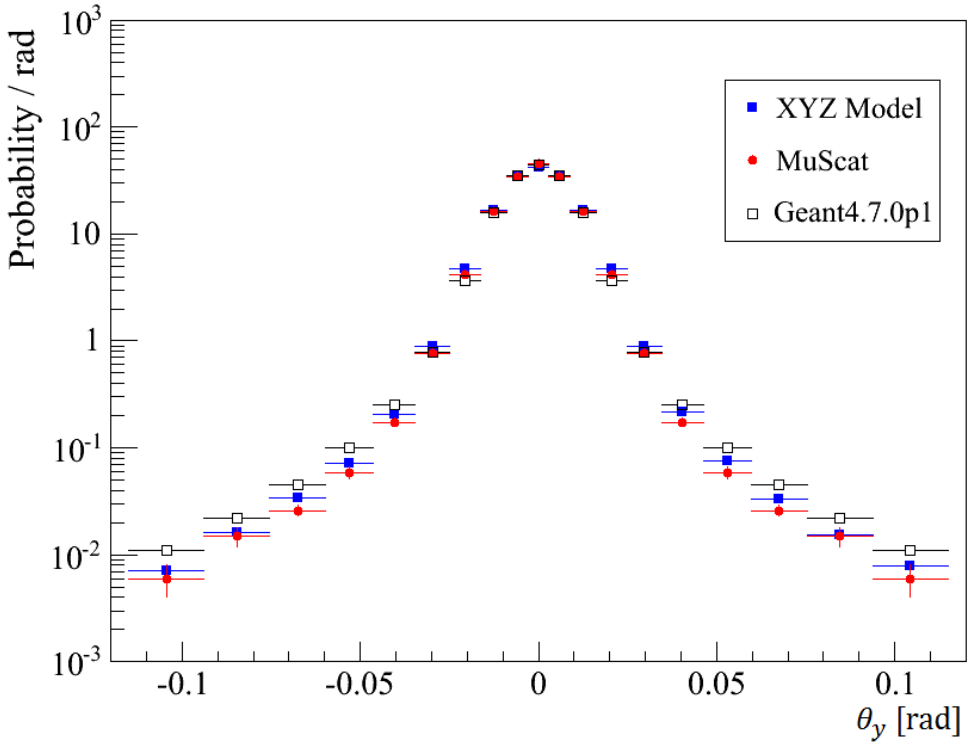

(b) 0.24 mm Fe.

Figure 7.9: Scattering probability distributions for the aluminium and iron targets, as described in Figure 7.5.

		XYZ			ICOOL			Maus
	MuScat	Born	Molière	NSW	Bethe	Fano	Tollestrup	Urban
LH_2 (i)	49.5 ± 2.7	48.4	48.6	51.3	47.4	48.2	48.5	49.2
LH_2 (ii)	40.6 ± 1.7	39.9	40.6	42.2	-	-	-	40.1
Li (i)	89.4 ± 4.4	80.5	81.0	85.5	-	-	-	83.6
Li (ii)	61.7 ± 3.4	57.5	57.7	60.9	57.3	57.0	58.8	58.8
Be (i)	112.0 ± 4.9	96.8	97.4	102.7	-	-	-	101.1
Be (ii)	54.2 ± 5.4	50.3	50.6	53.7	50.2	50.7	51.9	51.5
C	55.7 ± 3.0	51.7	51.9	54.8	52.0	52.2	53.6	48.6
CH_2	55.4 ± 3.1	50.2	50.5	53.3	52.2	54.5	53.1	53.9
Al	41.7 ± 2.4	37.8	38.2	40.4	38.4	38.6	39.0	39.8

Table 7.4: Scattering probability per radian in the central bin near zero degrees, as predicted in Monte Carlo. ICOOL values are taken from [94].

In LH_2, the distributions generated by the model are in very good visual agreement with the MuScat results, and closely resemble the ELMS values. In the central bin, ELMS (49.6 ± 0.07) and the model (48.4 ± 0.1, Born θ_1) are in good agreement with MuScat (49.5 ± 2.7), although the errors on the measurements are relatively large. The Geant4.7.0p01 predictions compare poorly with the measured distributions. In the thin, 10.9 mm LH_2 absorber for example Geant4.7.0p01 overestimates scattering by a factor of ~ 4 at 50 mrad. In contrast, the XYZ model prediction was only 13% above the measured value. For higher Z materials the model gave distributions slightly wider than the measured ones, but they were more accurate than Geant4.7.0p01 in all cases.

As discussed in Chapter 6, Fernow [94] made similar comparisons between MuScat and the scattering models in ICOOL, using the Bethe, Fano and Tollestrup models. Table 7.4 gives the bin content for the central bin (around $\theta_y = 0$ rad) for the XYZ model, Maus and ICOOL (given in Table 2 of Fernow's paper). The LH_2 (ii), Li (i) and Be (i) targets were not simulated in ICOOL. The MuScat errors are much larger than for the XYZ model and Maus Monte Carlo, both of which were less than 1%. No errors were provided with the ICOOL data, but it is reasonable to assume they are small also. Almost all models underestimate the amount of scattering, predicting probabilities $\approx 1\sigma$ below the MuScat measurements. Out of the three θ_1 descriptions, the Born and Molière simulations gave best agreement in LH_2 whilst NSW gave the best agreement in all heavier materials ($Z > 1$). All simulations gave poor agreement with the Be (i) measurement, where

the agreement was no better than $\sim 2\sigma$.

The agreement of the XYZ model with MuScat was assessed quantitatively using a standard χ^2-test:

$$\chi^2 = \sum_{i=1}^{n} (O_i - E_i)^2 / \sigma_i^2,$$

where $\sigma_i^2 = \sigma_{O,i}^2 + \sigma_{E,i}^2$. The MuScat data, O_i, and model predictions, E_i, have errors $\sigma_{O,i}$ and $\sigma_{E,i}$ respectively. Errors on the MuScat measurements, and the Geant4.7.0p01 and ELMS predictions, are given in the MuScat paper [28]. The errors for the XYZ model are proportional to $1/\sqrt{N}$, where N is the number of muons in a bin. The χ^2 was calculated over $n = 11$ bins, from 0 to 0.1151 rad in θ_y, as the distributions are folded. Over 11 bins one would normally consider $\chi^2 \sim 11$ to reflect good agreement. Figure 7.10 shows the χ^2 values for all ten targets, calculated for the XYZ model. All values are given in Table 7.5. The parameter θ_1 is calculated using the Born, Molière and NSW definitions, which were described in the previous section. As expected, the Born and Molière χ^2 values are very similar for $Z < 13$, as the difference in θ_1 is very small.

The NSW simulations give best agreement in all but the LH_2 targets ($\chi^2 > 50$). In Li, Be, C and Fe there was good agreement (χ^2 from 10 to 23), but worse in Al and CH_2 ($\chi^2 \sim 40$). Simulations with the Born and Molière θ_1 both give $\chi^2 \approx 7$ in LH_2 (i) which is remarkably good, even improving upon the ELMS agreement. In Li, Be and C they gave relatively poor agreement ($\chi^2 > 40$), and very poor agreement in Al and CH_2 where $\chi^2 > 150$.

Simulations were also made in Maus (using Geant4.9.2p04) with the ten MuScat targets and the χ^2 agreement with MuScat calculated, given in Table 7.5. Geant4.9.2p04 clearly gives much better agreement with MuScat than Geant4.7.0p01 in all but the C target. An overview of the scattering models in Geant4 as of 2010 is given in [55]. In LH_2, $\chi^2 = 20.9$ (i) and 31.0 (ii), which are worse than obtained with ELMS and the model, apart from the NSW runs. In Li and Be $\chi^2 = 28.3$ and 53.9 respectively, which was better than the Born and Molière runs but was worse than the NSW values. At higher Z, Geant4.9.2p04 gave $\chi^2 = 55$, in Al and $\chi^2 = 78$ in Fe respectively, which was worse than the NSW runs.

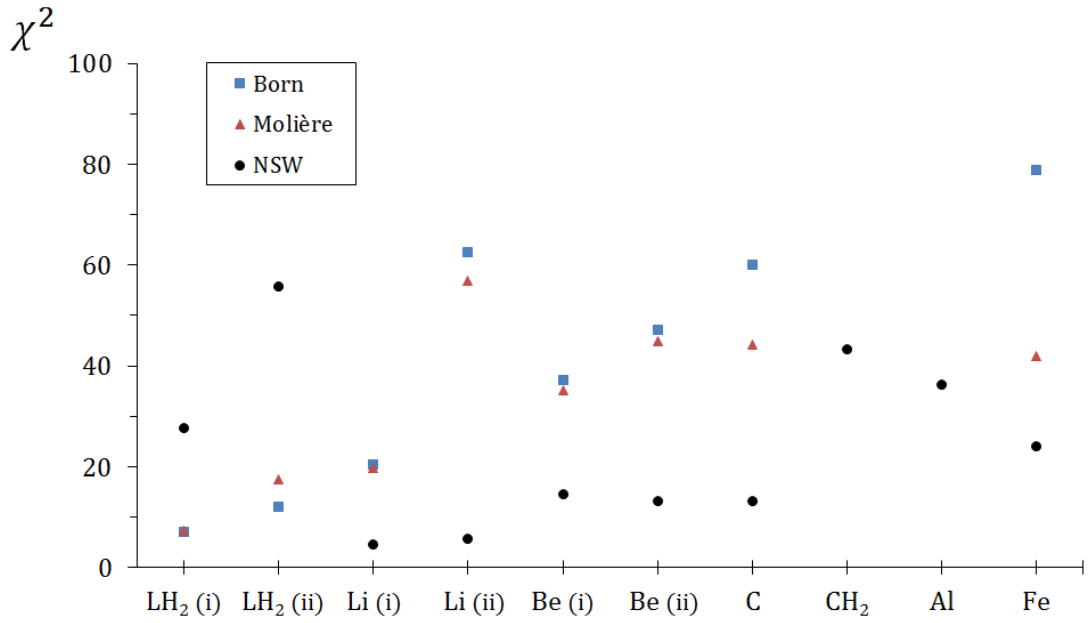

Figure 7.10: χ^2-agreement between the XYZ model and the MuScat measurements.

Target		Born	Molière	NSW	Geant4.7.0p1	ELMS	Geant4.9.2.p04
LH_2	(i)	7.1	7.2	27.6	478.2	15.4	20.9
	(ii)	12.1	17.4	55.7	622.5	29.3	31.0
Li	(i)	20.4	19.8	4.6	118.4		8.4
	(ii)	62.5	56.8	5.7	568.8		28.3
Be	(i)	37.1	35.1	14.6	103.2		14.1
	(ii)	47.2	44.9	13.1	406.7		53.9
C		60.0	44.2	13.2	315.1		307.4
CH_2		184.4	164.4	43.3	358.3		18.4
Al		206.9	173.0	36.3	243.2		55.3
Fe		78.9	42.0	24.1	157.5		78.0
	Total χ^2/n	3.92	3.27	1.30	18.75		3.53

Table 7.5: χ^2-agreement between Monte Carlo and the MuScat measurements, where the mean values, χ^2/n, are calculated over 21 bins for all ten distributions.

Whilst the XYZ model is indeed a very simple treatment of MCS, it is remarkably accurate compared with a Geant4. The χ^2-agreement of the model with MuScat clearly depends strongly on the definition of θ_1. The NSW definition was optimal for all materials apart from LH_2. The sensitivity of the model to the underlying parameters is studied in the following section.

Mean χ^2 values were calculated, over all bins and targets, for the XYZ models and the two Geant4 releases, and are given in Table 7.5. These χ^2/n values were used as a "goodness" parameter to define which of the simulations were "best". All materials were given equal weight. As anticipated, Geant4.7.0p01 gives the worst overall agreement ($\chi^2/n = 18.75$). The more recent Geant4.9.2p04 has a mean value of 3.53 using the default Urban scattering model. This was worse than reported for Geant4.8.0 [55], $\chi^2/n = 3.01$, which was not understood. The paper also gives values for the *Wentzel-VI* (2.31) and *CoulombScattering* models (1.70), which are also packaged in Geant4, but were not used in the Maus studies. The Born and Molière simulations give $\chi^2/n = 3.92$ and 3.27 respectively, which compare well with the Geant4 models. The XYZ model, using the NSW definition, gave the best agreement out of all the Monte Carlo, where $\chi^2/n = 1.30$.

7.3 Parameter study

As shown in the previous section, a simple physics model can give a very good description of the MCS distribution after an absorber. This is somewhat surprising considering the model uses just four parameters, the choice of which are somewhat approximate. Of the four parameters, θ_1 is the most difficult, as it describes the potential field of the nucleus and electron screening. Various definitions for θ_1 exist, three of which are used in the model (Born, Molière and NSW). All three of these definitions use the Thomas-Fermi radius (Equation 5.3) for the atomic size, which is inaccurate in low Z materials. There is uncertainty of the precise value of θ_1^e also, since electrons are bound to nuclei, and not screened. All simulations so far have assumed $\theta_1^e = \theta_1$, as discussed in Section 5.4.1. As shown in Table 7.5, the values of θ_1 are clearly important to the χ^2 agreement with the MuScat measurements. The model shows comparatively little sensitivity to the angles θ_2 and θ_2^e since they are far larger than a typical rms width of a distribution, as the vast majority of deflections are at small-angles.

In order to understand the model better, the χ^2 sensitivity to the parameters θ_1 and θ_1^e was studied. The parameters were scaled by the factors μ and μ^e respectively, over the range $0.5 < \mu < 3$ and $0.5 < \mu^e < 3$. Setting $\mu, \mu^e = 1$ yields the Born θ_1, and $\mu, \mu^e = 1.8$ the NSW value. The mean number of nuclear and electron scatters (Equations 7.1 and 7.2) are calculated by integrating over the DCS with θ_1 and θ_1^e as lower limits respectively. Consequently, increasing $\mu^{(e)}$ reduces the mean number of scatters. Figure 7.11a shows the distributions of two simulations with the 15.9 cm LH_2 target. Setting $\mu = 0.5$ and $\mu^e = 1$ improves the fit quality ($\chi^2 = 7.7$). Setting $\mu = 3$ and $\mu^e = 1$, however, increases the χ^2 to 31.9. Increasing μ to 3 reduces the number of nuclear collisions by a factor of ≈ 10. The θ_1^e parameter is most important in LH_2, as electron scatters account for 50% of collisions, as discussed earlier in Section 7.1.1. The optimal value for θ_1^e in LH_2 appears to be only slightly less than θ_1, so the original assumption ($\theta_1^e \approx \theta_1$) does appear justified, in this case.

Figure 7.12 shows the χ^2 contours for the six elemental MuScat targets. The compound CH_2 is not included since it has two sets of four parameters which makes an equivalent study overly complicated. The thin LH_2, Li and Be targets (i) were not studied, because their data have larger errors than for the thick targets. Figure 7.12a shows the χ^2 sensitivity for the thick (15.9 cm) LH_2 target, where the best fit was $\chi^2 = 7.7$ for $\mu = 0.5$ and $\mu^e = 1$. As expected, the χ^2 was most sensitive to θ_1^e in LH_2, since the electrons rapidly become insignificant in heavier materials. In LH_2 and Li the Born θ_1^e ($\mu^e = 1$) appears to be correct. The contours for heavier elements however, suggest that the true value for θ_1^e is approximately 1.5–2.5 times greater than the Born value. The optimal μ was greater than 1 for $Z > 1$, which was consistent with the χ^2 values in Table 7.5. The χ^2 agreement in Li and Be show comparatively little sensitivity to θ_1, possibly because the measured (MuScat) distributions have larger errors than in other materials. Optimization of θ_1, θ_1^e significantly improved upon the original χ^2 values. Setting $\mu = 1.5, \mu^e = 1.5$ for Fe, for example, gives a $\chi^2 = 10.9$, in comparison to the previous best of 24.1 (NSW θ_1). Optimal values for μ, μ^e, for all six targets, are given in Table 7.6.

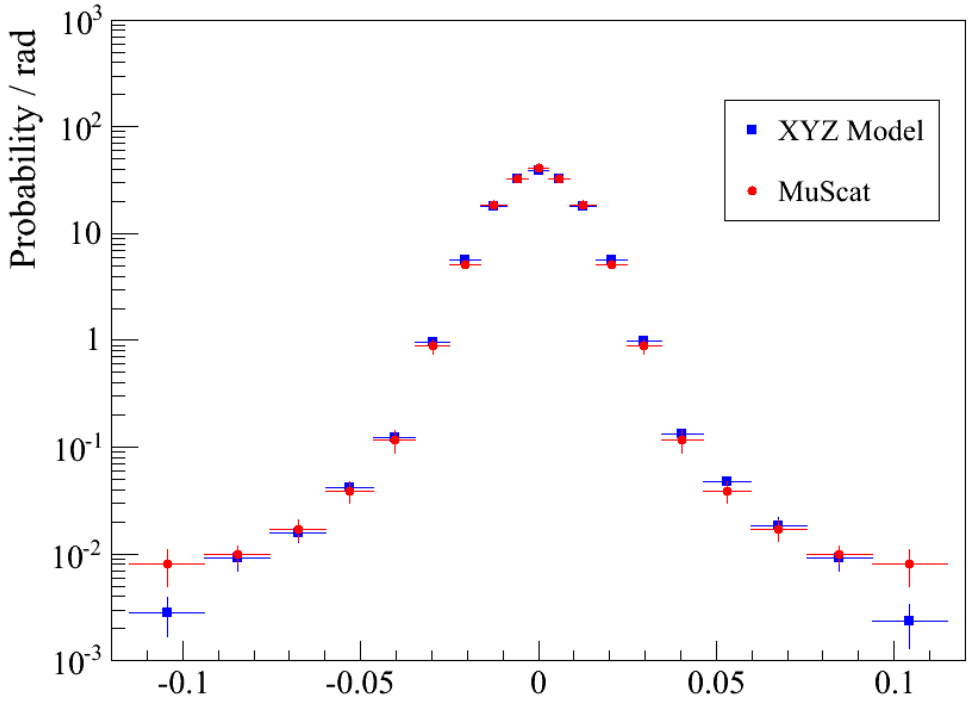

(a) $\mu = 0.5, \mu^e = 1$

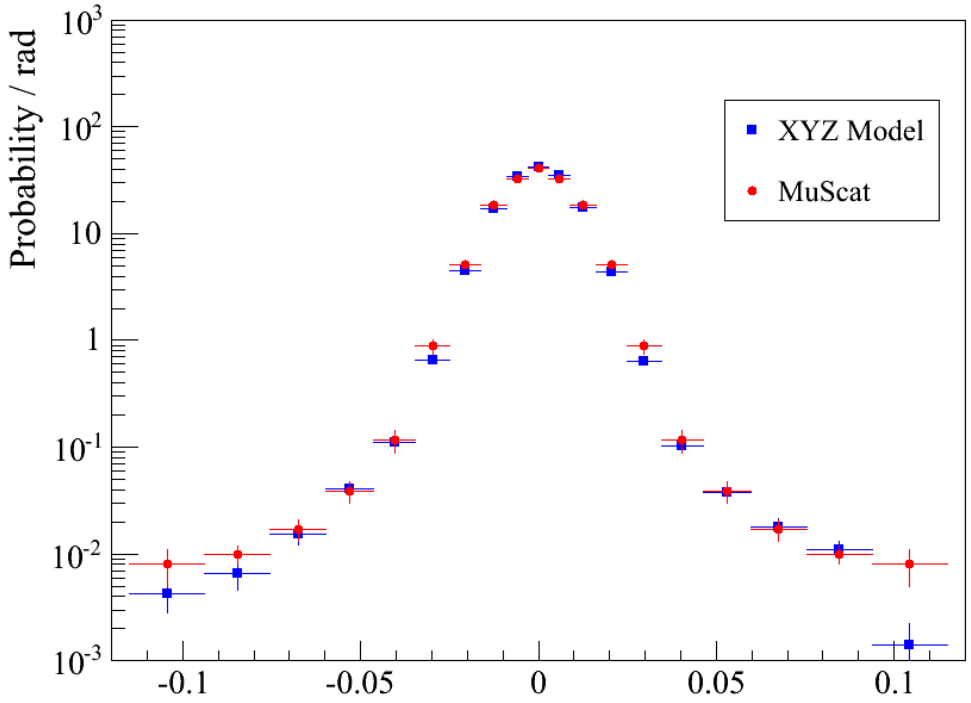

(b) $\mu = 3, \mu^e = 1$

Figure 7.11: Scattering probability distributions generated for 10^6 muons with $p = 172\,\text{MeV}/c$, after 15.9 cm of LH_2, where θ_1 and θ_1^e parameters are the Born values scaled by μ and μ^e respectively.

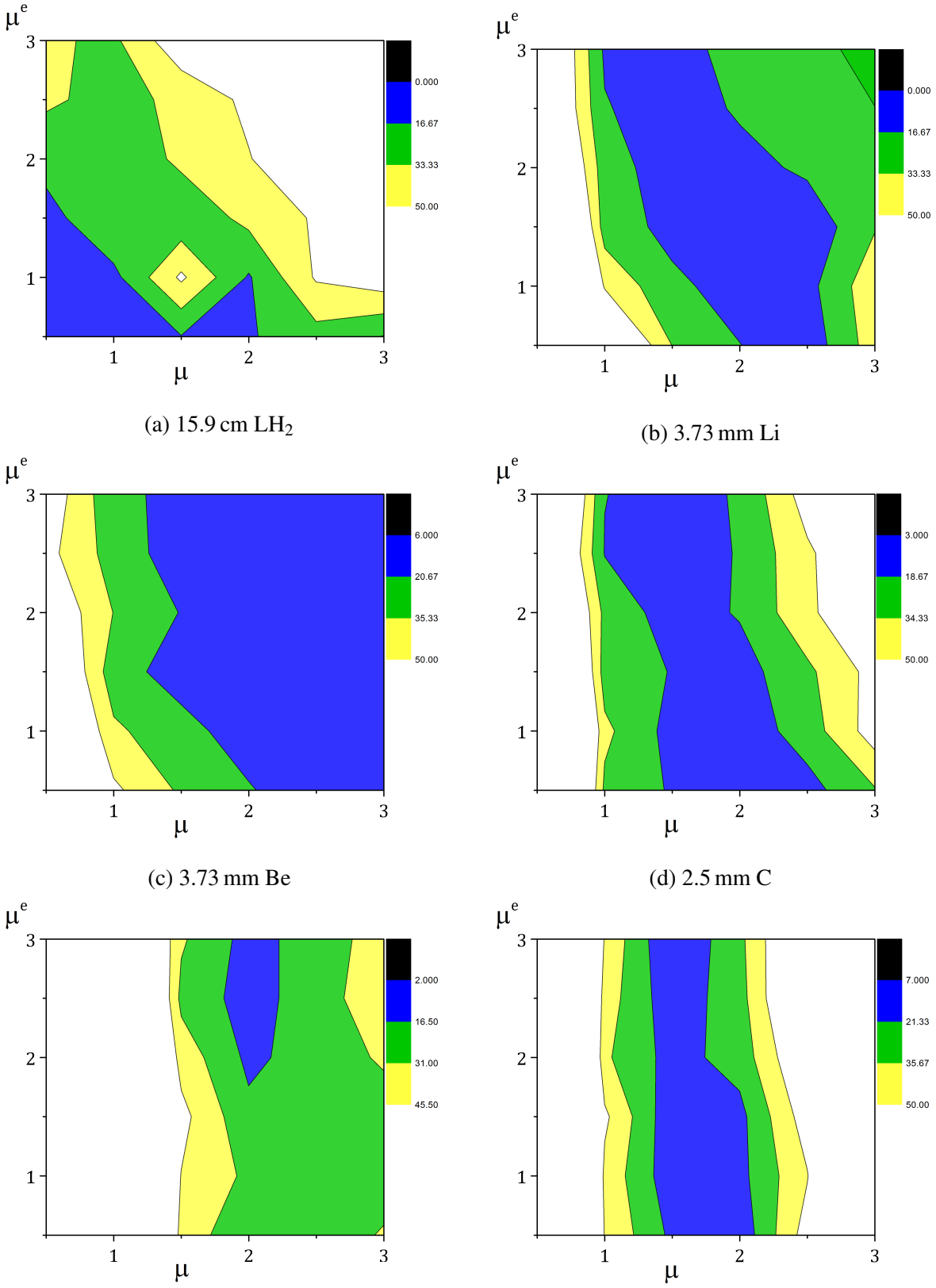

(a) 15.9 cm LH_2

(b) 3.73 mm Li

(c) 3.73 mm Be

(d) 2.5 mm C

(e) 1.5 mm Al

(f) 0.24 mm Fe

Figure 7.12: θ_1–θ_1^e χ^2 space, where μ and μ^e are scaling factors applied to θ_1 (Born) and θ_1^e respectively.

	μ	μ^e	χ^2
LH_2 (ii)	0.5	1.0	7.7
Li (ii)	2.5	1.0	4.5
Be (ii)	2.0	1.5	7.4
C	1.5	2.5	7.9
Al	2.0	2.5	10.4
Fe	1.5	1.5	10.9

Table 7.6: Optimal χ^2 values achieved using the model, where μ and μ^e are scaling factors applied to the parameters θ_1 (Born) and θ_1^e respectively.

7.4 Developing the model

As shown in Section 7.2, it is possible to develop a simple Monte Carlo model for scattering, which gives good agreement with the measured distributions of the MuScat Experiment. This is particularly remarkable considering that the XYZ model uses just two parameters, θ_1, and θ_2, to describe the entire structure of the atom. The accuracy of these parameters can be improved by fitting to the MuScat measurements, as discussed in the previous section. MICE has the opportunity to make its own measurements in Step IV, which will be investigated in Chapter 8. Additional studies could include comparison of the model against measured proton distributions. The only necessary modifications in the model would be to redefine the θ_2^e parameter (Equation 5.15) with the proton mass (938.2 MeV/c^2) in the denominator, and to use the appropriate $\langle dE/dz \rangle$ values. This change gives $\theta_2^e = 0.5$ mrad, which is roughly ten times smaller than the muon limit. As a result electron scatters will be less important to the scattering distribution than for muons.

It is important to emphasize that the XYZ model is not a tracking Monte Carlo, and only generates scattering distributions. Further development would be needed to incorporate the model into a tracking Monte Carlo such as Geant4. One way to do this would be to use tables of distributions for different materials and momenta. This is similar to how the ELMS code [49] is incorporated into ICOOL.

7.5 Summary

The XYZ model is a new treatment of multiple scattering, which generates distributions of scattering angles for straight, monoenergetic beams in material. Unlike other Monte Carlo, such as Geant4, it does not use a theory of multiple scattering, and simulates all collisions, with both nuclei and electrons, using the Wentzel single-scattering cross-section. The model uses four parameters, defined using approximate expressions, to describe the nuclear potential, electron screening and scattering kinematics.

The model gave very good agreement when compared against MuScat, which measured scattering distributions of 172 MeV/c muons in ten targets. In LH_2, the model was in excellent agreement with measured data, where $\chi^2 = 7.1$ and 12.1 for the 10.9 cm and 15.9 cm targets respectively. Over all bins and all ten targets the model gave $\chi^2/n = 1.30$–3.92, depending on the precise choice of the underlying parameters. More accurate values for θ_1, θ_1^e were derived from fits to the MuScat measurements, for use in the new scattering approximations which were developed in Chapter 5 (Equations 5.16 and 5.19). Maus showed good agreement with MuScat also, where $\chi^2/n = 3.53$, which was a vast improvement on Geant4.7.0p1, where $\chi^2/n = 18.75$. MICE is able to make its own scattering measurements in Step IV, which will now be discussed in Chapter 8.

Chapter 8

Multiple Scattering Measurements in Step IV of MICE

Multiple scattering can be measured in Step IV using the scintillating-fibre trackers both with and without the magnetic field. Predictions indicate that measurements are easier with no field, using straight muon tracks, but significant corrections are still necessary to observe the scattering distributions.

The first cooling measurements will be made in Step IV of MICE, starting in 2015. Step IV also involves a preliminary phase beginning in Q2 2014 (as shown in Figure 2.9) running with no magnetic field where muon tracks will be straight. This will allow the geometric alignment of the detectors to be studied before full operation. The anticipated cooling performance of Step IV, as predicted with Maus, was discussed in Chapter 3.

Studies were made to study and compare the intrinsic angular resolution both with and without the magnetic field. These measurements would complement those of the MuScat Experiment [28] which is, to date, the only muon scattering experiment at $\mathcal{O}(200\,\mathrm{MeV}/c)$. Step IV can also make the first multiple Coulomb scattering (MCS) measurements in LiH*, which was not used in MuScat. This chapter discusses the feasibility of measuring MCS in Step IV, in LH_2 and LiH, the primary MICE absorbers, and in the aluminium windows of the absorber focus coil (AFC) module. The MICE trackers will now be discussed in more detail.

*LiH is an excellent cooling medium and is used in the cooling scheme for the IDS Neutrino Factory design [18] (see Figure 1.1).

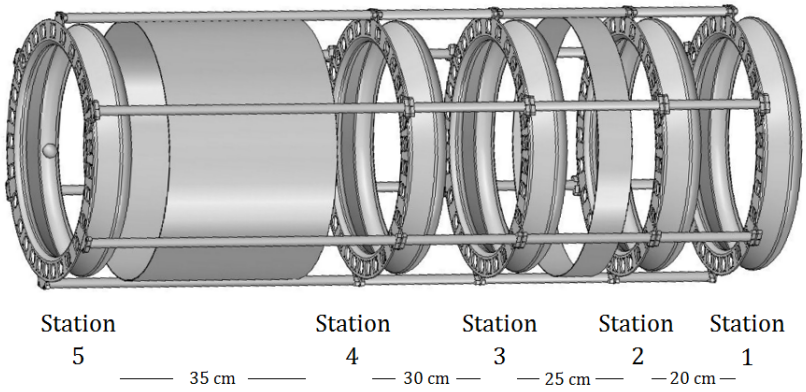

Figure 8.1: Each tracker consists of five scintillating-fibre stations, supported within a carbon-fibre frame [96].

8.1 Introduction

As discussed in Chapter 3, Step IV will run with several different absorber materials, including 35 cm of LH_2 and a solid 63 mm LiH target. Absorbers are housed within an absorber focus coil (AFC) module (shown in Figure 2.7) in which two pairs of thin, curved Al windows contain the LH_2. The windows are removed when using solid absorbers. Each window is 175 μm thick at the centre (which is aligned with the geometric axis of the channel), resulting in a total thickness of 0.7 mm of Al in the AFC module. The windows are thicker away from the centre, however.

The MICE trackers consist of five measurement planes, known as "stations", as illustrated in Figure 8.1. Each station contains polystyrene scintillating-fibres, of diameter $d = 350\,\mu$m, which are grouped together to form "channels", as shown in Figure 8.2a. There are three double layers in each station, arranged at 120° to each other, as illustrated in Figure 8.2b. They have an active detection region of 30 cm in diameter, and are read out by visible light photon counters (VLPCs). Each double layer has an average thickness $\pi d/4 = 275\,\mu$m, so the mean thickness of each tracker station (three double layers) is $t = 0.825$ mm. A 25 μm layer of Mylar is placed between each double layer, and held in place with a polyurethane adhesive [95]. Each station, including the additional Mylar and epoxy, represents 0.45% of a radiation length of polystyrene scintillating-fibre [96].

The x and y coordinates of individual muons are measured in each tracker station. Muon tracks can then be reconstructed by fitting to the measured hits in each tracker, from which the transverse

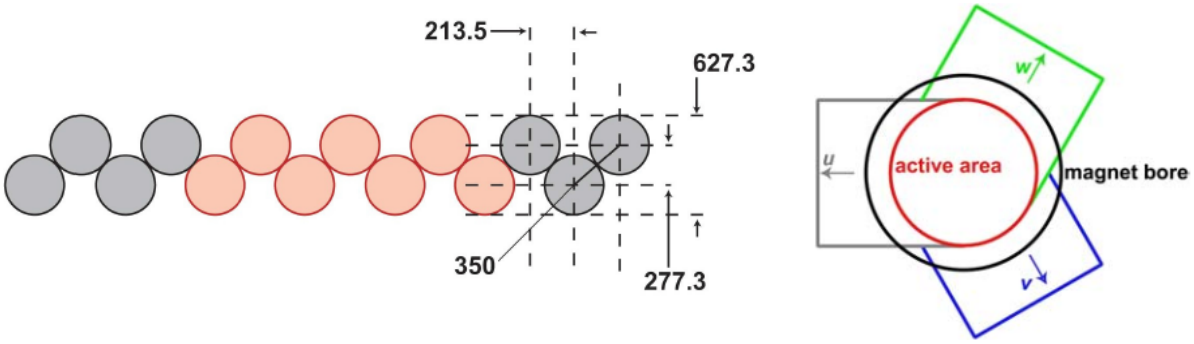

(a) (b)

Figure 8.2: (a) Fibres are grouped to form channels, as shown in red. Dimensions are given in μm. (b) A station comprises three double layers arranged at 120° to each other.

u_i	$\sigma(u_i)$
x [mm]	0.54
y [mm]	0.44
p_x [MeV/c]	2.05
p_y [MeV/c]	1.52
p_z [MeV/c]	4.58
E [MeV/c^2]	3.46

Table 8.1: Tracker resolution in phase-space coordinates u_i.

and longitudinal momenta, p_x, p_y and p_z, can be obtained. At the time of writing, however, the reconstruction software was not available. The tracker design has been tested using cosmic rays [58], so the spatial resolution is well understood and $\sigma_x = 0.54\,\text{mm}$ and $\sigma_y = 0.44\,\text{mm}$. Estimates for the p_x, p_y and p_z resolution were obtained from detailed simulations of the tracker [58], where the simulated hits were fitted using a Kalman filter. The anticipated tracker resolution is given in Table 8.1. The trackers suffer from relatively poor p_z resolution ($\sigma_{p_z} \approx 4.6\,\text{MeV}/c$) because of the difficulty in measuring p_z for tracks with low transverse momentum (which make small diameter helices). The time of flight detectors (TOFs) are more accurate, however, with $\sigma_{p_z} \approx 3.5\,\text{MeV}/c$, so it may be possible to use their p_z measurements to improve the p_z reconstruction.

Studies of the feasibility of measuring scattering in Step IV, with and without the magnetic field, will now be discussed.

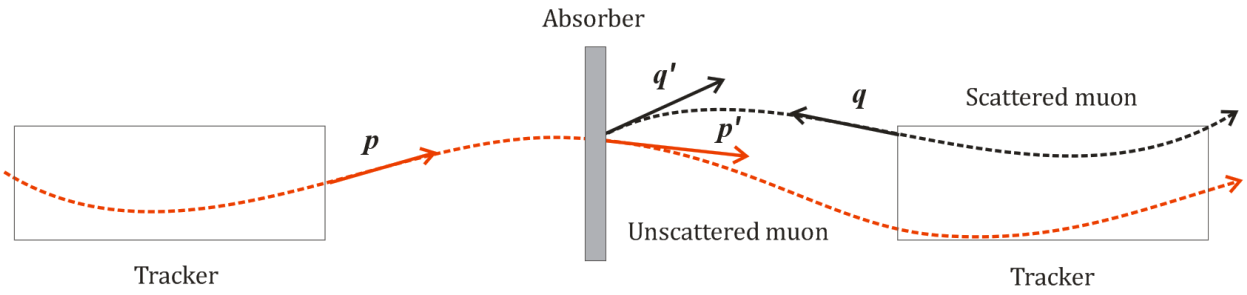

Figure 8.3: Sketch illustrating the scattering measurement procedure.

8.2 Measurements in the MICE magnetic field

MICE can measure multiple scattering and cooling simultaneously in Step IV. Muons will make helical tracks through the field, however, which makes scattering measurements complicated. Beams also have a large divergence, where $\sigma_{x'} \approx 100$ mrad (Equation 2.3) for a $\varepsilon_n = 6$ mm beam, so they cannot be treated simply as pencil beams. For a single muon, it is insufficient simply to calculate the angle between its reconstructed vectors in the upstream and downstream trackers, because the muon will be at different points in its helical rotation about the field. A procedure was devised to overcome this, shown in Figure 8.3, consisting of three steps:

i The coordinates of a muon measured in the upstream tracker (vector $\vec{p}$) are used to predict its momentum vector, $\vec{p'}$, at downstream face of the absorber in absence of scattering. This requires tracking the muon through the fields but without any material.

ii The coordinates of the same muon measured in the downstream tracker ($\vec{q}$) are used to predict its momentum vector, $\vec{q'}$, at the same position. This requires changing the sign of its momentum and flipping its charge.

iii The (3D) scattering angle, θ, for this muon, is the angle between the vectors $\vec{p'}$ and $\vec{q'}$ at the absorber face, *i.e.*

$$\cos\ \theta = \frac{\vec{p'}.\vec{q'}}{|p'||q'|}.$$

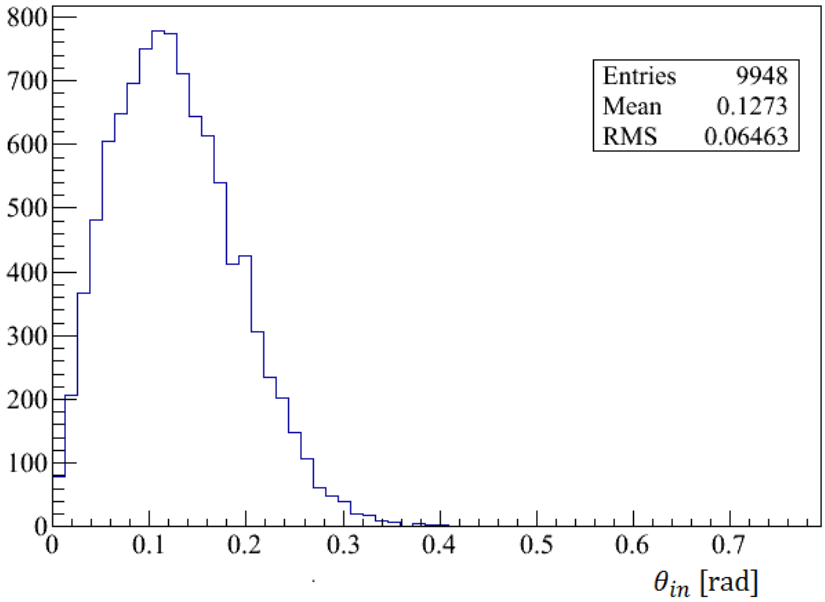

Figure 8.4: Muon track angle with respect to the z-axis before the absorber, for a $\varepsilon_n = 6$ mm beam in Step IV, simulated in Maus.

The projected 2D scattering angles, $\theta_{x,y}$, which define the angles between the muon vectors and the transverse coordinate axes, are calculated using

$$\theta_x = \frac{p'_x}{p'_z} - \frac{q'_x}{q'_z} = \theta_x^{p'} - \theta_x^{q'},$$

and similarly for θ_y. Implicit in this calculation is that the angle of the incoming track with respect to the z-axis, θ_{in}, is small (*i.e.* approximately paraxial), so the small-angle approximation ($\theta \approx \tan\theta$) holds. For a $\varepsilon_n = 6$ mm beam the average θ_{in} is predicted to be about 7.3° (0.13 rad), as shown in Figure 8.4. If θ_{in} were large (greater than about 10°) the calculation is more complicated, requiring a rotation into the frame whose z-axis is in the direction of the incident muon before scattering.

Monte Carlo studies were made to obtain estimates for the effective resolution of the procedure in the magnetic field. A $\varepsilon_n = 6$ mm beam was tracked through the Step IV geometry, scattering in the absorber material, AFC windows and tracker stations. The coordinates (x, y) and momenta (p_x, p_y, p_z) of each muon are recorded at the innermost scintillating-fibre stations in the trackers. This gives an upstream ($\vec{p}$) and a downstream ($\vec{q}$) set of vectors, which are defined as the Monte Carlo truth vectors as they assume perfect measurement resolution. The phase-space coordinates

(x, y, p_x, p_y, p_z) of each set were then smeared according to the resolutions given in Table 8.1, to reflect the measured values. These smeared muons were then tracked forward and backward as described above to obtain $\vec{p'}$ and $\vec{q'}$ at the downstream face of the absorber.

All simulations used beams of 10,000 muons with initial $p_z = 207\,\text{MeV}/c$, corresponding to $p_z = 200\,\text{MeV}/c$ at the absorber centre, and $\sigma_{p_z} = 1\,\text{MeV}/c$. Muon beams were injected into the constant field region in the upstream spectrometer solenoid, matched according to the condition $\beta_\perp \kappa = 1$, as described in Chapter 3. The baseline Step IV magnetic field (see Figure 3.2) was used in all cases.

The following Step IV simulations were made:

1. An empty channel (just fields) ("Empty");
2. An AFC module (incl. windows) without an absorber ("AFC");
3. 35 cm of LH_2, with and without the windows ("AFC + LH_2" and "LH_2"), and
4. 63 mm of LiH ("LiH").

Figures 8.5, 8.6 and 8.7 show the truth and reconstructed (obtained using the procedure outlined above) space and projected angle distributions for the AFC, LiH and LH_2 configurations in Step IV. The reconstructed distributions are significantly wider than the truth distributions. The truth distributions in the empty channel simulations had an effective width of zero, which confirms the accuracy of the tracking in Maus/Geant4. The smeared distributions for the LH_2 without windows are not shown because this case cannot be measured in MICE.

Config.	Al windows	Rms proj. angle, θ_0 [mrad] Truth	Smeared	Rms space angle, θ^{rms} [mrad] Truth	Smeared
Empty		0.0	22.2	0.0	31.9
AFC	$4 \times 175\,\mu$m	9.5	24.4	13.7	35.4
35 cm LH_2		13.8	27.4	19.9	40.4
AFC + 35 cm LH_2	$4 \times 175\,\mu$m	16.6	28.8	24.1	42.1
63 mm LiH		19.3	30.5	27.6	44.5

Table 8.2: Rms projected and rms space angles for the simulated distributions.

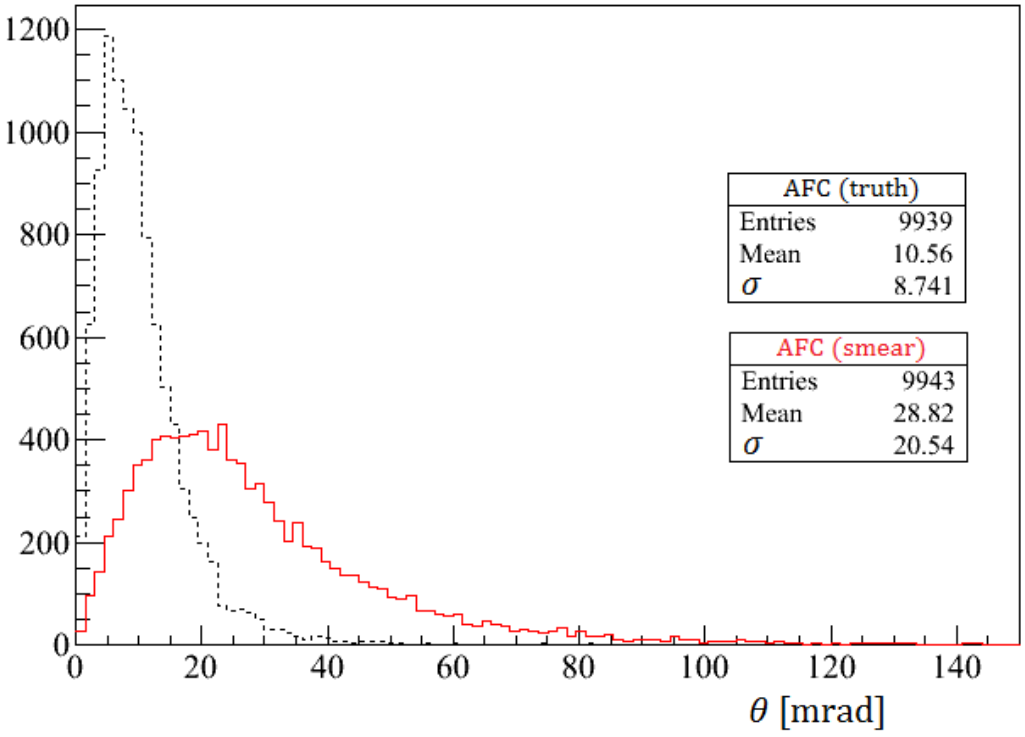

(a) Space angle (3D).

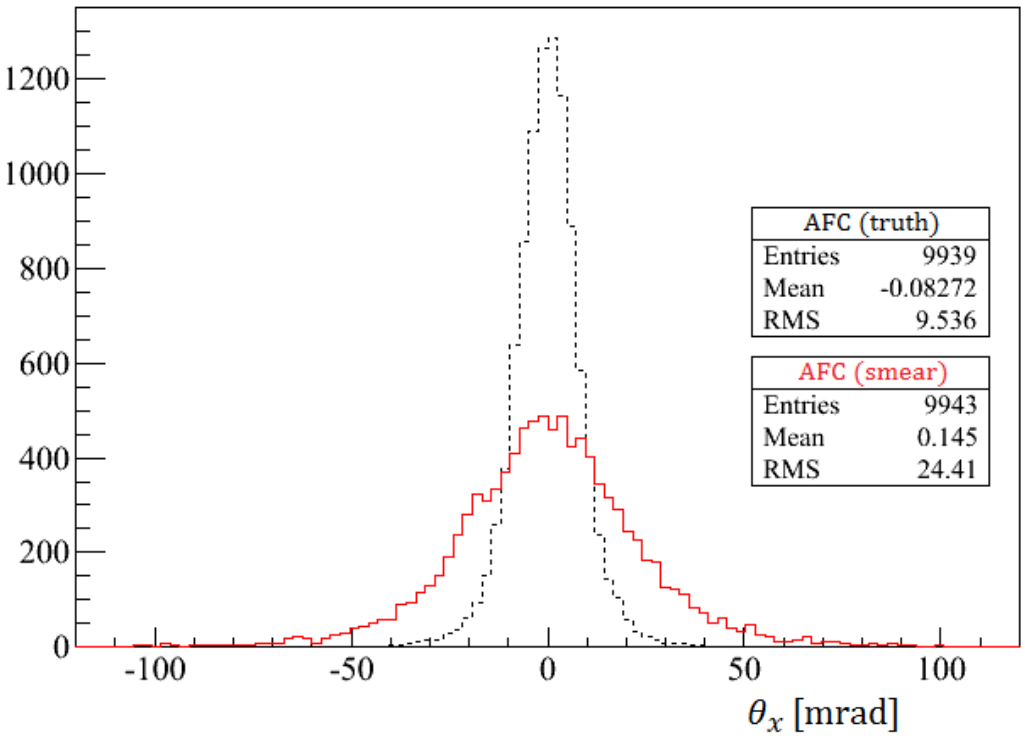

(b) Projected angle (2D).

Figure 8.5: Simulated truth and measured (smeared) distributions for scattering in the aluminium windows of the AFC module in Step IV.

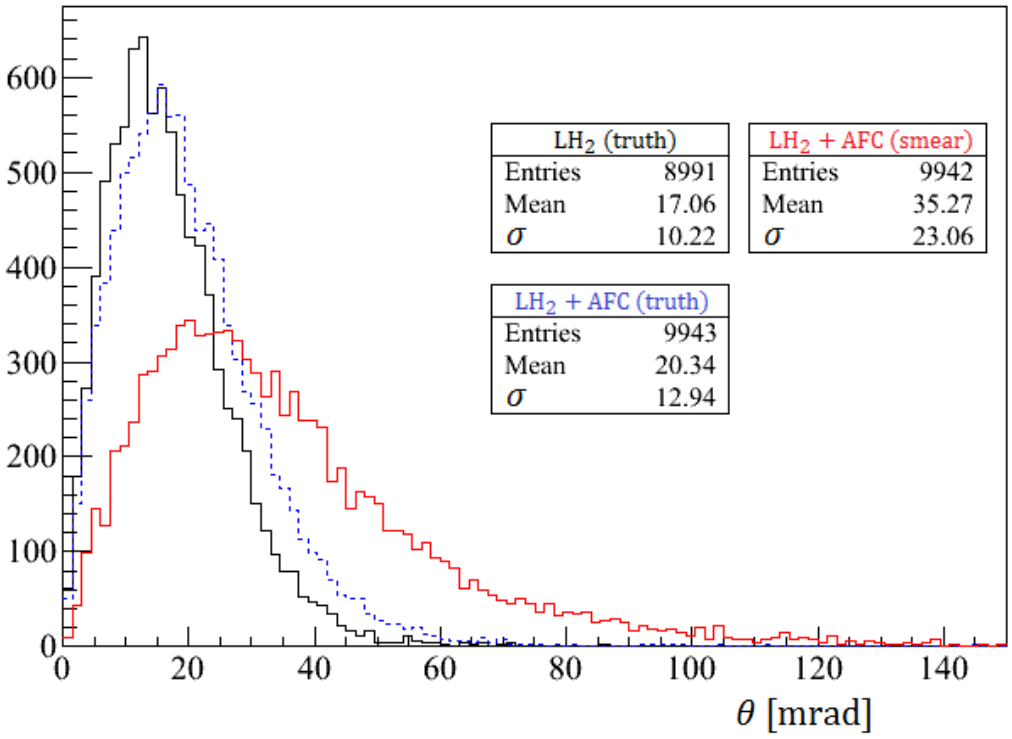

(a) Space angle (3D).

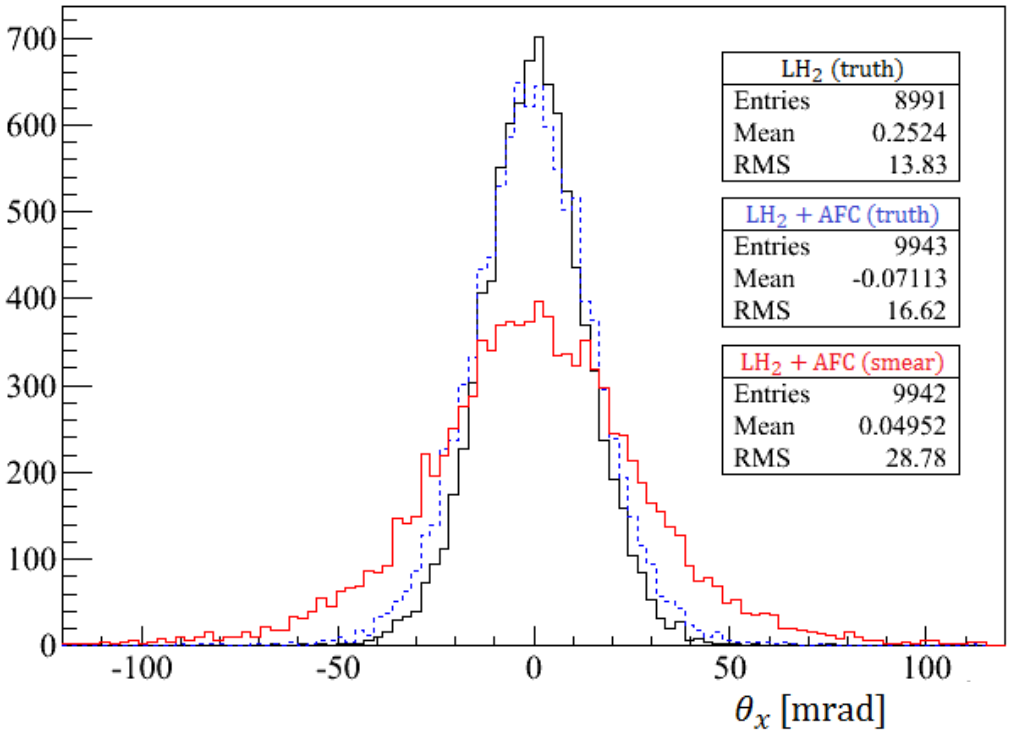

(b) Projected angle (2D).

Figure 8.6: Simulated truth and measured (smeared) distributions for scattering in the 35 cm LH_2 absorber in Step IV.

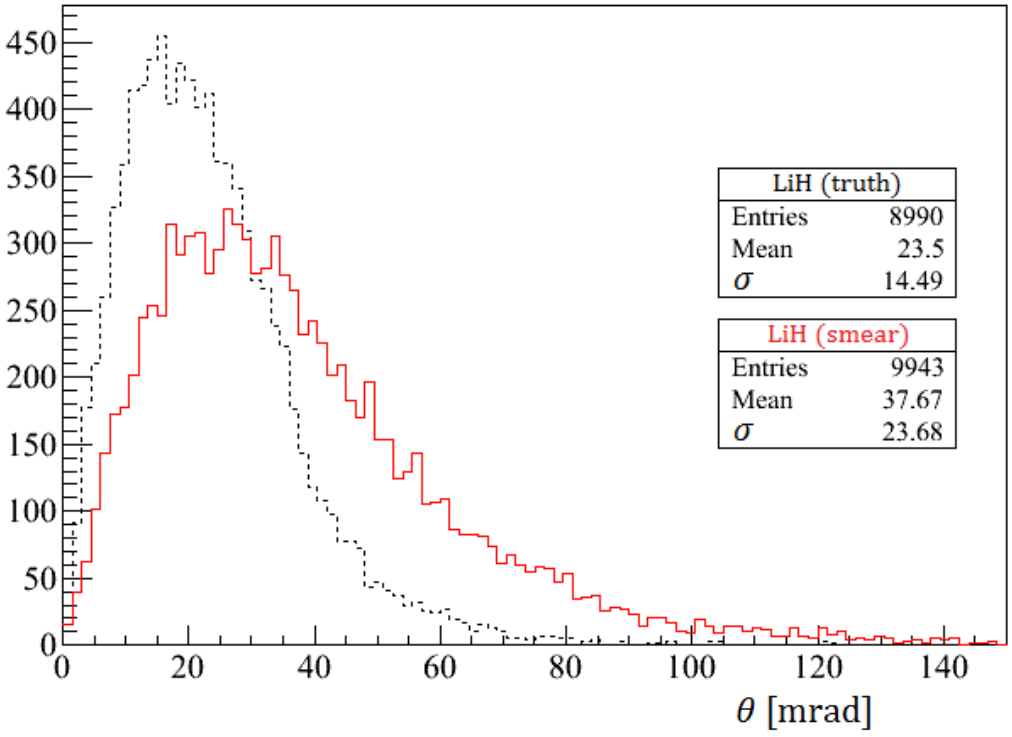

(a) Space angle (3D).

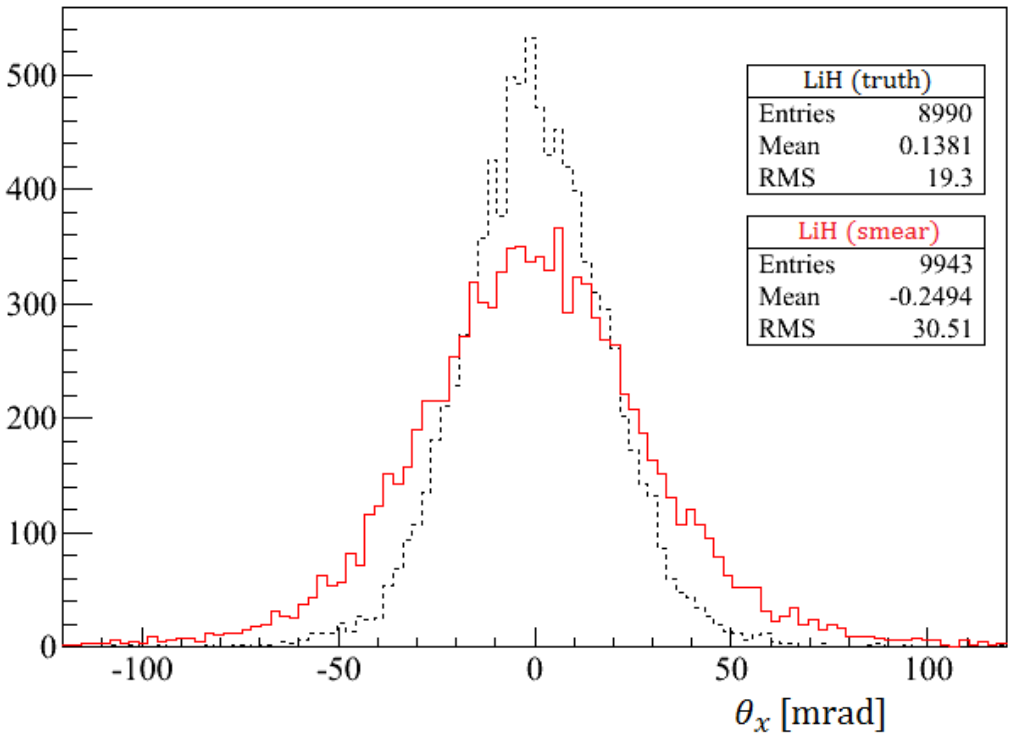

(b) Projected angle (2D).

Figure 8.7: Simulated truth and measured (smeared) distributions for scattering in the 63 mm LiH absorber in Step IV.

In an empty channel, with no absorber, the smeared simulations predict that the effective 2D angular resolution, *i.e.* the rms width, is approximately $\theta_0 = 22.2$ mrad. This is large relative to the predicted widths* of the scattering distributions for Al ($\theta_0 = 9.5$ mrad), LH_2 ($\theta_0 = 13.8$ mrad) and LiH ($\theta_0 = 19.3$ mrad).

The rms projected angles for the smeared AFC + LH_2 ($\theta_0 = 28.8$mrad) and LiH (30.5 mrad) simulations were over 60% larger than the truth values (which were 16.6 and 19.3 mrad respectively). The smeared widths are consistent with the individual contributions of the multiple scattering and tracker resolution when added in quadrature. Adding up the contributions for the AFC + LH_2 case gives $(22.2^2 + 9.5^2 + 13.8^2)^{1/2} = 27.8$ mrad for example. The rms space, θ^{rms}, and rms 2D projected, θ_0, angles for all configurations are given in Table 8.2.

From this short study it seems that substantial unfolding would be required to remove the measurement resolution. As a result, high statistics samples of the Empty and AFC configurations will be required in Step IV to unfold from the LiH and AFC + LH_2 runs respectively. Estimates for the corrections required, *i.e* the angular subtractions required to unfold the data, are given in Table 8.3.

	Fields		No fields	
	θ_0	θ^{rms}	θ_0	θ^{rms}
AFC (Al)	9.5	13.7	9.5	13.4
Measured	24.4	35.4	12.1	17.1
Correction	22.5	32.6	7.4	10.5
LH_2	13.8	19.9	13.8	19.5
Al (AFC)	9.5	13.7	9.5	13.4
Measured	28.8	42.1	18.3	25.9
Correction	23.5	34.6	12.1	17.1
LiH truth	19.3	27.6	19.3	27.3
Measured	30.5	44.5	20.7	29.3
Correction	23.6	34.9	7.4	10.5

Table 8.3: Estimated corrections required for scattering angle measurements in the trackers, with and without magnetic fields. Values are given for the rms projected angle, θ_0 [mrad], and mean square angle, θ^{rms} [mrad].

*These scattering angles are significantly larger than the predictions by the PDG formula (Equation 4.2), as muons have a longer path length in magnetic fields, because of their helical motion, and will scatter more as a result. In addition, the Al windows are thicker off-axis (up to 0.5 cm at the edges) so muons at larger amplitudes scatter more, increasing θ_0.

Further studies are necessary to understand these corrections further, using the tracker reconstruction software. It may also be possible to select a subset of tracks which are known to be well-measured, such as those with large tangential momenta, in which a p_z measurement is much easier. An alternative approach could be to obtain the scattering angle using the transfer matrices, which is less primitive than the procedure outlined here, and also warrants further study.

8.3 Straight-track scattering measurements

Multiple scattering can also be measured with no magnetic field, using straight muon tracks, as illustrated in Figure 8.8. Straight tracks can be obtained by tuning the quadrupoles in the beam line (shown in Figure 2.5) to focus the beam at the centre of the absorber, although this as not yet been demonstrated experimentally (planned for 2014). The event rate for a straight beam will be lower than with the magnetic field as there is no field to contain the muons. Straight-track scattering measurements, however, are simpler than with fields because the scattering can be measured directly using the trackers, and will require a smaller correction. Estimates for the angular resolution of a scattering measurement with no magnetic field will now be derived using standard formulae.

Straight tracks can be reconstructed by fitting to the hits in each tracker. As discussed above, the trackers have a spatial measurement resolution of $\sigma_x = 0.54\,\text{mm}$ and $\sigma_y = 0.44\,\text{mm}$. However, it is also important to consider multiple scattering in each of the polystyrene station, which each represent 0.45% of a radiation length. Using the PDG approximation (Equation 4.2) the rms projected scattering angle, θ_0, will be 5.0 mrad for a 207 MeV/c muon beam. Scattering at each plane displaces the track by $s\theta_0$ between stations, where s is the separation. Between the fourth and fifth stations, where $s = 35\,\text{cm}$, this displacement is approximately 1.73 mm. This is a significant effect as it over three times greater than the spatial resolution, so scattering clearly dominates. As a result, the hits in the first three tracker stations are not particularly helpful in reconstructing the track vector upon entering the absorber, as illustrated in Figure 8.9.

The angular resolution of the trackers can be roughly estimated by considering only the hits in

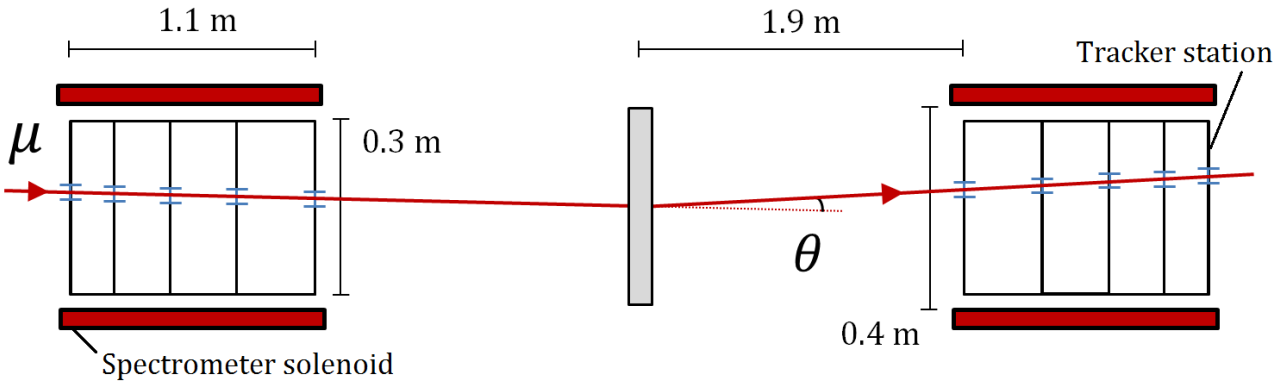

Figure 8.8: Scattering angle measurements using straight muons tracks (no magnetic field) in Step IV.

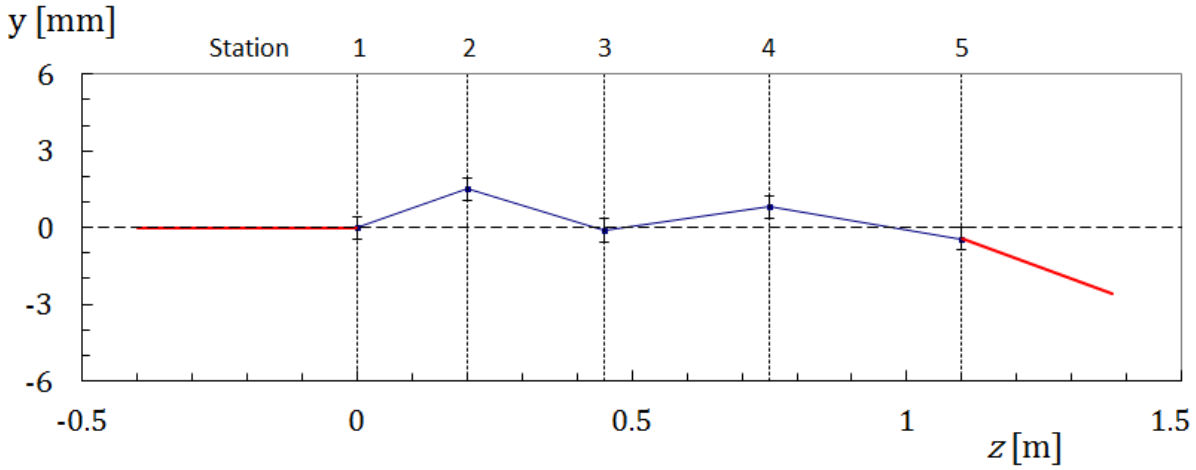

Figure 8.9: An incoming muon will scatter in each scintillating-fibre station in the tracker, which can significantly change its trajectory. This diagram comes from a simple spreadsheet Monte Carlo using realistic scattering angles.

stations 4 and 5, *i.e.* those closest to the absorber. A track between these stations requires two hits, so the angular resolution of the tracker is $2\sigma_y^2/s^2 \approx (1.8\,\text{mrad})^2$, where $\sigma_y = 0.44\,\text{mm}$. Scattering in the final station is unavoidable and unmeasurable, so the track angular resolution can be no better than 5.0 mrad. Adding scattering to the tracker resolution in quadrature gives an overall resolution of $\sigma_\theta^2 = (1.8\,\text{mrad})^2 + (5.0\,\text{mrad})^2 = (5.3\,\text{mrad})^2$ for each tracker.

	Al windows	Rms projected angle, θ_0 [mrad] Truth	Smeared
Empty		0.0	7.4
AFC	$4 \times 175\,\mu$m	9.5	12.1
35 cm LH_2		13.8	15.7
AFC + 35 cm LH_2	$4 \times 175\,\mu$m	16.8	18.3
63 mm LiH		19.3	20.7

Table 8.4: Rms projected angles for the simulated distributions, in no magnetic field. The smeared values are obtained by adding the truth value and angular resolution (7.4 mrad) in quadrature.

Measuring the angle of scattering requires track measurements in both trackers, so the effective angular resolution is $\sqrt{2}\sigma_\theta \approx 7.4\,\text{mrad}$. MICE can of course measure two, independent projected angles (θ_x, θ_y) so it may be possible to combine these measurements to improve the overall resolution by a factor of $\sqrt{2}$. The measured widths of the distributions can be estimated by adding the overall measurement resolution (7.4 mrad) in quadrature with the Maus predictions for scattering in the absorber and AFC windows, which are given in Table 8.2. For example, in LH_2 the measured width would be at least 17.4 mrad. Truth and smeared values are given in Table 8.4. Scattering measurements using straight tracks, in no field, therefore seem to require much smaller corrections than in the magnetic field. Measuring θ_0 in LiH for example requires a quadrature subtraction of roughly 24 mrad in the magnetic field, but only 7 mrad in no field. A comparison is shown in Table 8.3.

8.4 Summary

Multiple scattering can be measured in Step IV using the scintillating-fibre trackers. The estimates given here indicate that measurements with no magnetic field, using straight tracks, are much simpler than with fields, but will still require significant correction because of the limited tracker resolution. Running without fields will involve a significant drop in the event rate however, in the absence of a containing field. There is an excellent opportunity to make a complete series of scattering measurements in Step IV, from LH_2 up to Al, time permitting. Such measurements would be an important contribution to the field and provide an ideal benchmark to compare with, and validate, the XYZ and Geant4 scattering models.

Chapter 9

Conclusion

The Muon Ionization Cooling Experiment (MICE) is a prototype ionization cooling channel for a Neutrino Factory, currently under construction at the Rutherford Appleton Laboratory in the UK. As discussed in Chapter 1, ionization cooling technology is essential in designs for the Neutrino Factory and Muon Collider facilities. An introduction to MICE and the technique of ionization cooling was given in Chapter 2.

The first cooling measurements of MICE will be made in Step IV in a range of different absorber materials, including LH_2 and LiH. MICE Step IV is anticipated to measure a 5% reduction in emittance, as predicted by a widely-used approximation known as the cooling formula. The expression consists of a multiple Coulomb scattering (heating) term and an energy loss (cooling) term. These predictions were found to disagree with the Monte Carlo predictions by up to 30% in LH_2, as shown in Chapter 3. This discrepancy brought in to question the reliability of both the cooling formula and the Monte Carlo physics models.

In Chapter 4, the source of this disagreement was shown to lie in the treatment of multiple Coulomb scattering, which describes the very large numbers of small-angle collisions made by charged particles as they scatter through material. In order to understand this discrepancy it was necessary to return to the fundamental physics of Rutherford and Wentzel, to find out the origins of the scattering term in cooling formula. An improved scattering expression, which correctly correctly treats scatters off atomic electrons, was then developed. This is especially important when considering

scattering in low Z materials. Using this expression, a modified form of the cooling formula was derived that improved the agreement with Monte Carlo in LH_2, to within 2%, as was shown in Chapter 5.

Monte Carlo models use the distribution of scattering angles when simulating a particle's transport through material. These distributions are usually obtained using a theory of multiple scattering. An introduction to Molière theory, the most commonly used multiple scattering theory, is given in Chapter 6. In contrast to the cooling formula, which is a simple expression, the treatment of scattering in Monte Carlo is not transparent and can involve complex assumptions and approximations.

In light of the possible uncertainty in the existing Monte Carlo, a simple model that predicts multiple scattering distributions was written, where the particle-scatters off electrons are correctly treated. The model was tested against the results of the MuScat Experiment, which made scattering angle measurements of 172 MeV/c muons in LH_2, Li, Be, C, Al, Fe and CH_2. The model predictions were compared against the measured data and showed very good agreement ($\chi^2 \sim 10$ in LH_2), as was discussed in Chapter 7.

Preliminary studies have shown that MICE has the potential to make its own multiple scattering measurements in Step IV using the the scintillating-fibre trackers, both with and without the magnetic field. Whilst corrections are required in both cases to account for the tracker resolution, initial results indicate that measurements are easier with no magnetic field. This was shown in Chapter 8. Step IV is a pivotal stage of MICE, in which the first ever ionization cooling demonstration will be made, along with only the second set of muon scattering measurements at $\mathcal{O}(200\,\mathrm{MeV}/c)$.

Bibliography

[1] G. Aad et al. (The ATLAS Collaboration). Observation of a new particle in the search for the Standard Model Higgs boson with the ATLAS detector at the LHC. *Phys. Lett. B*, 716(1):1–29, 2012.

[2] S. Chatrchyan et al. (The CMS Collaboration). Observation of a new boson at a mass of 125 GeV with the CMS experiment at the LHC . *Phys. Lett. B*, 716(1):30–61, 2012.

[3] G. Organtini. Unveiling the Higgs mechanism to students. *Eur. Phys. J.*, 33(5):1397, 2012.

[4] F. Halzen and S. Klein. IceCube: An instrument for neutrino astronomy. *Rev. Sci. Instrum.*, 81(8), 2010.

[5] D. Kaplan and K. Long. MICE: The International Muon Ionization Cooling Experiment. In *LP07, Daegu, South Korea, 2007.*

[6] Y. Ashie et al. (The Super-Kamiokande Collaboration). Evidence for an Oscillatory Signature in Atmospheric Neutrino Oscillations. *Phys. Rev. Lett.*, 93:101801, 2004.

[7] J. N. Bahcall, M. C. Gonzalez-Garcia, and C. Peña-Garay. Global analysis of solar neutrino oscillations including SNO CC measurement. *J. High Energy Phys.*, 2001(08):014, 2001.

[8] B. T. Cleveland, T. Daily, R. Davis Jr, J. R. Distel, K. Lande, C. K. Lee, P. S. Wildenhain, and J. Ullman. Measurement of the solar electron neutrino flux with the Homestake chlorine detector. *Astrophys. J.*, 496(1):505, 1998.

[9] S. Abe et al. (The KamLAND Collaboration). Precision Measurement of Neutrino Oscillation Parameters with KamLAND. *Phys. Rev. Lett.*, 100(22):221803, 2008.

[10] B Pontecorvo. Mesonium and Antimesonium. *Sov. Phys. JETP*, 6:429, 1958.

[11] Z. Maki, M. Nakagawa, and S. Sakata. Remarks on the Unified Model of Elementary Particles. *Prog. Theor. Phys.*, 28(5):870–880, 1962.

[12] P. A. R. Ade et al. (Planck Collaboration). Planck 2013 results. XVI. Cosmological parameters. arXiv:1303.5076, 2013.

[13] M. C. Gonzalez-Garcia and M. Maltoni. Phenomenology with massive neutrinos. *Phys. Rep.*, 460(1):1–129, 2008.

[14] W. Wangi et al. (Daya Bay Collaboration). The Hunt for θ_{13} at the Daya Bay nuclear power plant. *AIP Conf. Proc.*, 1222:494–497, 2010.

[15] J. K. Ahn et al. (RENO Collaboration). RENO: An Experiment for Neutrino Oscillation Parameter θ_{13} Using Reactor Neutrinos at Yonggwang. arXiv:1003.1391, 2010.

[16] K. Abe et al. (T2K Collaboration). The T2K experiment. *Nucl. Instrum. Meth. A*, 659(1):106–135, 2011.

[17] P. Coloma, P. Huber, J. Kopp, and W. Winter. Systematic uncertainties in long-baseline neutrino oscillations for large θ_{13}. *Phys. Rev. D*, 87(3):033004, 2013.

[18] S. Choubey et al. (IDS-NF Collaboration). Interim Design Report. `https://www.ids-nf.org/`, 2011. IDS-NF-020.

[19] S. Ozaki, R. B. Palmer, M. Zisman, and J. Gallardo (ed.). Feasibility Study-II of a muon-based neutrino source. `http://www.cap.bnl.gov/mumu/studyii/`, 2001. BNL-52623.

[20] J. S. Berg, S. A. Bogacz, S. Caspi, J. Cobb, R. C. Fernow, J. C. Gallardo, S. Kahn, H. Kirk, D. Neuffer, R. Palmer, K. Paul, H. Witte, and M. Zisman. Cost-effective design for a neutrino factory. *Phys. Rev. ST Accel. Beams*, 9:011001, 2006. doi:10.1103/PhysRevSTAB.9.011001.

[21] S. Geer. Muon Colliders and Neutrino Factories. *Annu. Rev. Nucl. Part. Sci.*, 59(1):347–365, 2009.

[22] K. Wille. *The Physics of Particle Accelerators*. Oxford University Press, 2000.

[23] R. Tomas. Overview of the compact linear collider. *Phys. Rev. ST Accel. Beams*, 13(1):014801, 2010.

[24] J. Brau et al. (ILC Collaboration). International Linear Collider Reference Design Report. `http://www.linearcollider.org/ILC/Publications/Reference-Design-Report`, 2007.

[25] S. Nagaitsev. Project X - a new multi megawatt proton source at Fermilab. arXiv:1208.5759, 2012.

[26] A. Skrinsky and V. Parkhomchuk. Cooling methods for beams of charged partices. *Sov. J. Part. Nucl.*, 12:223, 1981.

[27] K. Yonehara, R. P. Johnson, and Y. S Derbenev. Helical channel design and technology for cooling of muon beams. In *AIP Conf. Proc., 2010.*

[28] D. Attwood et al. (MuScat Collaboration). The scattering of muons in low Z materials. *Nucl. Instrum. Meth. B*, 251(1):41–55, 2006. With permission from Elsevier.

[29] J. Rosenzweig. *Fundamentals of beam physics*. Oxford University Press, 2003.

[30] G. Penn and J. S. Wurtele. Beam envelope equations for cooling of muons in solenoid fields. *Phys. Rev. Lett.*, 85(4):764, 2000.

[31] R. C. Fernow and J. C. Gallardo. Muon transverse ionization cooling: Stochastic approach. *Phys. Rev. E*, 52:1039–1042, 1995.

[32] J. Beringer et al. Review of particle physics. *Phys. Rev. D*, 86(1), 2012.

[33] Y.-S. Tsai. Pair production and bremsstrahlung of charged leptons. *Rev. Mod. Phys.*, 46:815–851, 1974.

[34] B. Rossi and K. Greisen. Cosmic-Ray Theory. *Rev. Mod. Phys.*, 13:240–309, 1941.

[35] A. Blondel and et al. (MICE Collaboration). Proposal to the Rutherford Appleton Laboratory: an international muon ionization cooling experiment (MICE). `http://mice.iit.edu/`, 2003. MICE note 21.

[36] M. Bogomilov et al. (MICE Collaboration). The MICE Muon Beam on ISIS and the beamline instrumentation of the Muon Ionization Cooling Experiment. *J. Instrum.*, 7(05):P05009, 2012.

[37] D. Adams et al. (MICE Collaboration). Characterisation of the muon beams for the Muon Ionisation Cooling Experiment. *Eur. Phys. J.*, C73:2582, 2013.

[38] R. Bertoni et al. The design and commissioning of the MICE upstream time-of-flight system. *Nucl. Instrum. Meth. A*, 615(1):14–26, 2010.

[39] D. Bolognini et al. Tests of the MICE Electron Muon Ranger front end electronics with a small scale prototype. *Nucl. Instrum. Meth. A*, 646(1):108–117, 2011.

[40] M. Rayner. *The development of a novel technique for characterizing the MICE muon beam and demonstrating its suitability for a muon cooling measurement*. PhD thesis, University of Oxford, 2011.

[41] C. Rogers, P. Snopok, L. Coney, and A. Jansson. Wedge Absorber Design for the Muon Ionisation Cooling Experiment. In *IPAC10, Kyoto, Japan, 2010.*

[42] M. Apollonio and H. Witte. Optimizing the MICE matching coil currents for the production spectrometer solenoids. `http://mice.iit.edu/`, 2006. MICE note 153.

[43] The MICE Collaboration. Maus. `http://micewww.pp.rl.ac.uk/projects/maus`.

[44] S. Agostinelli et al. (GEANT Collaboration). GEANT4: A simulation toolkit. *Nucl. Instrum. Meth. A*, 506(3):250–303, 2003.

[45] J. H. Cobb. Statistical errors on emittance measurements. `http://mice.iit.edu/`, 2009. MICE note 268.

[46] M. Apollonio and J. H. Cobb. Absorbers for MICE Step III. `http://mice.iit.edu/`, 2008. MICE note 199.

[47] R. C. Fernow. ICOOL: a simulation code for ionization cooling of muon beams. In *PAC99, New York, USA, 1999.*

[48] GEANT Collaboration. *Geant3 Manual*. `http://wwwasdoc.web.cern.ch/wwwasdoc/pdfdir/geant.pdf`, 1993. CERN Program Library Long Writeup W5013.

[49] W. W. M. Allison, J. H. Cobb, S. J. Holmes, R. C. Fernow, and R. B. Palmer. *Ab initio* liquid hydrogen muon cooling simulations with ELMS. *J. Phys. G*, 34(4):679, 2007.

[50] S. Holmes. *The Physics of Muon Cooling for a Neutrino Factory*. PhD thesis, University of Oxford, 2006.

[51] L. D. Landau. On the energy loss of fast particles by ionization. *J. Phys.*, 8:201–205, 1944.

[52] H. Lewis. Multiple Scattering in an Infinite Medium. *Phys. Rev.*, 78:526–529, 1950.

[53] GEANT Collaboration. *GEANT4 Physics Reference Manual*. `http://geant4.cern.ch/support/userdocuments.shtml`, 2011.

[54] J. M. Fernádez-Varea, R. Mayol, J. Baró J, and F. Salvat. On the theory and simulation of multiple elastic scattering of electrons. *Nucl. Instrum. Meth. B*, 73(4):447–473, 1993.

[55] V. Ivanchenko, O. N. Kadri, M. Maire, and L. Urban. Geant4 models for simulation of multiple scattering. *J. Phys. Conf. Ser.*, 219:032045, 2010.

[56] B. Rossi. *High-energy particles*. Prentice-Hall, 1952.

[57] V. Highland. Some practical remarks on multiple scattering. *Nucl. Instrum. Methods*, 129(2):497–499, 1975.

[58] A. Khan et al. MICE Scintillating Fibre Tracker Prototype. `http://mice.iit.edu/`, 2005. MICE note 90.

[59] E. Rutherford. LXXIX. The scattering of α and β particles by matter and the structure of the atom. *Philos. Mag. Ser. 6*, 21(125):669–688, 1911.

[60] J. J. Thomson. XXIV. On the structure of the atom: an investigation of the stability and periods of oscillation of a number of corpuscles arranged at equal intervals around the circumference of a circle; with application of the results to the theory of atomic structure. *Philos. Mag. Ser. 6*, 7(39):237–265, 1904.

[61] J. D. Jackson. *Classical Electrodynamics*. Wiley, 3rd edition, 1998.

[62] B. Povh, M. Lavelle, K. Rith, C. Scholz, and F. Zetsche. *Particles and Nuclei: An Introduction to the Physical Concepts*. Springer, 2008.

[63] W. Scott. The Theory of Small-Angle Multiple Scattering of Fast Charged Particles. *Rev. Mod. Phys.*, 35:231–313, 1963.

[64] G. Wentzel. Zwei Bemerkungen über die Zerstreuung korpuskularer Strahlen als Beugungserscheinung. *Z. Phys.*, 40:590, 1926.

[65] N. F. Mott and H. S. W. Massey. *The theory of atomic collisions*. Clarendon Press, 1965.

[66] F. Mandl. *Quantum Mechanics*. Butterworth Scientific Publications., 2nd edition, 1957.

[67] F. Salvat. Elastic scattering of fast electrons and positrons by atoms. *Phys. Rev. A*, 43:578–581, 1991.

[68] E. Fermi. Eine statistische Methode zur Bestimmung einiger Eigenschaften des Atoms und ihre Anwendung auf die Theorie des periodischen Systems der Elemente. *Z. Phys.*, 48(1-2):73–79, 1928.

[69] L. Thomas. The calculation of atomic fields. *Math. Proc. Cambridge*, 23:542–548, 1927.

[70] H. Bethe. Molière's Theory of Multiple Scattering. *Phys. Rev.*, 89:1256–1266, 1953.

[71] G. Lynch and O. Dahl. Approximations to multiple Coulomb scattering. *Nucl. Instrum. Meth. B*, 58(1):6–10, 1991.

[72] A. C. Thompson and D. et al. Vaughan. *X-ray Data Booklet*. Lawrence Berkeley Laboratory, 2001.

[73] S. Goudsmit and J. Saunderson. Multiple Scattering of Electrons. *Phys. Rev.*, 57:552–552, 1940.

[74] S. Goudsmit and J. Saunderson. Multiple Scattering of Electrons. II. *Phys. Rev.*, 58:36–42, 1940.

[75] E. Williams. Concerning the Scattering of Fast Electrons and of Cosmic-Ray Particles. *Proc. R. Soc. Lond. A*, 169(939):531–572, 1939.

[76] E. Williams. Multiple Scattering of Fast Electrons and Alpha-Particles, and "Curvature" of Cloud Tracks Due to Scattering. *Phys. Rev.*, 58:292–306, 1940.

[77] G. Molière. Theorie der Streuung schneller geladener Teilchen I. *Z. Naturforsch.*, 2a(40):133, 1947.

[78] G. Molière. Theorie der streuung schneller geladener teilchen ii. mehrfach-und vielfachstreuung. *Z. Naturforsch.*, 3a:78, 1948.

[79] U. Fano. Inelastic Collisions and the Molière Theory of Multiple Scattering. *Phys. Rev.*, 93:117–120, 1954.

[80] H. Snyder and W. Scott. Multiple Scattering of Fast Charged Particles. *Phys. Rev.*, 76:220–225, 1949.

[81] E. Bullard et al. Remarks on the scattering of electrons by atomic fields. *Proc. Camb. Philos. Soc.*, 26:556, 1930.

[82] H. E. Ahn. *Part I, Angular Distribution Measurement of Beam-Foil Muonium, Part II, Muon Injection Simulation for a New Muon g-2 Experiment*. PhD thesis, Yale University, 1992.

[83] L. I. Schiff. *Quantum Mechanics*. McGraw-Hill, 3rd edition, 1968.

[84] E. Zeitler and H. Olsen. Complex Scattering Amplitudes in Elastic Electron Scattering. *Phys. Rev.*, 162:1439–1447, 1967.

[85] M. Berger and R. Wang. *Monte Carlo Transport of Electrons and Photons*. Plenum, 1988.

[86] L. Kulchitsky and G. Latyshev. The Multiple Scattering of Fast Electrons. *Phys. Rev.*, 61:254–265, 1942.

[87] A. O. Hanson, L. H. Lanzl, E. M. Lyman, and M. B. Scott. Measurement of Multiple Scattering of 15.7-MeV Electrons. *Phys. Rev.*, 84:634–637, 1951.

[88] H. Cox Jr. and R. Bonham. Elastic electron scattering amplitudes for neutral atoms calculated using the partial wave method at 10, 40, 70, and 100 kV for Z=1 to Z=54. *J. Chem. Phys.*, 47:2599, 1967.

[89] B. Gottschalk, A. M. Koehler, R. J. Schneider, J. M. Sisterson, and M. S. Wagner. Multiple Coulomb scattering of 160 MeV protons. *Nucl. Instrum. Meth. B*, 74(4):467–490, 1993.

[90] B. Nigam, M. Sundaresan, and T. Wu. Theory of Multiple Scattering: Second Born Approximation and Corrections to Molière's Work. *Phys. Rev.*, 115:491–502, 1959.

[91] J. Marion and B. Zimmerman. Multiple scattering of charged particles. *Nucl. Instrum. Methods*, 51(1):93–101, 1967.

[92] G. Shen et al. Measurement of multiple scattering at 50 to 200 GeV/c. *Phys. Rev. D*, 20:1584–1588, 1979.

[93] A. Tollestrup and J. Monroe. Multiple scattering calculations for hydrogen, helium, lithium and beryllium. `http://nfmcc-docdb.fnal.gov/`, 2000. MuCool note 176.

[94] R. C. Fernow. Scattering in ICOOL. `http://nfmcc-docdb.fnal.gov/`, 2006. MuCool note 336.

[95] D. Adey. *Beam instrumentation and investigations into muon cooling at MICE*. PhD thesis, University of Warwick, 2012.

[96] M. Ellis et al. The design, construction and performance of the MICE scintillating-fibre trackers. *Nucl. Instrum. Meth. A*, 659(1):136–153, 2011.